DISK DRIVE ACTUATOR DESIGN AND CONTROL FOR ROBUST NON-OPERATIONAL SHOCK PERFORMANCE

By

RYAN TODD RATLIFF

Bachelor of Science
University of Oklahoma
Norman, Oklahoma, USA
1992

Master of Science
University of Oklahoma
Norman, Oklahoma, USA
1997

Submitted to the Faculty of the
Graduate College of
Oklahoma State University
in partial fulfillment of
the requirements for
the Degree of
DOCTOR OF PHILOSOPHY
December, 2005

COPYRIGHT ©

By

RYAN TODD RATLIFF

December, 2005

DISK DRIVE ACTUATOR DESIGN AND CONTROL FOR ROBUST NON-OPERATIONAL SHOCK PERFORMANCE

Dissertation Approved:

Prabhakar R. Pagilla

Dissertation Advisor

Rafael Fierro

Eduardo A. Misawa

Gary E. Young

Dean of the Graduate College

TABLE OF CONTENTS

LIST OF TABLES

LIST OF FIGURES

CHAPTER 1

INTRODUCTION

The read/write (R/W) heads of a hard disk drive are very sensitive to external shock and vibration. Shock and vibration dynamics can cause head/disk impact (HDI). If the impact occurs in the area where data is stored, data loss or permanent damage can occur. Typically, there is a maximum shock and vibration specification limit that corresponds to a given head design. Shock specifications are determined for both operational and non-operational states. Disk drives will usually be subject to higher shock levels during the non-operational state primarily resulting from shipping and handling. During this process, the drive could incur dynamics from both linear and rotational shocks. In order to prevent damage and data loss, disk drive manufacturers have developed methods to suppress the effects of external, non-operational dynamics. However, existing designs increase product costs and sacrifice seek performance resulting from the added shock protection. This research introduces enhanced mechanical design and control methods that provide adequate shock protection against linear and rotational dynamics while eliminating the additional cost and performance reduction associated with current designs.

In the case of rotary shocks, modern designs incorporate latching or locking mechanisms to hold the actuator arm at a specific position when the drive is not in operation. This allows higher non-operational dynamics to be tolerated and prevents a fatal event, caused by a drop or careless handling, that would physically damage the drive. The majority of the latch designs that exist today are passive and require external sources of mechanical energy. For example, certain latch designs take ad-

vantage of the high velocity airflow generated by the spinning disks for actuation [1]. Other designs rely on the inertia of a separate member that moves when a shock is imparted to the drive [2]. Although not as common, some latches are designed to take advantage of magnetic forces that are inherent in the actuator magnetic circuit or supplied by a separate magnet [3, 4].

Air vane and inertial style latches are the most commonly used in industry today. Both styles are preferred for their high shock resistance capabilities. Inertial latches are common in drives sized for notebook computers and consumer electronics. An inertial-style latch is shown in Figure 1.1. The latch consists of a separate inertial member rotating about a designated pivot point. Both the pivot location and inertia of the member are designed so that the member engages the actuator arm in a finite time while subject to a specified range of rotary shock amplitudes and pulse widths.

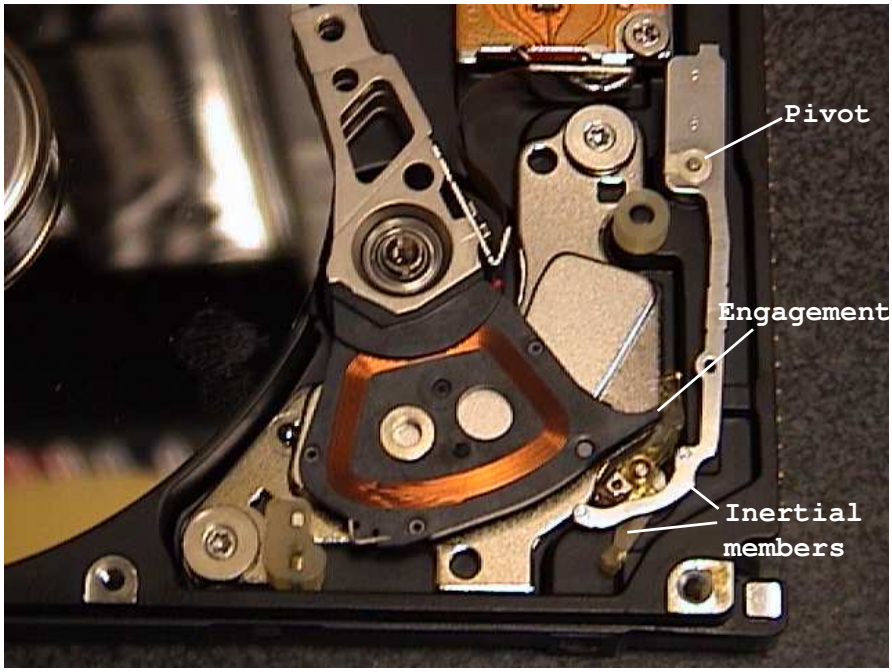

Figure 1.1: Inertial latch concept (Courtesy of Fujitsu Corp).

The engagement contact effectively blocks actuator motion and prevents the R/W heads from moving into the data zone. The timing of this engagement can become problematic, inconsistent, or even impossible if wide ranges of shock resistance are required. For example, the latch design may meet a specified upper amplitude limit at the expense of lower amplitudes. Therefore, it is possible for inertial latches to engage the actuator at higher shock amplitudes, but "miss" at lower amplitudes.

Air latches are typically found in desktop and server drives where larger disk sizes and higher spindle speeds provide stronger air flow currents. Figure 1.2 depicts an air latch consisting of a small, nominal, return bias and a "vane" member that protrudes radially along the disks obstructing potential airflow. Opposite the air vane is an engagement feature that keeps the actuator arm locked in shipping position when the drive is off. When power is applied to the drive, force is applied to the latch vane as a result of the airflow from spinning disks. The latch overcomes the return bias and stays open as long as power is applied and the disks are spinning.

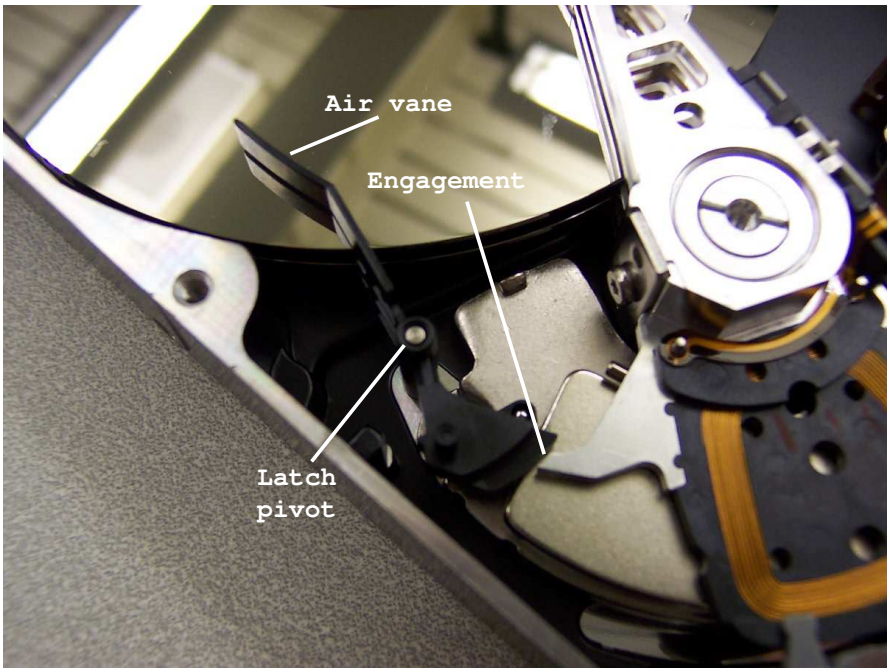

Figure 1.2: Air latch concept (Courtesy of Quantum Corp).

Disk drive manufacturers typically benefit from reducing the disk count or "depopulating" a given product. This allows the manufacturer to design only one set of mechanics and provide customers with different levels of capacity. Reducing the disk count, however, would obviously change the aerodynamics and the air latch operation. Therefore, difficulties can arise in implementation of a common air latch with a product scheduled for depopulation. Multiple latch designs may be required which is undesirable.

Magnetic, bi-stable latches are not as common because of their low shock resistance capability. They are typically found in high-end server drives where shock requirements are not so stringent. The bi-stable latch is called such because it has two stable equilibrium points. A typical bi-stable latch is shown in Figure 1.3. A plastic member rotates about a designated pivot pin. A magnet is molded into the plastic member and is attracted to two separate steel pins. The proximity of the magnet determines to which pin the magnet is attracted.

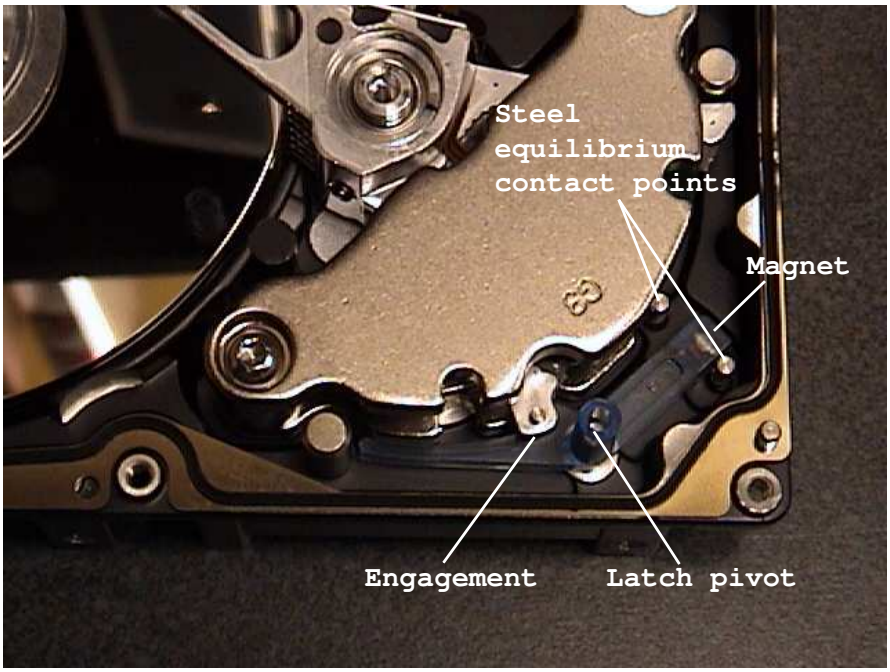

Figure 1.3: Bi-stable latch concept (Courtesy of Seagate Technology).

A properly designed bistable latch is not allowed to rest between the two pins. The engagement contact dynamics between the latch and actuator arm are analogous to that of two spur gears. The latch is actuated by the disk drive actuator itself. Hence, while closed, the latch is required to overcome the actuator arm inertia subject to a rotational shock. Conversely, the disk drive actuator must overcome the latch holding force when the drive is powered on. So the latch holding torque requirement conflicts with the actuator arm opening torque requirement. Most bi-stable latches are positioned behind the actuator limiting the coil length. A longer coil generally results in higher torque capability and improved seek performance of the actuator. Also, because there is impact involved during latching, the potential exists for particulate generation which can be fatal to a disk drive and, therefore, presents reliability issues.

All three of the previously mentioned latches result in additional cost that can become significant in high volume products. One low-cost alternative proposes adding an external bias to the arm. A magnetic bias is induced by attaching a steel object to the arm that rotates in the magnetic air gap of the actuator [5]. This latching mechanism has the advantage of a single, inexpensive mechanical part. Additionally, the size of the actuator is less restricted so motor performance can be optimized. Also, the magnetic bias provides a non-contact solution which eliminates particulate generation that is associated with latches. The disadvantage is that the bias force is typically nonlinear, and exists over most, if not all, of the actuator stroke which influences drive operation and seek controller performance. Further, the bias force nonlinearity is an unmatched uncertainty [6], which presents an additional challenge for the controller design. Backstepping techniques [7] are available to handle certain unmatched conditions in nonlinear systems. However, even if the bounds on the bias are known, the worst case bias value is required as an estimate for all drives in order to prevent saturation. If the bias could be estimated for each individual drive,

some additional seek performance could be obtained on drives that do not represent the worst case. A seek controller must be developed that can compensate for uncertain bias nonlinearities without sacrificing performance. Adaptive control techniques represent one method that can be used to handle effects of uncertain system parameters [8]. Although there has been no known published results in adaptive seek control applied to disk drives, the uncertain magnetic bias problem has definitive characteristics that make it a desirable candidate. Furthermore, distributions can be determined on a given disk drive population by performing a tolerance analysis on the mechanical design. Therefore, the bias parameters can be bounded even though the bias characteristics are unknown for each individual drive.

The research proposes fulfilling the rotary shock resistance requirements using a pure magnetic bias that results in reduced cost and virtually none of the issues mentioned above. In this research, an actuator is designed based on typical design constraints used in the disk drive industry. An initial lumped parameter design was carried out first to quickly get an idea of the optimized coil geometry and air gap flux density. To further refine the lumped parameter results into a more realistic representation, a solid model of the actuator was created with the actual geometric constraints resulting in a more distributed parameter design. Magnetic and structural finite element methods were used to give a more accurate value of the coil inductance, arm inertia, and air gap flux density. Using the previously calculated arm inertia and a predetermined sweep angle, a bias feature is designed to restore the arm back to the nominal shipping location after the impact of a rotary shock. The actuator is manufactured according to a proposed set of design specifications and the motor physical parameters are measured. A third-order dynamic model for the actuator with the added bias feature is developed. Bounds on the magnetic bias magnitude and position are determined relative to geometric tolerance studies. A stable, model-based, adaptive seek controller is designed and experiments are conducted using a laser vi-

brometer for position and velocity feedback. A performance comparison is made on the effects of sample rate and accuracy of nominal bias approximation. A projection algorithm is also implemented to limit the bias estimate to within the known bounding tolerances. The adaptive controller requires measurement feedback availability of all system states. However, disk drives do not typically possess this direct measurement capability in production. Therefore, an output feedback controller is developed to estimate the states and control the actuator under magnetic bias influence. The design is constructed based only on current measurement with specific assumptions on the nonlinearity. Experiments are performed to verify the design.

As previously mentioned, rotational shocks can be suppressed by implementing an external bias or latching mechanism that holds the disk drive actuator and R/W heads at the disk inner radius in the absence of power. These methods, however, will not provide adequate protection from linear shocks. To provide linear shock robustness, manufacturers design the R/W heads to rest on a "textured", circumferential band at the disk inner radius (Fig 1.4). The texture prevents any adherence of the R/W heads to the disk and provides an area of contact away from the data zone in the presence of linear shocks. Therefore, any head/disk interference (HDI) will occur in the texture zone where no data is present. This method has proven to be relatively effective and is currently used in enterprise and server-class drives susceptible to less frequent, low amplitude shock levels. However, drives scheduled for notebook computers and consumer electronic devices will naturally experience higher shock levels. Frequent and severe HDI will cause media divots in the zone textured area (Fig 1.5). When power is applied and the disks begin to spin, these divots can disrupt the airflow and actually contact the heads causing catastrophic failure during the disk spin-up process.

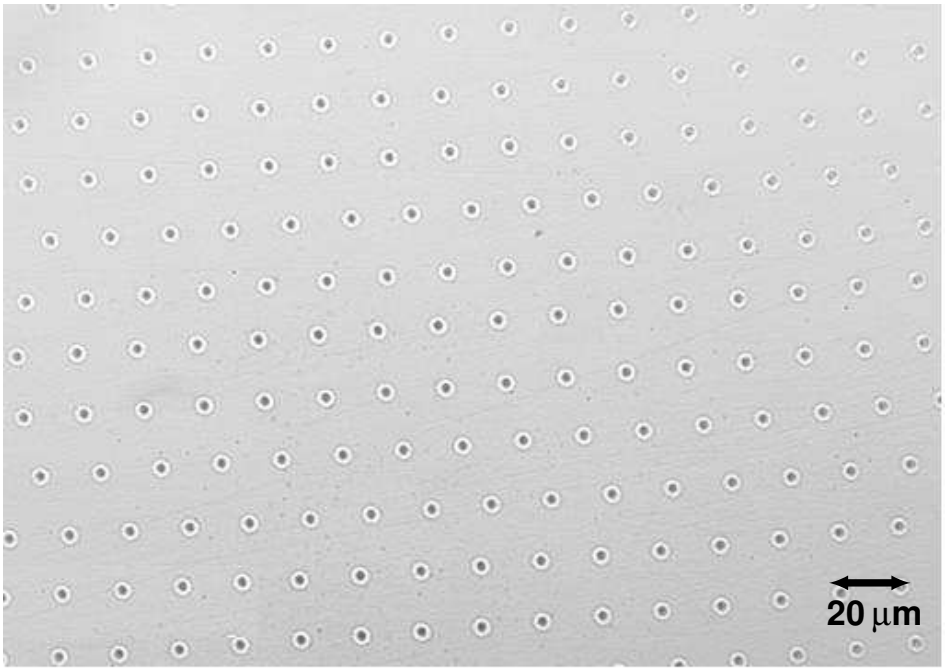

Figure 1.4: Laser zone texture at inner radius

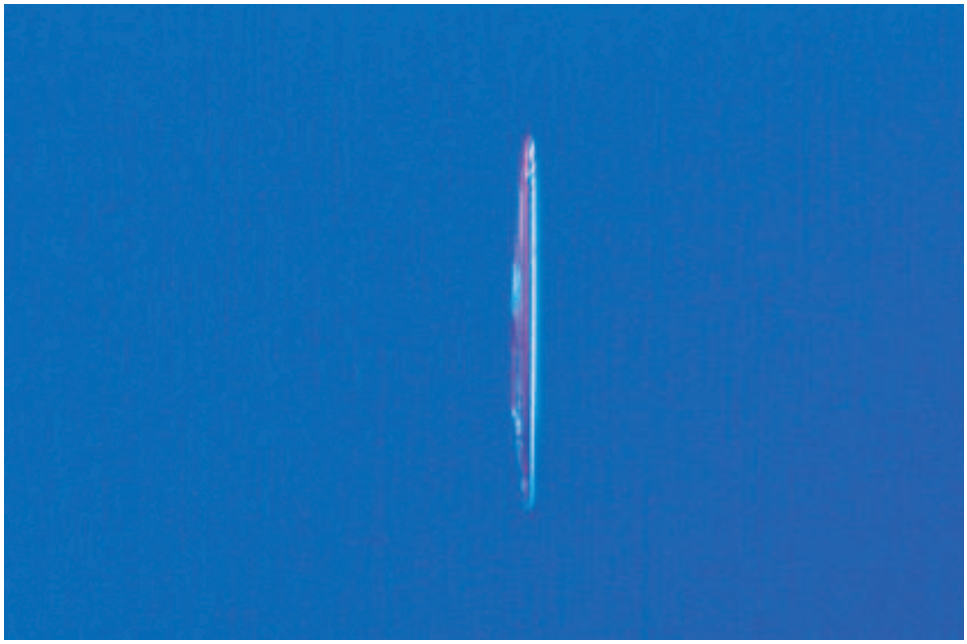

Figure 1.5: Disk damage resulting from linear shock HDI

To combat the issue, many disk drive manufacturers prefer to keep the heads completely off the disks when the drive is not operating. The common method adopted in industry is to park the tip of the actuator on a ramp located outside the disk outer diameter [9]. Figure 1.6 shows a typical non-operational configuration with actuator parked on a ramp and heads suspended off the disks. When the drive is powered on, the actuator moves the heads off the ramp and onto the disks where normal operation occurs. When the drive is powered off, residual energy from the disk spindle motor back-emf is used to move the actuator, unloading the heads off the disks and onto the ramp. One issue that has had much attention recently is the effects of HDI during the loading process and how to prevent it. Figure 1.7 shows an example of HDI from ramp loading where the edge of the R/W head has created a divot in the disk. It has been shown that HDI during loading is primarily dependent on vertical loading velocity along with the pitch and roll angle of the head [10, 11]. These two factors are

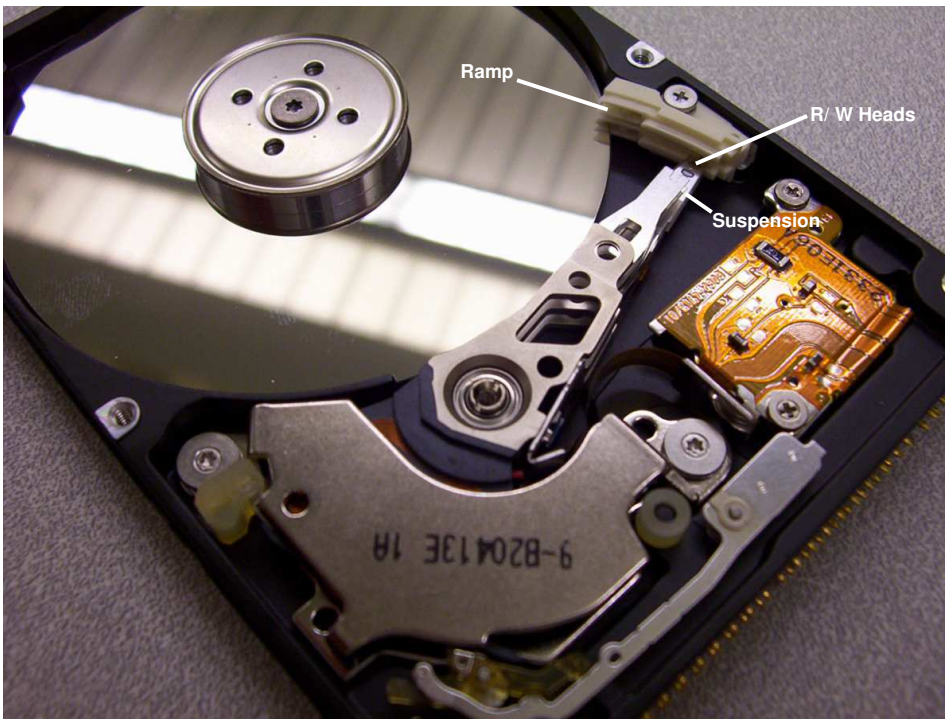

Figure 1.6: Ramp load concept (Courtesy of Fujitsu Corp)

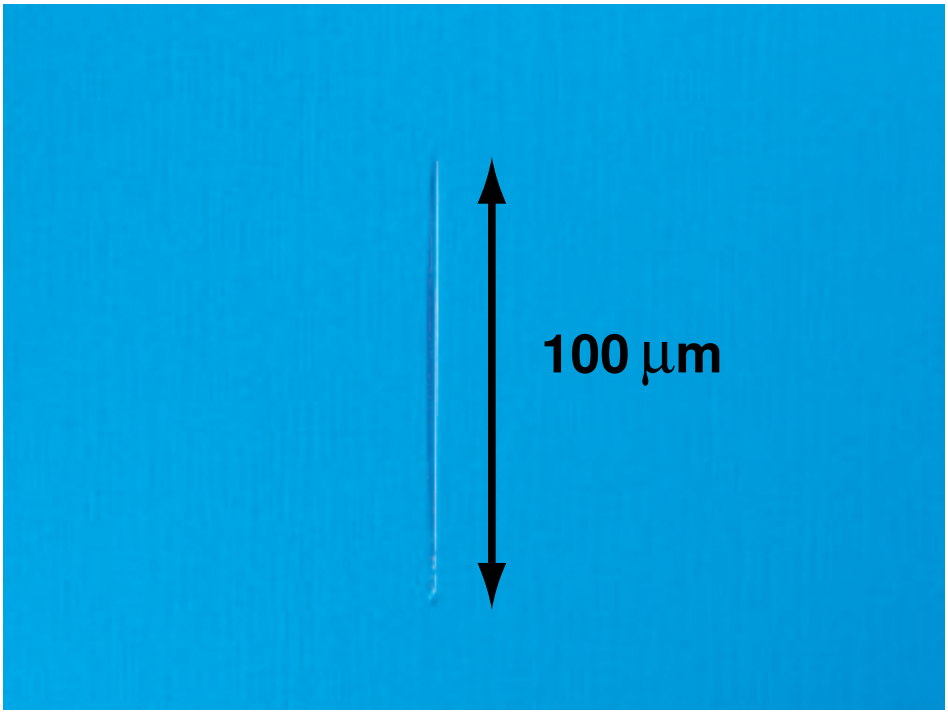

Figure 1.7: Disk damage resulting from ramp loading HDI

a function of the head suspension spring constant, actuator angular velocity, and the ramp incline [12]. The suspension spring force is a very controlled parameter because of the effects of aerodynamics and fly height during operation. It is not likely that this parameter will be adjusted to compensate for ramp loading. Additionally, the ramp incline can be restricted by the geometric limitations of the drive form factor. There is flexibility, however, on the angular velocity parameter and disk drive load/unload (L/UL) controllers typically regulate the velocity moving on and off the ramp. This is usually accomplished by estimating the motor back-emf which is proportional to angular velocity. Therefore, it is advantageous to have an idea of the motor back-emf factor characteristics across the entire stroke. The shape of the motor back-emf or torque factor across the actuator stroke (sweep angle) is dependent on the geometry of the magnets. Most L/UL disk drives will have relatively constant torque factors within the normal operating stroke on the disk and reduce to a lower value on the ramp.

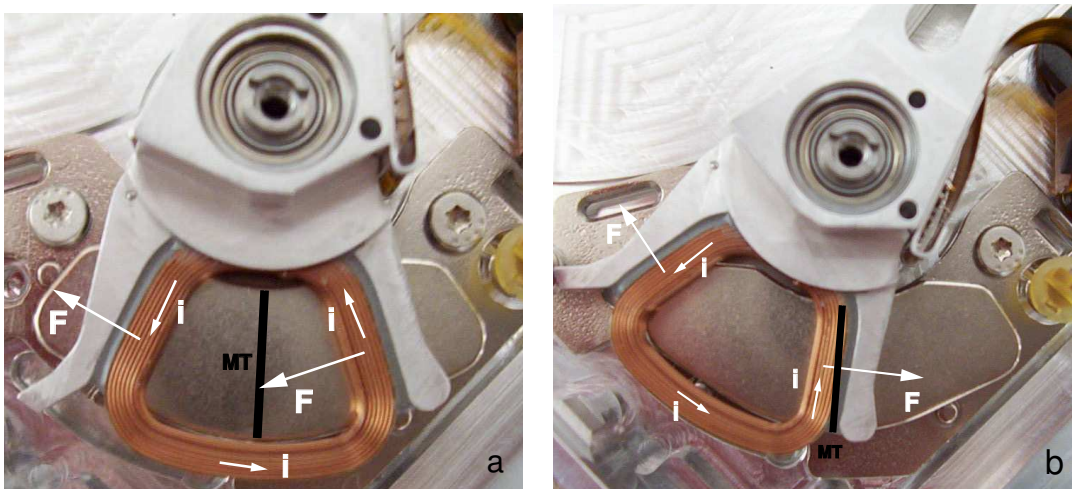

(a) Controllable (b) Uncontrollable

Figure 1.8: Conventional actuator illustrating uncontrollability.

Disk drive actuator magnets are polarized such that the gap flux density is equal and opposite for each of the two active coil lengths inside the air gap. The location where the magnet polarity changes is called the magnetic transition (MT). Because the magnetic flux flow in the air gap has opposite direction on each side of the MT, the current, i, flowing through the coil produces a force, F, in the active lengths as shown in Figure 1.8(a). Each active coil length contributes, roughly, one-half of the total torque produced by the actuator. If the actuator continues to rotate, one active length will cross the MT where both active lengths are subject to magnetic flux flow in the *same* direction. In this case, the actuator stops resulting from equal and opposite forces imparted to each coil active length (Fig. 1.8(b)). Because both active coil lengths are influenced equally by similar flux density, the actuator cannot be moved from this position by applying current through the coil. The condition depicted in Figure 1.8(b) renders the system uncontrollable. Increasing the coil and magnet arc length is the solution that is currently used in industry. The magnet arc length increase effectively changes the MT location and prevents both active coil lengths from overlapping the MT. This accounts for the extra stroke angle that must

be traveled to access the ramp past the outer disk diameter without going through the uncontrollable condition. However, increasing the coil size increases the inertia of the actuator, reducing seek performance. Seek performance is also influenced by the magnet surface area. The air gap magnetic flux density is inversely proportional to the magnet surface area. Increasing the magnet surface area effectively reduces the amount of torque generated by the actuator. Also since magnet cost is directly related to the physical volume of material, a cost increase will result from increasing the magnet size. In fact, depending on product sales volume, the cost increase for a given product could be in the millions of dollars. Therefore, implementing the ramp L/UL solution results in a significant cost increase from increased magnet volume. Additionally, a torque reduction is realized along with an inertia increase which are both detrimental to seek time performance. Figure 1.9 exhibits the extra magnet required for a nominal ramp load actuator design.

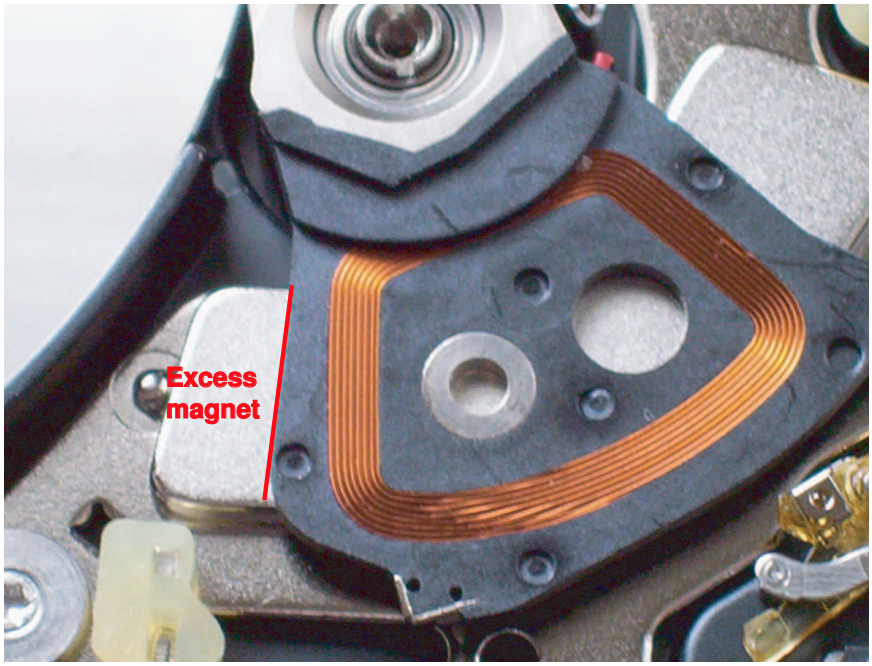

Figure 1.9: Left of the red line depicts additional magnet material required specifically to provide actuation while maneuvering on the ramp.

One concept that has been proposed uses a conventional actuator to perform the L/UL operation [13, 14]. The design requires the actuator coil active lengths to travel over and through the MT which presents an uncontrollable set in the state-space. To promote travel through the uncontrollable set, a special head loading algorithm was developed. It was proposed that current be applied through the coil to move the actuator in a specific direction. Current is then removed from the coil when both active lengths cross the MT and reapplied with opposite polarity to keep the actuator moving in the same direction (Fig. 1.10). The maneuver is performed open-loop using a set of voltage pulses. The pulse widths and amplitudes are tuned until a successful loading is achieved. However, because of the open-loop nature of the system, there is no knowledge of the actual loading velocity. Distributions will exist in the actuator physical parameters for large production volumes and it may be difficult if not impossible to achieve a desired loading velocity using open-loop voltage pulses. Furthermore, factors such as disk windage, temperature, and ramp wear could cause variations in loading velocity over the life of a product. Therefore, a closed-loop solution is necessary.

There has been much discussion in the literature about dealing with uncontrollable sets, but most techniques promote avoidance. However, for the ramp loading design with conventional actuator, the set is unavoidable and must be reached to complete the control maneuver. Furthermore, an input singularity is also exhibited on the uncontrollable set. Therefore, from an input-output perspective, the system relative degree is not well defined. Previous research investigating system characteristics at or near input singularities primarily propose system approximation methods. In [15], a method is developed for reference trajectory tracking of systems through singular points. A control law is designed based on an approximation of the true system by neglecting higher order terms that would result in a definitive input/output map.

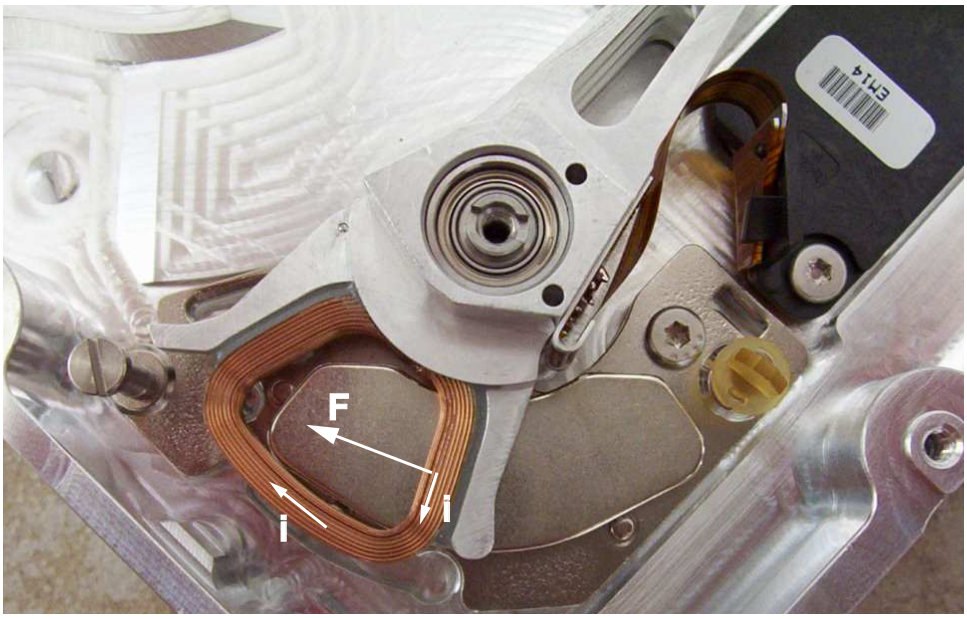

Figure 1.10: Actuator after traveling through MT. Current polarity is reversed.

Bounded tracking is only guaranteed in a neighborhood of the true system singular points because the neglected terms may become significant further away from the singular condtion. System characteristics are defined and presented as necessary conditions for stability of the error dynamics under the proposed control law. The ball and beam system (BBS) exhibits an ill-defined relative degree and was used extensively as a demonstrative platform for studying this phenomena. The work of [15] was extended in [16] to systems with uncertain parameters. An adaptive control law was derived to produce bounded tracking and parameter estimates. The control law was based on the approximate model of [15] while the parameter update law was derived from an observer based on the exact model. The authors continued with a refined control law in [17] using exact input-output tracking away from the singular condition and switched to the approximate law of [15] within some threshold. The switching scheme included an exponential term to ensure a finite switching rate. The control law required the necessary conditions of [15] in addition to a "slowly varying" reference trajectory near singular points and stable zero dynamics. The

BBS was used for controller evaluation. A similar switching control scheme (without the exponential term) was introduced in [18] and extensive analysis was performed to determined what affect the zero dynamics would have on the control performance. Sufficient conditions were given for bounded tracking and, again, the BBS was used as a demonstrative platform. The results in [19] show that the switching control scheme proposed in [18] is applicable for a wider class of nonlinear systems. When the region of the approximate linearization control law is attractive to the exact zero dynamics, it is possible that the closed-loop system under the switching control scheme is still stable. Approximate tracking through the input singularity requires the system to satisfy local controllability within the region of operation. The commutational ramp load actuator, however, possesses an uncontrollable condition that coincides with an input singularity.

This work focuses on the design, integration, analysis, and implementation of a disk drive actuator with a unique application to ramp loading. The design eliminates material costs from larger magnets and coils typically inherited with ramp load designs. Therefore, the shock resistance of ramp loading is retained while realizing the cost and performance benefits of a conventional actuator. A reference model of the system is derived along with an extensive study of the system dynamic behavior. A sufficient condition is developed to facilitate a maneuver through an uncontrollable, singularity along the ramp. A trajectory is generated to specifically fulfill the requirement when tracked using closed-loop control. A formal procedure is developed outlining the trajectory design method along with stable, state-feedback and output feedback controllers designed to track the trajectory. A disk drive is fabricated with the unique actuator to support ramp loading. Experiments are performed to verify the overall design concept.

The research focuses on enhanced mechanical and servo controller designs for disk drives that reduce cost and eliminate quality concerns associated with suppressing the

effects of non-operational shocks. The contributions of this research are summarized as follows:

- A method of magnetic bias design to meet specific rotational shock performance requirements is discussed. Magnetic finite element analysis is employed to design a bias capable of resisting a rotational shock specified with a half-sine acceleration amplitude and duration. The magnetic bias energy is required to be greater than the energy produced by the shock calculated over the actuator sweep angle. A formal derivation and computational process is given.

- Many issues exist for current methods of rotational shock resistance. A magnetic bias solution presents the best option from a quality and cost perspective. However, the magnetic bias solution is not popular because of the associated servo control issues. New controllers are developed that allow for the use of a pure magnetic bias while maintaining seek performance. Robustness issues are also handled with knowledge of bias distributions for a large population of drives. The results are substantiated with experiments.

- Accurate modeling of the magnetic bias requires an increase in model complexity. An increase in memory or processor capability is required to perform the calculations necessary for the control law computation. It is suggested, however, that a sample rate increase could recover some of the performance lost by reducing modeling accuracy. Therefore, a feasible solution would still be available for applications that are memory or processor limited. A comparative study was conducted to determine performance trade-offs between modeling accuracy of the magnetic bias and available sample rate resulting from computational requirements. Experimental results form the basis of the conclusions.

- Much work has been done on detection and avoidance of uncontrollable sets in a system state space. Since the ramp load problem does not allow for avoidance,

the system must pass through the uncontrollable set. A sufficient condition is derived that guarantees maneuvering through an uncontrollable, singular manifold. A trajectory generation methodology, based on the sufficient condition, is presented that allows for successful passage through the system uncontrollable, singularity.

- Ramp loading is a common method of preventing damage resulting from non-operational linear shocks. However, a cost increase and performance reduction is realized using existing ramp loading techniques. A new mechanical design and closed-loop control scheme is developed to realize the shock benefits of ramp loading while preserving the enhanced seek performance and cost reduction benefits of a conventional, non-ramp load actuator.

Chapter 2 details a mechanical design solution for rotary shock performance. The actuator with magnetic bias is designed corresponding to associated design constraints. A dynamic model of the actuator is developed to include the nonlinearity due to the arm bias. Two control strategies are proposed in Chapter 3 and comparative experimental results are discussed. The ramp load design solution is presented in Chapter 4 and a unique disk drive is fabricated to support commutational ramp loading corresponding to the proposed design. Measurements are taken of the actuator physical parameters to verify the design. Dynamic analysis of the commutational ramp load actuator system behavior is given in Chapter 5 where a sufficient condition for moving through uncontrollable, singular points is presented. Chapter 6 details a trajectory generation strategy that maneuvers the actuator through the uncontrollable region when tracked using closed loop control. Stable, state-feedback and output feedback controllers are designed to track the proposed trajectory. Experiments are conducted to verify and validate the overall commutational ramp load concept. A final summary and description of future work is given in Chapter 7.

CHAPTER 2

ACTUATOR DESIGN WITH NONLINEAR MAGNETIC BIAS

From a product quality and cost reduction perspective, a pure magnetic bias design is advantageous for suppressing the effects of non-operational, rotary shocks in disk drives. However, a pure magnetic bias is rarely used because it is nonlinear and reduces seek controller performance. This chapter discusses the requirements and methods for design of a disk drive actuator a with pure magnetic bias. The design constraints are addressed in Section 2.1 where special consideration is given to form factor geometry, magnetic flux leakage, and rotational shock performance. The actuator and magnetic bias design are developed in Section 2.2. A dynamic model of the actuator that includes the nonlinearity due to the arm bias is given in Section 2.3. A summary of conclusions is given in Section 2.4. The control problem will be addressed in Chapter 3.

2.1 Design Constraints

Before beginning the actuator design, certain performance requirements must be defined. The move-time is defined as the time required by the actuator to move the arm from an initial location on the disk to the neighborhood of a desired destination. The third-stroke move-time is the time required to move one-third of the total available sweep angle. The settle time is defined as the time required by the actuator to converge on the desired destination within the neighborhood. The seek time is the sum of the move and settle-time. An obvious approach to improving move-time would be to increase the available power. However, customer constraints and industry

Table 2.1: Actuator performance requirements

Parameter	Spec
Max move-time	10 msec
Move power	6.5 W
Max PCB Flux leakage	100 Gauss
Coil mass	3.2 grams
Rotary shock amplitude	40 krad/s^2
Rotary shock pulse width	2 msec
Voltage Saturation limit	11 V

standards limit the amount of overall power a given disk drive can consume and move power factors into that limitation. Mounted below the actuator is a printed circuit board (PCB) that contains the disk drive electronics. In order to reduce the effects of electromagnetic interference and prevent small ferrous particles from adhering to the PCB, a maximum actuator flux leakage specification is required at the PCB surface. As previously mentioned, operating and non-operating shock disturbances can be detrimental and even fatal to disk drive performance. Robustness to operational shock and vibration are achieved by minimizing the arm imbalance. A constraint on the voice-coil mass is necessary to meet the imbalance requirements. In the case of a non-operational rotational shock, a maximum limit is specified that the latching mechanism is guaranteed to meet. The performance requirements being considered for this particular disk drive application are given in Table 2.1. Industry standards limit the size or form-factor of a disk drive and therefore the size of the actuator. This limitation restricts the height and profile of the magnetic circuit. The actuator is typically mounted in one corner of the drive shell and allowed to extend out to the arm pivot location. The PCB, base mounting shell, cover, and magnetic circuit thickness must all sum to less than the form-factor height. The voice-coil profile is

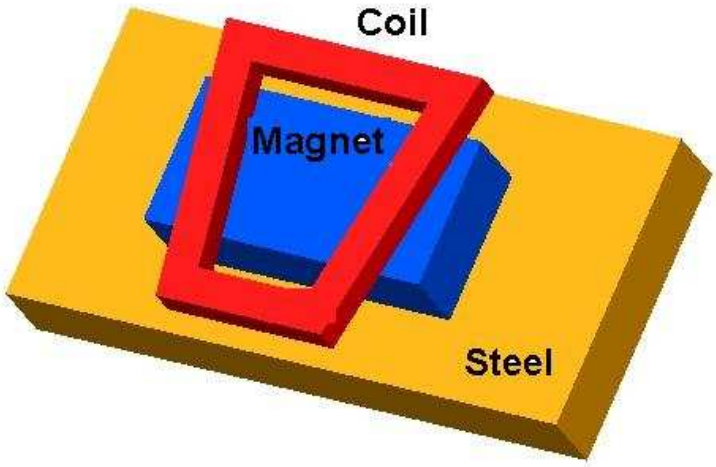

Figure 2.1: Lumped actuator profile showing bottom half with coil

limited by the sweep angle or total stroke of the actuator. The geometric constraints imposed on the actuator profile, height, and sweep angle were 1246 mm^2, 1575 mm, and 32°, respectively.

2.2 Design Methods

The following section describes the voice-coil motor design procedure. A lumped parameter model for the coil and magnetic circuit is developed. The design is further refined in Section 2.2.2 using finite-element modeling and compared to the lumped design. In Section 2.2.3 a magnetic bias is designed to restore the actuator arm back to the nominal shipping location after the impact of a rotational shock.

2.2.1 Lumped Parameter Design

To quickly get a reasonable estimate of the performance, a lumped parameter model was established and analyzed. An initial profile for the actuator components was developed based on the geometric profile constraints and shown in Figure 2.1. Given the coil profile constraints, a trapezoidal shape was assumed having an average mean

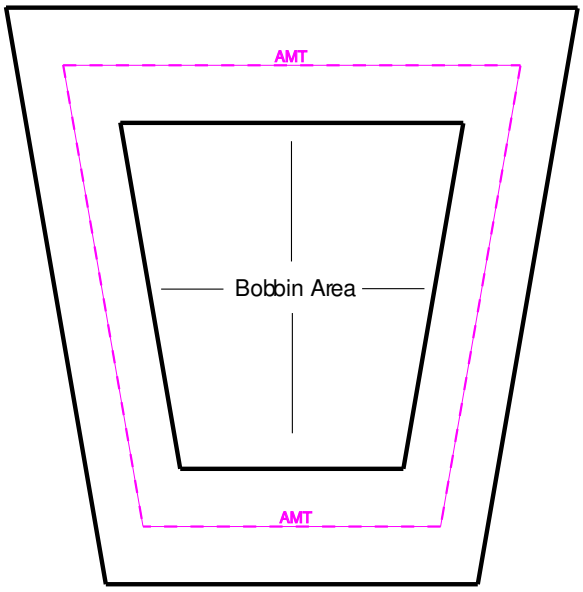

Figure 2.2: Lumped parameter coil profile

turn length of 200.2 mm. The average mean turn (AMT) length is noted as the dotted line in Figure 2.2 and the bobbin is the trapezoidal interior that the coil wire is wound around. In order to balance the arm, a coil mass of 3.2 grams was required and pure copper was selected as the material for the conductor. Iteration on the diameter and length was performed until the mass and profile targets were met. A diameter of 0.183 mm was selected to give a total wire length of 10 m. The resistance, R, of the wire was calculated using

$$R = \rho \frac{l_w}{A_w} \tag{2.1}$$

where ρ is the resistivity of copper and l_w and A_w are the length and cross-sectional area of the wire, respectively. The inductance, L, is a function of the geometry of the coil and the number of turns according to [20]

$$L = \frac{N^2 \mu_o A_b}{t_c} \tag{2.2}$$

where N is the number of turns, $\mu_o = 4\pi \times 10^{-7}$ is the permeability of air, A_b is the trapezoidal area of the bobbin, and t_c is the coil axial thickness. Table 2.2 lists the results from the coil lumped parameter design. The coil design coupled

Table 2.2: Coil design parameters

Parameter	Spec
Wire diam. (d_w)	0.183 mm
Mean turn (l_c)	200.2 mm
Bobbin area (A_b)	131.7 mm^2
Thickness (t_c)	3.05 mm
Turns (N)	223
Resistance (R)	8.7 Ω
Inductance (L)	2.7 mH
Mass (m_c)	3.2 grams

with the actuator arm resulted in a motor inertia of 47.31 g $\cdot$ cm^2. A standard, lumped parameter method [21] was used for the magnetic circuit design based on the geometric constraints. The general configuration for the magnetic circuit of the actuator is a tandem C-core as shown in Figure 2.3. The overall height and profile of the motor is designed to maximize the available space. The magnet and steel thickness are optimized to magnetically saturate the steel without exceeding the flux leakage specification. Each magnet is polarized using the configuration shown in Figure 2.3 where N and S represent a north and south pole, respectively. A lumped estimate of the circuit performance can be calculated using a simplified version of Maxwell's equations [22]. The total magnetic flux, Φ, flowing through the circuit is constant and can be represented by

$$\Phi = B_m A_m = B_g A_g = B_s A_s \tag{2.3}$$

where B_m, B_g, and B_s are the flux densities of the magnet, air gap, and steel, respectively and A_m, A_g, and A_s are the corresponding cross-sectional areas. The

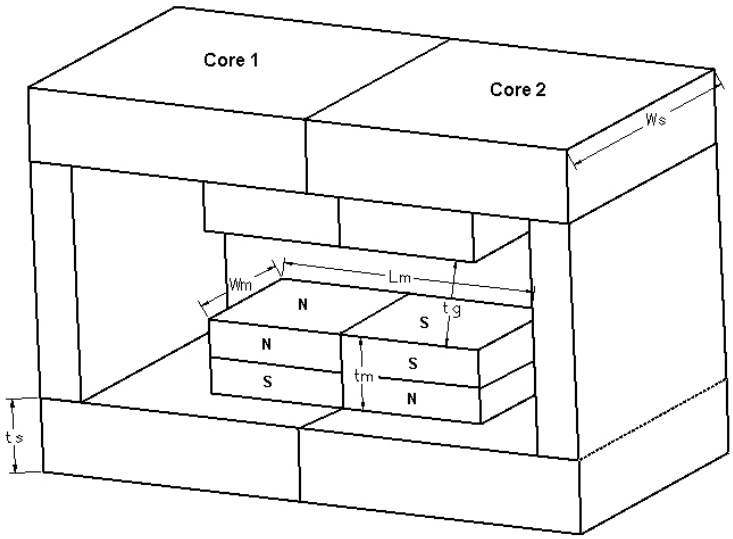

Figure 2.3: General tandem C-core actuator configuration

magnetizing force around the C-core loop yields the current spanning that loop

$$i = H_m t_m + H_g t_g + H_s l_s \tag{2.4}$$

where i is the loop current and H_m, H_g, and H_s are the magnetizing force of the magnet, air gap, and steel, respectively. The variables t_m and t_g are the magnet thickness and air gap thickness, respectively. The steel length, l_s, is the median distance the flux travels through the steel. Because permanent magnets in air do not generate current and the steel is assumed to have infinite permeability ($H_s = 0$), Equation (2.4) reduces to

$$H_m t_m + H_g t_g = 0. \tag{2.5}$$

Ampere's law defines the relationship of magnetic properties in the air gap as

$$B_g = \mu_o H_g \tag{2.6}$$

From Figure 2.3, W_m and L_m are the geometric width and length of a whole magnet, respectively. Noting that $A_m = A_g = 0.5 W_m L_m$ for the C-core circuit and combining equations (2.3), (2.5), and (2.6), a relationship is provided between the magnet

Table 2.3: Lumped parameter magnetic circuit design

Parameter	Spec
Overall height	15.75 mm
Steel transition length	22.66 mm
Steel thickness	3.02 mm
Magnet thickness	2.89 mm
Magnet area	216.7 mm^2
Air gap thickness	3.91 mm
Steel saturation	1.7 Tesla
Air gap flux density	0.806 Tesla

parameters B_m and H_m as a function of only the magnet and air gap thickness,

$$\frac{B_m}{\mu_o H_m} = -\frac{2t_m}{t_g}. \tag{2.7}$$

Therefore the operating point of the magnetic circuit can be determined using equation (2.6) and the demagnetization characteristics of a high energy magnetic material selected to fulfill the design requirements. The air gap thickness, t_g, is fixed by the coil thickness and a clearance of 0.43 mm on each side of the coil for a total air gap thickness of $t_g = 3.91$ mm. The design was optimized by iterating for t_m and t_s using equations (2.3), (2.7), and the demagnetization characteristics until a desired steel saturation level of 1.7 Tesla was achieved. The optimized values of t_m and t_s were determined to be 2.89 mm and 3.02 mm, respectively for a gap flux density of 0.806 Tesla. The magnetic circuit parameters are summarized in Table 2.3. Using the coil design information along with the magnetic circuit parameters, the motor torque factor, K_t, can be calculated as

$$K_t = 2NB_g l_a \tag{2.8}$$

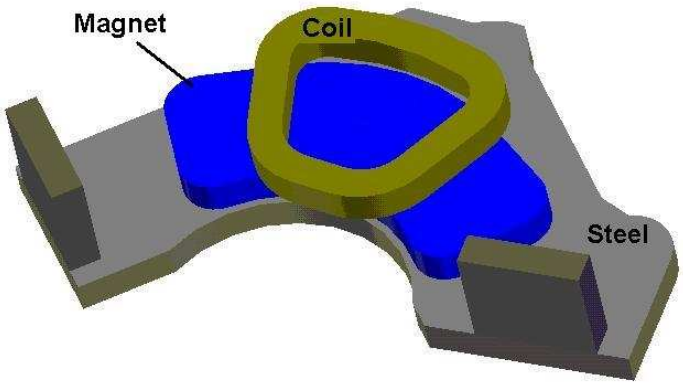

Figure 2.4: Distributed actuator geometry showing bottom half with coil

where l_a is the distance from the arm pivot to the midpoint of the coil active length. The active length of the coil is defined as the portion of the coil inside the air gap. Based on the computed coil and magnetic circuit parameters, the torque factor was determined to be $K_t = 87$ N-mm/amp.

2.2.2 Distributed Parameter Design

The lumped parameter design in the previous section provided a satisfactory initial design. However, assumptions made in the lumped design typically result in overestimates of the performance parameters once the design is manufactured. It was desired to more accurately predict the performance of the actuator and further refine the system by simulating with finite-element modeling (FEM). A solid model was defined (Fig. 2.4) representing all of the internal drive geometric constraints and an initial finite-element mesh was generated using the geometric design parameters described in the previous section as a starting point.

The coil thickness remained 3.05 mm, but the profile was contoured as in Figure 2.4. The FEM estimate of the coil inductance was 1.15 mH which is lower than that estimated from the lumped design. The finite-element coil geometry is shown

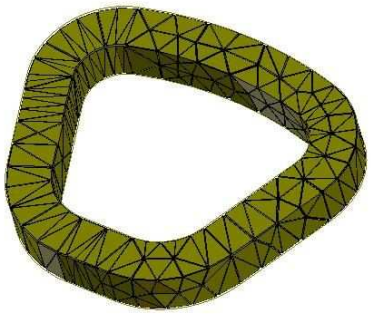

Figure 2.5: FEM coil geometry

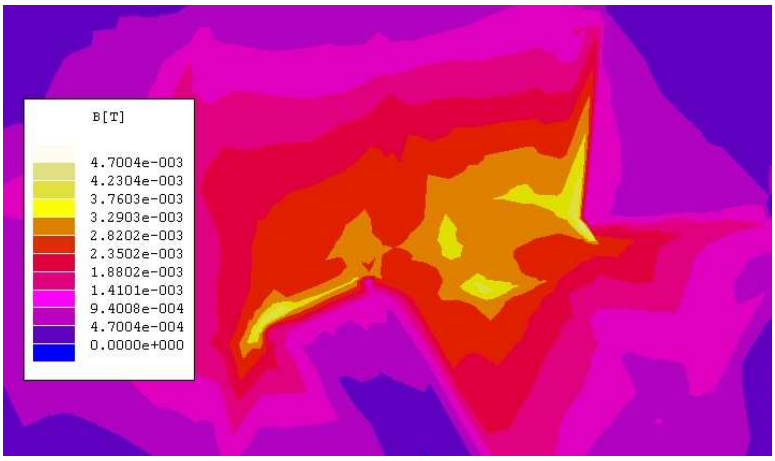

Figure 2.6: Magnetic circuit leakage at PCB (FEM results)

in Figure 2.5. The PCB is approximately 4.27 mm below the bottom steel plate of the actuator. It was desired to keep the leakage flux density below 50 Gauss at the PCB meeting the requirement given in Table 2.1. Beginning with the lumped parameter values, the steel and magnet thicknesses were slightly varied until this value was reached. Steel and magnet thickness of 2.92 mm and 3.0 mm, respectively resulted in a flux leakage limit of approximately 47 Gauss at the PCB (Fig 2.6). The maximum air gap flux density from FEM was 0.78 Tesla (Fig 2.7) which is 3.7% lower than predicted from the lumped parameter model. The peak torque factor was computed to be 14% lower than the lumped estimate. The results are summarized in Table 2.4.

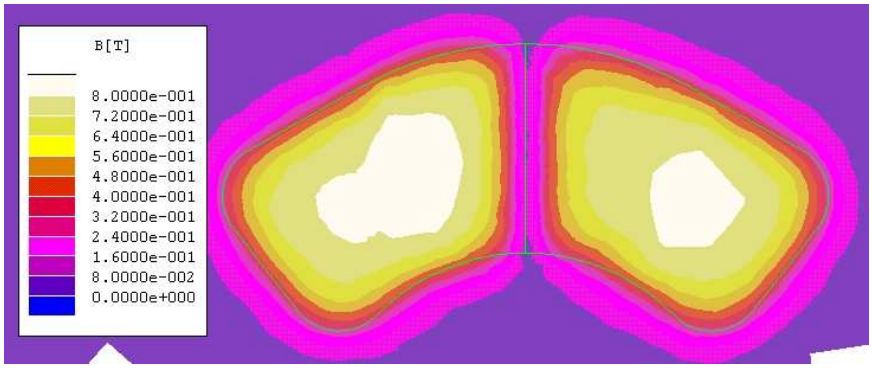

Figure 2.7: Magnetic circuit air gap flux density (FEM results)

Table 2.4: Dynamic model parameter comparison

Parameter	Lumped	Distributed
Torque factor (K_t)	87 N-mm/amp	75 N-mm/amp
Inertia (J)	47.31 g-cm^2	47.31 g-cm^2
Coil resistance (R)	8.7 Ω	8.7 Ω
Coil inductance (L)	2.6 mH	1.15 mH
Voltage limit (V_{max})	11 Volts	11 Volts
Move angle (θ_f)	10.6°	10.6°

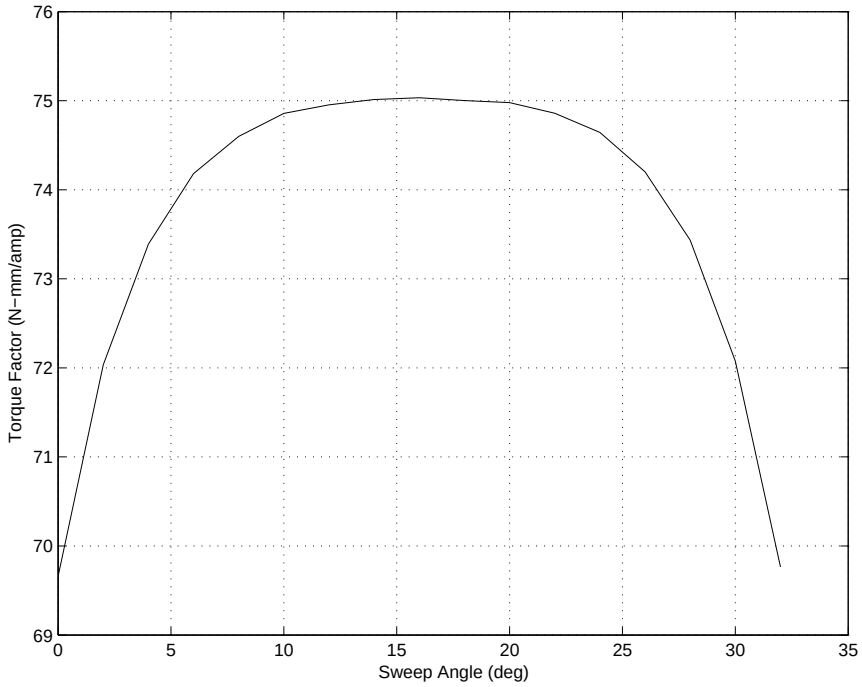

Figure 2.8: Torque factor profile

Variation of the flux density at the air gap edges causes nonlinearity in the torque factor at the sweep angle extremes. The torque factor computed throughout the sweep angle is shown in Figure 2.8. The value of the torque factor at the sweep angle extremes is 7.3% lower than the center.

2.2.3 Magnetic Bias Design

It was necessary to design a bias force across the sweep angle to restore the arm back to the nominal shipping location after the impact of a rotational shock. The angular acceleration of the shock, α_s, is specified as a half-sine pulse [23, 24]

$$\alpha_s(t) = A_p \sin\left(\frac{\pi}{\tau}\, t\right) \tag{2.9}$$

where A_p is the maximum shock amplitude and τ is the shock pulse width. Integration of (2.9) with respect to time using $\alpha_s(0) = \omega_s(0) = 0$ gives the angular velocity

$$\omega_s(t) = \frac{\tau A_p}{\pi}\left[1 - \cos\left(\frac{\pi}{\tau}\, t\right)\right]. \tag{2.10}$$

The torque on the arm resulting from the shock can be described by

$$T_s(t) = J\alpha_s(t) = JA_p \sin\left(\frac{\pi}{\tau}t\right) \tag{2.11}$$

and the total energy, E_s, of the shock is the time integral of the shock power, $P_s = T_s\omega_s$, over the pulse width. After integrating and simplifying,

$$E_s(t) = \int_0^\tau T_s(t)\omega_s(t)dt = \frac{2J(A_p\tau)^2}{\pi^2}. \tag{2.12}$$

The energy of a bias torque, E_b, can be computed from

$$E_b = \int_0^{\theta_T} \psi(\theta)d\theta \tag{2.13}$$

where $\psi(\theta)$ is the bias torque as a function of the arm sweep angle, θ_T. The strategy is to design a bias torque that applies an energy equivalent to that of the shock ($E_b = E_s$) and bring the arm to rest after traveling a desired angular displacement. Using equations (2.10) through (2.12) and the shock specifications, the shock energy was determined to be 6.13 mJ. Therefore, if a *constant* bias is chosen to bring the arm to rest within the total sweep angle, the magnitude of the bias torque required is

$$\psi = \frac{E_s}{\theta_T} = 11 \text{ N-mm}. \tag{2.14}$$

Ideally, a constant and passive bias torque would be most desirable for controller design. A passive bias can be obtained by pressing a steel pin into the actuator arm, partially protruding into the air gap of the magnetic circuit as shown in Figure 2.9. A force is generated proportional to the flux density gradient in the steel feature at the corresponding location. Shaping of the torque profile can be achieved by changing the location and size of the steel member. Depending on the shock specification, the magnetic bias may be required to provide a considerable torque relative to the available torque produced by the actuator. The data flex circuit is typically optimized to minimize bias within the given geometric constraints of the disk drive form

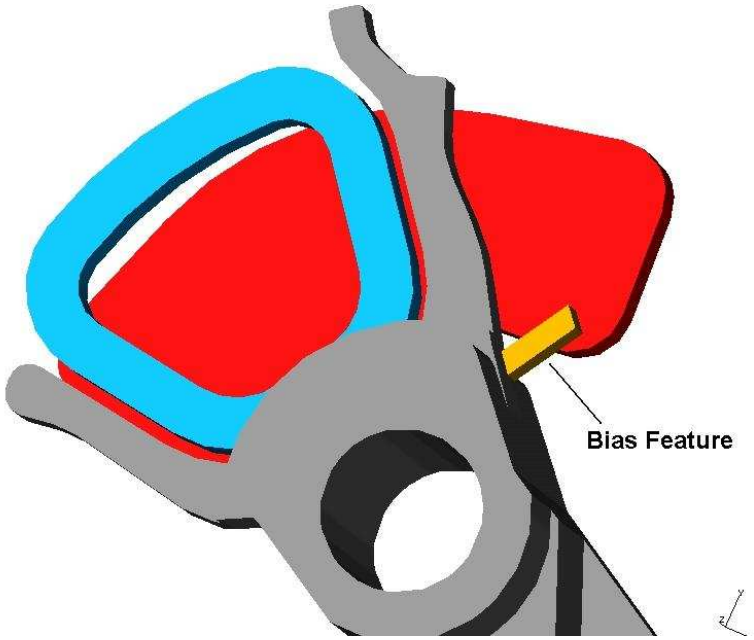

Figure 2.9: Bias feature design on actuator arm

factor. It was shown in [25] that the primary degrees of freedom for optimization of flex circuit design are layer thickness, free length, and slope location of the flex attachment points. Those three parameters can be selected to provide a desired bias characteristic within the constraints. The energy of the torque profile throughout the sweep angle was calculated from (2.13) and desired to be larger than the shock energy computed from (2.12). The resulting bias contribution from flex circuit and magnetic sources is nonlinear and a combined torque profile can be represented as an n-th order polynomial of the form

$$\psi(\theta) = \sum_{k=0}^{n} c_k \theta^k \tag{2.15}$$

where θ is the angular position and c_k is the k-th order coeffiecient.

An actuator was manufactured to meet the modeled performance requirements designed in Section 2.2. The following values of 48.26 g-cm^2, 71.5 N-mm/amp, 8.82 Ω, and 1.11 mH were measured for the inertia, torque factor, resistance, and inductance, respectively. The bias torque was also measured and is shown as a function of actuator sweep angle in Figure 2.10. A fixture was designed that allowed a torque sensor to

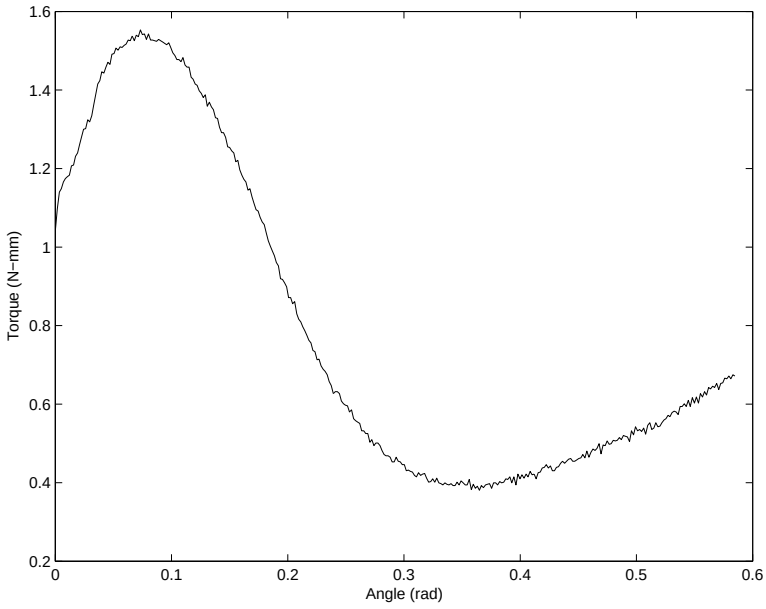

Figure 2.10: Measured magnetic bias torque

be attached directly to the actuator pivot. Beginning with the actuator arm parked at the inner radius of the disks, the bias torque was measured across the entire sweep angle of approximately $\theta_T = 32°$. The final bias concept is shown in Figure 2.11.

2.3 Dynamic Model

Noting that the magnetic bias opposes the arm torque when positive current is applied, the mechanical dynamics of the actuator can be represented as

$$J\ddot{\theta} = K_t\, i - \psi(\theta) \tag{2.16}$$

where θ is the angular position, J is the arm inertia, and K_t is the torque factor as defined in the previous section. The electrical circuit dynamics of the actuator are described by

$$V_s = R\, i + L\frac{di}{dt} + V_b \tag{2.17}$$

where $V_b = K_t\dot{\theta}$ is the back electro-motive force, R and L are as defined in Section 2.2, and V_s is the supply voltage control signal. Choosing the states as $x_1 = \theta,\ x_2 = \dot{\theta}$,

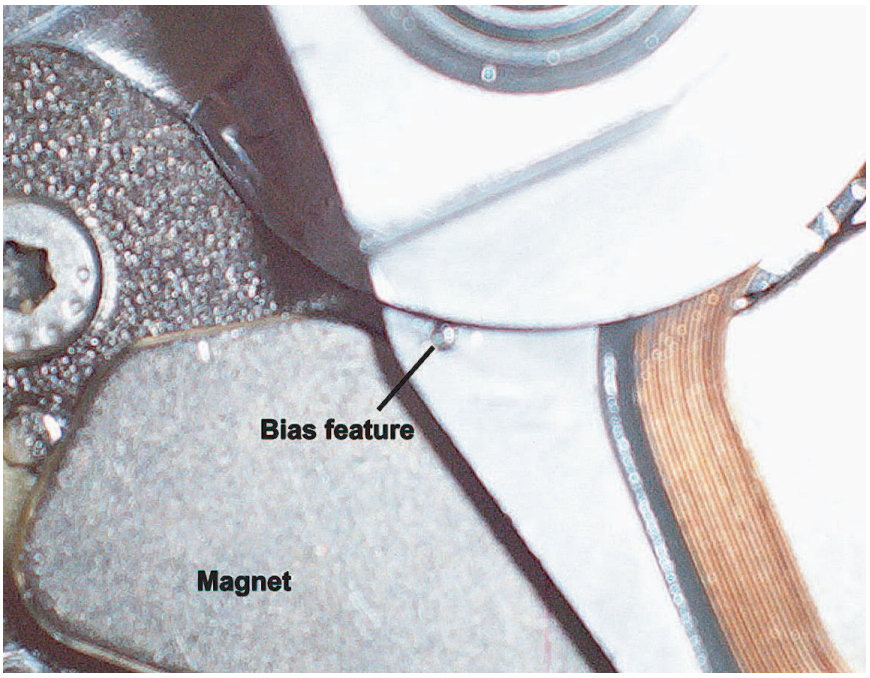

Figure 2.11: Experimental drive magnetic bias concept

$x_3 = i$, and denoting the control input as $u = V_s$, the system can be represented in state-space form as

$$\dot{x} = Ax + Bu - B_\psi \psi(x_1), \tag{2.18}$$

$$A = \begin{bmatrix} 0 & 1 & 0 \\ 0 & 0 & \frac{K_t}{J} \\ 0 & -\frac{K_t}{L} & -\frac{R}{L} \end{bmatrix}, \quad B = \begin{bmatrix} 0 \\ 0 \\ \frac{1}{L} \end{bmatrix}, \quad B_\psi = \begin{bmatrix} 0 \\ \frac{1}{J} \\ 0 \end{bmatrix}.$$

It is noted that the matrix B_ψ, of the bias nonlinearity, is not in the range space of the input matrix, B. Therefore, the system does not satisfy the matching condition.

2.4 Summary

A voice-coil motor actuator for a disk drive was designed to meet specific move-time performance requirements. An initial lumped parameter design was evaluated and followed by a more accurate distributed parameter solution using finite-element analysis.

A comparison revealed the lumped representation to be an ambitious estimate of the distributed design. A non-contact, magnetic bias latching mechanism was designed to fulfill the non-operational, rotary shock requirements. It was determined that the combined flex circuit and magnetic bias torque profile was nonlinear throughout the actuator sweep angle. An actuator was manufactured to meet the desired design requirements and measurements were taken of the motor physical parameters. A third-order dynamic model was developed for the actuator which included the bias force nonlinearity.

CHAPTER 3

SEEK CONTROL WITH NONLINEAR BIAS EFFECTS

The magnetic bias designed to resist non-operational shock affects seek control during the drive operational state. Thus, it is necessary to design a feedback controller that can compensate for the bias. It is also desired that the actuator be capable of tracking a predetermined trajectory generated from a reference model. This chapter investigates multiple control solutions designed to fulfill the tracking task. With the availability of full-state feedback, an adaptive controller is developed that handles the effects of uncertainty in the bias torque. Because full-state feedback is not available in production disk drives, an output feedback controller was also developed using only current measurement. In this case, it is assumed the bias is represented by a known polynomial model which possesses a locally Lipschitz property. Simulations and experiments are conducted to verify performance of both controllers. The first section describes the technique used to generate the model-reference trajectories. Section 3.2 discusses a *linear* state-feedback control design and issues associated with nonlinear bias influence while tracking. The adaptive controller is described in Section 3.3 and 3.4 along with experimental results and a performance trade-off study. The chapter concludes with an output feedback design to address the lack of state measurement in production disk drives.

3.1 Trajectory Generation

To minimize vibration, acoustic energy, and power, it was desired that the reference model produce a smooth trajectory for the controller to track. This was achieved by modeling the trajectory as a high-order polynomial with appropriate boundary conditions [26]. Using the boundary conditions

$$\begin{aligned} &\theta(0) = \dot{\theta}(0) = \ddot{\theta}(0) = \dddot{\theta}(0) = 0 \\ &\dot{\theta}(t_f) = \ddot{\theta}(t_f) = \dddot{\theta}(t_f) = 0 \\ &\theta(t_f) = \theta_f \end{aligned} \tag{3.1}$$

the coefficients, β_k, of a unique seventh-order polynomial

$$\theta_r(t) = \sum_{k=0}^{7} \beta_k t^k \tag{3.2}$$

were determined ($k = 0, 1, \ldots 7$). A trajectory was then defined for $\dot{\theta}_r$, $\ddot{\theta}_r$, and $\dddot{\theta}_r$. The reference trajectory for current was computed from

$$i_r(t) = \frac{J}{K_t}\,\ddot{\theta}_r(t) \tag{3.3}$$

and the reference voltage from

$$V_r(t) = \frac{LJ}{K_t}\,\dddot{\theta}_r(t) + Ri_r(t) + K_t\dot{\theta}_r(t). \tag{3.4}$$

Injecting the reference waveform (3.4) into the corresponding reference model

$$\dot{x}_r = Ax_r + BV_r \tag{3.5}$$

produces the state reference trajectory. A reference trajectory was generated based on (2.18) with the measured physical parameters of Section 2.2.3. It was determined that the fastest third-stroke, state-reference trajectory the system could produce while remaining below the 11 volt saturation level was 9.2 msec. The final reference trajectory move-time will be the target for the subsequent analysis.

3.2 Linear State-Feedback Control Design

The error between the reference trajectory designed in the previous section and the actual state trajectory is defined as $e(t) = x(t) - x_r(t)$. By choosing the control law

$$u(t) = -\mathcal{K}e(t) + V_r, \tag{3.6}$$

the error dynamics can be written by subtracting (3.5) from (2.18) as

$$\dot{e} = \dot{x} - \dot{x}_r = (A - B\mathcal{K})e - B_\psi \psi(x_1) \tag{3.7}$$

It is desired to select the gain vector, $\mathcal{K}$, so that the actual system states track the reference state trajectories, thereby forcing the error dynamics to zero. Choosing a Lyapunov function candidate

$$V(e) = e^\top P e \tag{3.8}$$

where P is a symmetric, positive-definite matrix and taking the derivative of V along the trajectories of (3.7) gives

$$\begin{aligned} \dot{V}(e) &= e^\top (PA_c + A_c^\top P)e - 2e^\top P B_\psi \psi(x_1) \\ &\leq -\lambda_{min}(Q)\|e\|^2 + 2\|e\|\|P\|\|B_\psi \psi(x_1)\| \end{aligned}$$

where P is the solution of the linear time-invariant Lyapunov equation

$$PA_c + A_c^\top P = -Q$$

with $A_c = A - B\mathcal{K}$ and $\lambda_{min}(Q)$ is the minimum eigenvalue of Q. Therefore, tracking error convergence is only guaranteed if

$$\|e\| > \frac{2\lambda_{max}(P)}{\lambda_{min}(Q)}\|B_\psi \Psi(x_1)\|$$

To enlarge the domain of attraction, a stable model-reference adaptive controller is developed in the following section.

3.3 Adaptive Controller Design

One method of compensating for the magnetic bias uncertainty during a seek operation is through implementation of an adaptive controller. The goal is to design an adaptive controller that will estimate the uncertain coefficients of the nonlinear bias in the dynamic model and result in tracking error convergence. To simplify the derivation, the motor physical parameters are defined as

$$\mu_0 = \frac{K_t}{J}, \quad \mu_1 = \frac{1}{J}, \quad \mu_2 = \frac{K_t}{L}, \quad \mu_3 = \frac{R}{L}. \tag{3.9}$$

Further, the nonlinear bias term $\psi(x_1)$ can be defined in the vector form as

$$\psi(x_1) = w^T c \tag{3.10}$$

where $w^\top = [x_1^n, x_1^{n-1}, x_1^{n-2}, \cdots, 1]$ and $c^\top = [c_n, c_{n-1}, c_{n-2}, \cdots, c_0]$. Choosing the control law as

$$u = L(\dot{x}_{3r} + \mu_2 x_{2r} + \mu_3 x_{3r} + u_f), \tag{3.11}$$

the error dynamics using (2.18) are given by

$$\begin{aligned} \dot{e}_1 &= e_2 \\ \dot{e}_2 &= \mu_0 e_3 - \mu_1 w^T c \\ \dot{e}_3 &= -\mu_2 e_2 - \mu_3 e_3 + u_f \end{aligned} \tag{3.12}$$

The signal, u_f, is an auxiliary control signal to be determined later. Two variables, s_1 and s_2 are defined in terms of the tracking error as

$$s_1 = e_2 + \lambda e_1, \tag{3.13}$$

$$s_2 = \mu_0 e_3 - \mu_1 w^T \hat{c} + \alpha_1 e_1 + \alpha_2 e_2 \tag{3.14}$$

where $\hat{c}$ is the estimate of the parameter vector c, and α_1, α_2 are positive gains. The choice of s_1 was developed so that driving $s_1 \to 0$ results in an invariant manifold

such that $e_1, e_2 \to 0$. The selection of s_2 is motivated by the fact that bias is not included in the reference model. Therefore, e_3 should take on some value that is proportional to the current required to offset the effects of magnetic bias. Hence, $s_2 \to 0 \implies \mu_0 e_3 \to \mu_1 w^T \hat{c}$ in order to compensate for bias. The dynamics of s_1 and s_2 can be determined using (3.12) as

$$\dot{s}_1 = -\alpha_1 e_1 - (\alpha_2 - \lambda) e_2 + \mu_1 w^T \tilde{c} + s_2, \tag{3.15}$$

$$\begin{aligned} \dot{s}_2 = &-\mu_0(\mu_2 e_2 + \mu_3 e_3 - \alpha_2 e_3 - u_f) + \alpha_1 e_2 \\ &- \mu_1(x_2 v^T \hat{c} + w^T \dot{\hat{c}} + \alpha_2 w^T c) \end{aligned} \tag{3.16}$$

where $v^T = [n x_1^{n-1}, (n-1) x_1^{n-2}, \cdots, 0]$ and $\tilde{c} = \hat{c} - c$. If the auxiliary control signal, u_f, is chosen to be

$$u_f = \mu_2 e_2 + \mu_3 e_3 - \alpha_2 e_3 - \frac{\alpha_1 e_2 + \alpha_3 s_2 + s_1}{\mu_0} + \frac{\alpha_2 \mu_1 w^T \hat{c} + \mu_1 x_2 v^T \hat{c} + \mu_1 w^T \dot{\hat{c}}}{\mu_0} \tag{3.17}$$

the dynamics of s_2 become

$$\dot{s}_2 = -\alpha_3 s_2 - s_1 + \mu_1 \alpha_2 w^T \tilde{c} \tag{3.18}$$

A Lyapunov function candidate is chosen as

$$V(s_1, s_2, \tilde{c}) = \frac{1}{2}(s_1^2 + s_2^2 + \tilde{c}^\top \Gamma \tilde{c}) \tag{3.19}$$

where Γ is a symmetric positive definite gain matrix. Differentiating V along the trajectories of (3.15) and (3.18), and simplifying, gives

$$\begin{aligned} \dot{V} &= s_1 \dot{s}_1 + s_2 \dot{s}_2 + \dot{\tilde{c}}^\top \Gamma \tilde{c} \\ &= -(\alpha_2 - \lambda) s_1^2 - \alpha_3 s_2^2 - (\alpha_1 - \alpha_2 \lambda + \lambda^2) e_1 s_1 \\ &\quad + \mu_1 s_1 w^T \tilde{c} + \alpha_2 \mu_1 s_2 w^T \tilde{c} + \dot{\tilde{c}}^\top \Gamma \tilde{c}. \end{aligned} \tag{3.20}$$

As previously mentioned, bounds on the bias torque profile are known for a given drive population. This translates to bounds on the bias polynomial coefficients. With this knowledge, consider the function

$$\mathcal{P}(\hat{c}) = \hat{c}^\top \hat{c} - c_u^\top c_u \tag{3.21}$$

where c_u is the known vector of coefficients that constitute the bias polynomial upper bound. A gradient projection algorithm [27] can be used to keep $\hat{c}$ within the convex set $\mathcal{S}$ where

$$\mathcal{S} := \{\hat{c} \in \mathbb{R}^n \,|\, \mathcal{P}(\hat{c}) \leq 0\} \tag{3.22}$$

Now, consider the "smooth projection operator", Proj$(\cdot)$, which will be used to estimate $\hat{c}$ while maintaining (3.22). Let $\dot{\hat{c}} = \text{Proj}(\hat{c}, y)$ where

$$\text{Proj}(\hat{c}, y) = \begin{cases} y, \text{ if } \mathcal{P}(\hat{c}) < 0. \\ \\ y, \text{ if } \mathcal{P}(\hat{c}) = 0 \text{ and } \nabla_{\mathcal{P}}^{\top} y \leq 0. \\ \\ y - \Gamma \dfrac{\nabla_{\mathcal{P}}^{\top} \nabla_{\mathcal{P}}}{\nabla_{\mathcal{P}}^{\top} \Gamma \nabla_{\mathcal{P}}} y, \text{ otherwise,} \end{cases} \tag{3.23}$$

$$y = -\mu_1 (s_1 + \alpha_2 s_2) w^{\top} \Gamma^{-1}, \quad \text{and} \quad \nabla_{\mathcal{P}} = \left[\tfrac{\partial \mathcal{P}}{\partial \hat{c}}\right]^{\top}$$

Using the projection algorithm (3.23) along with the control law (3.11) and (3.17) results in

$$\dot{V} = -(\alpha_2 - \lambda) s_1^2 - \alpha_3 s_2^2 - (\alpha_1 - \alpha_2 \lambda + \lambda^2) e_1 s_1. \tag{3.24}$$

If the gains are chosen such that

$$\alpha_2 > \lambda, \quad \alpha_1 - \alpha_2 \lambda + \lambda^2 = 0, \quad \text{and} \quad \alpha_3 > 0, \tag{3.25}$$

then

$$\dot{V} = -(\alpha_2 - \lambda) s_1^2 - \alpha_3 s_2^2 \leq 0. \tag{3.26}$$

So $s_1 \in L_2 \cap L_\infty$, $s_2 \in L_2 \cap L_\infty$, and $\tilde{c} \in L_\infty$. Further, $\dot{s}_1 \in L_\infty$ and $\dot{s}_2 \in L_\infty$. Using Barbalat's lemma [28], $s_1 \to 0$ and $s_2 \to 0$. Since $s_1 = e_2 + \lambda e_1$, $e_1 \to 0$ and $e_2 \to 0$. Also, $s_2 \to 0 \implies \mu_0 e_3 \to \mu_1 w^T \hat{c}$. Expressing the control law in terms of the tracking error results in the following theorem:

Theorem 3.1 *For the actuator dynamics with nonlinear magnetic bias* (2.18)*, consider the following control law and adaptation law*

$$\begin{aligned} u = L[&\dot{x}_{3r} + \mu_2 x_{2r} + \mu_3 x_{3r} + \left(\rho_{11} + \rho_{12} w^T \Gamma^{-1} w\right) e_1 \\ &+ \left(\rho_{21} + \rho_{22} w^T \Gamma^{-1} w\right) e_2 + \left(\rho_{31} + \rho_{32} w^T \Gamma^{-1} w\right) e_3 \\ &+ \rho_{c1} x_2 v^T \hat{c} + \rho_{c2} w^\top \hat{c} + \rho_{c3} w^T \Gamma^{-1} w w^T \hat{c}] \end{aligned} \tag{3.27}$$

$$\dot{\hat{c}} = \mathrm{Proj}(\hat{c}, y) \tag{3.28}$$

where

$$y = \mu_1^2 \alpha \Gamma^{-1} w w^\top \hat{c} + (\sigma_1 e_1 + \sigma_2 e_2 + \sigma_3 e_3)\Gamma^{-1} w, \tag{3.29}$$

$$\rho_{11} = -\tfrac{(\lambda + \alpha_1 \alpha_3)}{\mu_0}, \qquad \rho_{12} = \tfrac{\mu_1 \sigma_1}{\mu_0},$$

$$\rho_{21} = \tfrac{\mu_2 \mu_0 - \alpha_1 - \alpha_2 \alpha_3 - 1}{\mu_0}, \quad \rho_{22} = \tfrac{\mu_1 \sigma_2}{\mu_0},$$

$$\rho_{31} = \mu_3 - \alpha_2 - \alpha_3, \qquad \rho_{32} = \tfrac{\mu_1 \sigma_3}{\mu_0},$$

$$\rho_{c1} = \tfrac{\mu_1}{\mu_0}, \qquad \rho_{c2} = \tfrac{\mu_1(\alpha_2 + \alpha_3)}{\mu_0}, \qquad \rho_{c3} = \tfrac{\mu_1^3 \alpha_2}{\mu_0},$$

$$\sigma_1 = -\mu_1(\lambda + \alpha_1 \alpha_2), \quad \sigma_2 = -\mu_1(1 + \alpha_2^2), \quad \sigma_3 = -\mu_0 \mu_1 \alpha_2.$$

If the gains α_1, α_2 and λ are chosen such that $\alpha_2 > \lambda$, $\alpha_1 - \alpha_2 \lambda + \lambda^2 = 0$, and $\alpha_3 > 0$, then all the signals, $e_1, e_2, e_3, \hat{c}$, are bounded, and e_1 and e_2 asymptotically converge to zero.

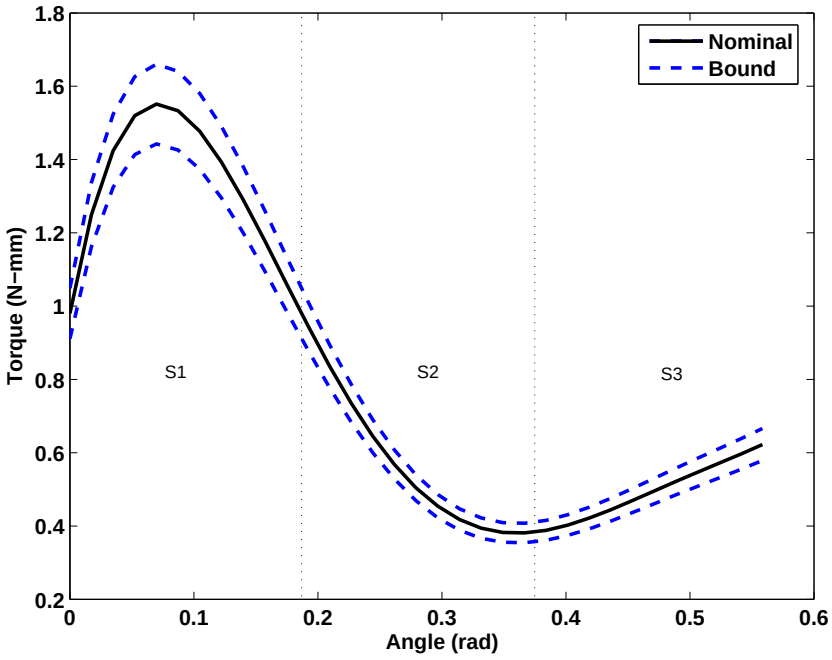

Figure 3.1: Bias torque boundary with tolerance variation

3.3.1 Simulation Results

Simulations were conducted for the control designs developed in the previous sections. All tracking trajectories were designed for a third-stroke move as outlined in the performance requirements. The sweep angle was partitioned into three sectors, S_k, each comprising one-third of the overall stroke, θ_T, where

$$S_k := \left\{ \theta \in \mathbb{R} \mid \frac{(k-1)\theta_T}{3} \leq \theta \leq \frac{k\,\theta_T}{3} \right\}, \; k = 1 \ldots 3 \tag{3.30}$$

where 0 rad corresponds to the disk inner radius. The sectors are illustrated in Figure 3.1. The magnetic force dominates the bias to about 0.3 rad (17.2°). When the actuator rotates to the outer radius, influence from the magnetic field is lost as the bias feature exits the air gap and flex circuit compression torque becomes dominant. Because the largest bias influence and variation exists in S_2, the following discussion is based on results from that sector. Figure 3.1 also shows the bounds on the magnetic

bias computed through tolerance analysis of the magnetic design. The bias was fit to a nominal fifth-order polynomial with coefficients

$$c_5 = 0.4518,\ c_4 = -0.8749,\ c_3 = 0.6232,\ c_2 = -0.1883,\ c_1 = 0.0186,\ c_0 = 0.0098.$$

The geometric tolerance analysis bounds were determined by a $\pm 7\%$ envelope about the nominal polynomial fit. The state-feedback gain vector, $\mathcal{K}$, was selected so that the poles of $A_c = A - B\mathcal{K}$ were at least five times faster than the third-stroke move time target. The desired final time, $t_f = 9.2$ msec ≈ 680 rad/s, suggests that the closed loop poles be located at -3500 rad/s resulting in

$$\mathcal{K} = [3110,\ 2.59,\ 3.37] \tag{3.31}$$

The control was chosen as in (3.6) and simulations were performed for a third-stroke move in S_2. When tracking the 9.2 msec target moving outward, the controller saturates. However, saturation is not exhibited when moving inward, and a control effort margin exists. The results suggest that better performance might be attainable, on average without saturation, by considering the directional dependence in the reference trajectory design. It was determined that the fastest outward trajectory the system could track without saturation was 10.7 msec (Fig. 3.2). Therefore, in order to meet the 9.2 msec average target, the system would be required to track an inward, 7.7 msec trajectory move. The simulation results show that the system was capable of tracking 8.95 msec inward without saturation (Fig. 3.3). The inward/outward move-time results in an average of 9.82 msec which exceeds the linear model target, but remains below the 10 msec specifications.

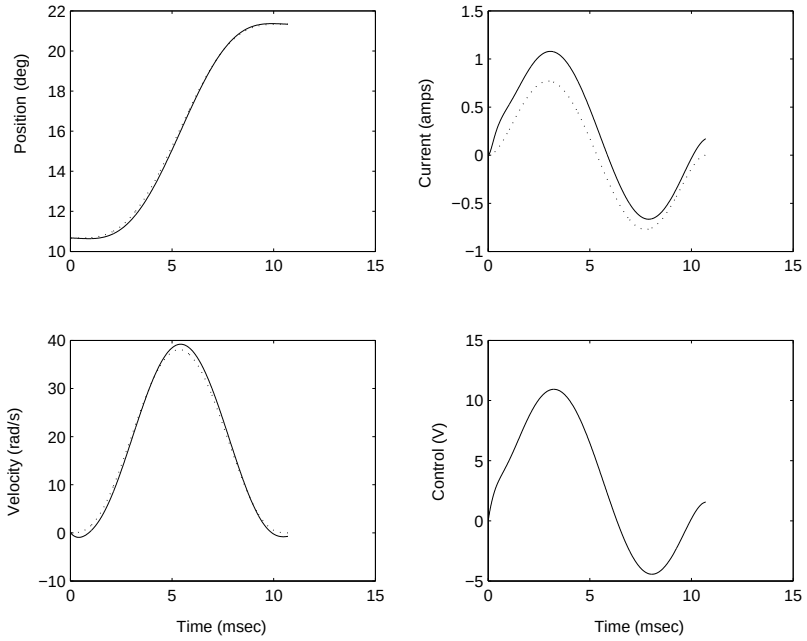

Figure 3.2: State feedback simulated outward move performance optimized for saturation in S_2; actual (solid), reference (dashed).

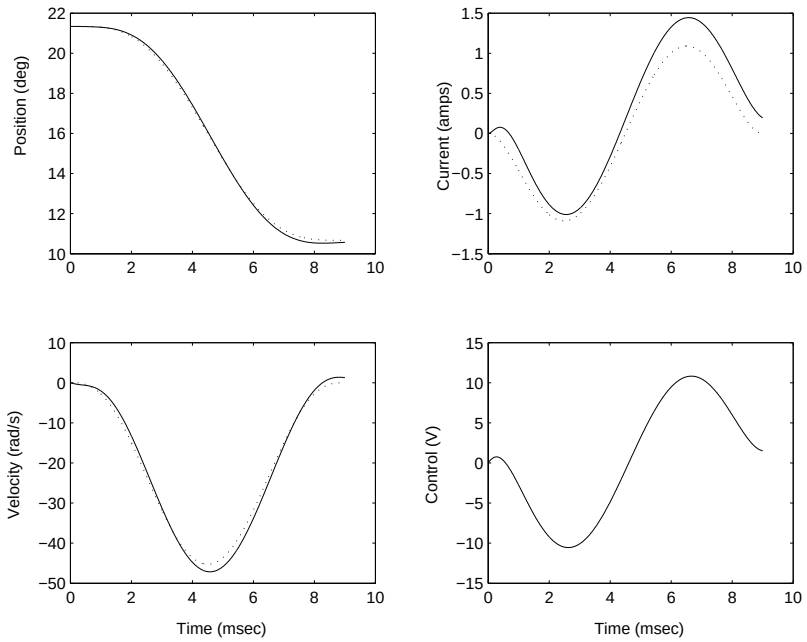

Figure 3.3: State feedback simulated inward move performance optimized for saturation in S_2; actual (solid), reference (dashed).

For the adaptive controller (3.27), the gains, α_k, were selected so that the error dynamics be five times the speed of the predicted third-stroke move. For the purpose of simulation, the nominal modeled bias was used and the estimated bias initial conditions were set to the minimum bias curve, ψ_{min}, of Figure 3.1. The trajectory tracking coefficients were chosen such that $\lambda = w_n$, $\alpha_2 = 2w_n$, and $\alpha_3 = w_n$ where $w_n = 3500$. Equation (3.25) results in $\alpha_1 = w_n^2$, and the parameter gain matrix, Γ, was determined iteratively as

$$\Gamma = \text{diag}\{2.5\times10^{-22},\ 10^{-20},\ 2\times10^{-16},\ 2.5\times10^{-14},\ 10^{-12},\ 3.3\times10^{-9},\ 2\times10^{-7}\} \quad (3.32)$$

Similar to the state-feedback case, the move-time performance was direction dependent. Therefore, the directional optimization used in the linear state-feedback controller case was also implemented here. The adaptive design was capable of tracking the optimal state-feedback trajectory with less control effort. More aggressive reference trajectories were generated and the controller was re-optimized. The tracking results for an inward and outward maneuver are shown in Figures 3.4 and 3.5, respectively. The performance combined for an average move-time of 9.5 msec which was 0.3 msec faster than state-feedback control. Also, the higher performance move was achieved with less overall error and comparable power consumption to that of state-feedback. The bias coefficient dynamics as a ratio of the estimate to the true value are shown in Figure 3.6 and 3.7 for an inward and outward maneuver, respectively. The adaptation gains are markedly large and no relevant adaptation is noticed in the higher-order bias polynomial coefficients indicating the higher-order terms could be neglected. Table 3.1 summarizes the simulated controller performance.

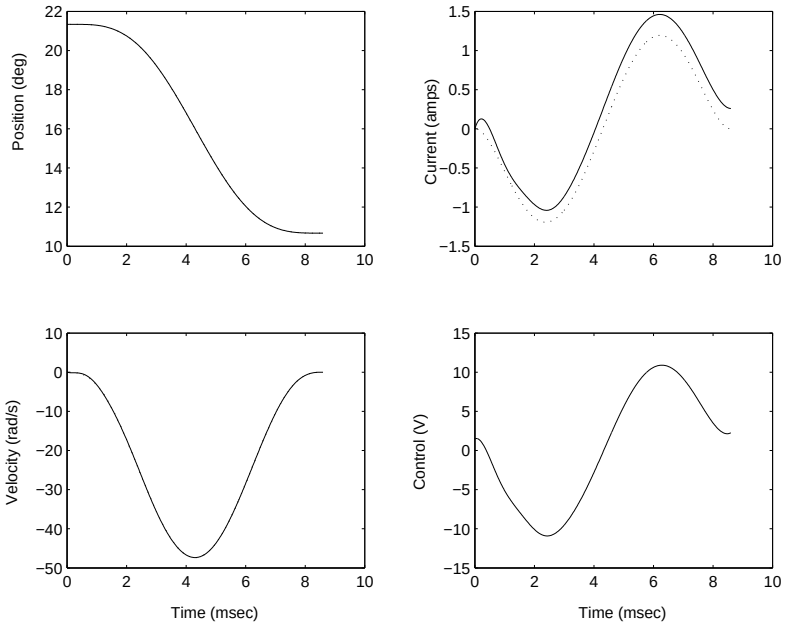

Figure 3.4: Adaptive control simulated inward move performance in S_2. Bias coefficients initially 7% lower than nominal; actual (solid), reference (dashed).

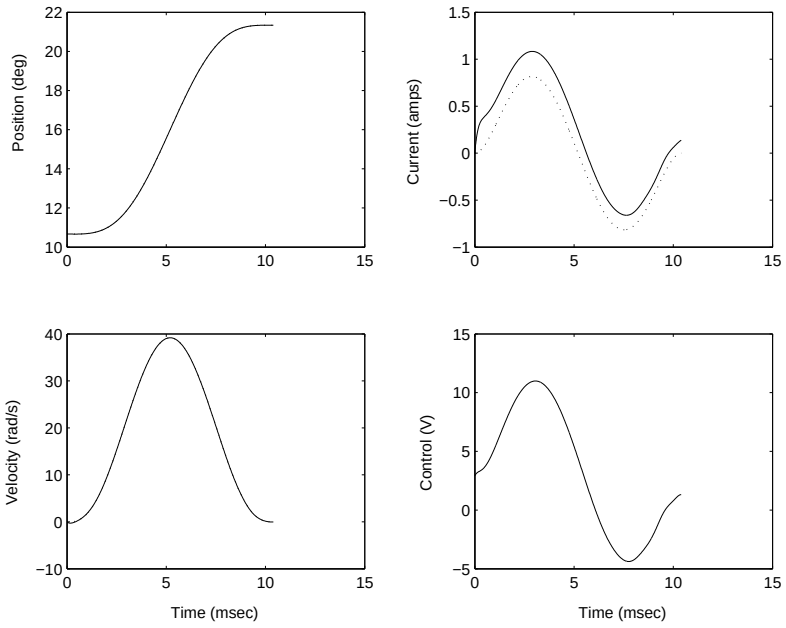

Figure 3.5: Adaptive control simulated outward move performance in S_2. Bias coefficients initially 7% lower than nominal; actual (solid), reference (dashed).

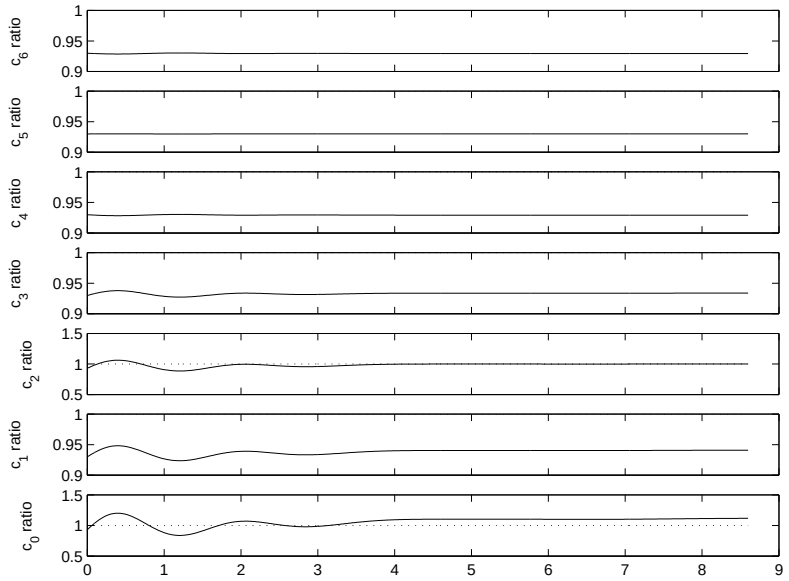

Figure 3.6: Adaptive control simulated bias coefficient ratio for an inward move in S_2. Bias coefficients initially 7% lower than nominal; actual (solid), reference (dashed).

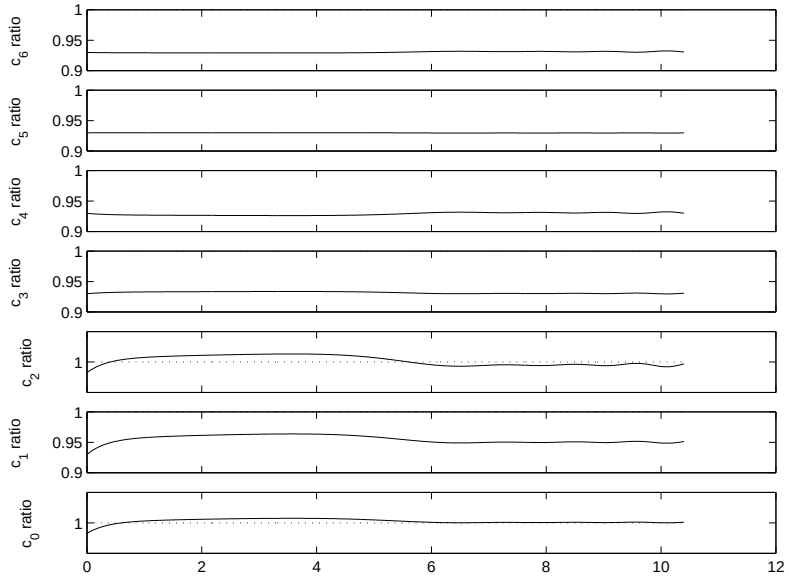

Figure 3.7: Adaptive control simulated bias coefficient ratio for an outward move in S_2. Bias coefficients initially 7% lower than nominal; actual (solid), reference (dashed).

Table 3.1: Simulated controller performance summary

Parameter	State Feedback		Adaptive	
	Outward	Inward	Outward	Inward
Move-time (msec)	10.7	8.95	10.4	8.6
Max Voltage (V)	10.935	10.935	10.92	10.99
Mean power (W)	6.2	3.8	6.07	4.02
Pos. error norm	0.059	0.057	4.15e-4	9.81e-4
Final pos. error (10^{-6}rad)	-81.7	-1780	-1.62	-5.20

3.3.2 Experimental Results

Figure 3.8 depicts the experimental setup which consisted of a disk drive containing the designed actuator and a laser doppler vibrometer (LDV) to provide position and velocity feedback. The laser was targeted on the side of the actuator arm approximately 23.24 mm from the pivot (Fig 3.9). Because the disks are highly reflective, removing them was necessary to minimize the laser scatter and maintain a satisfactory measurement signal. Also, the reflectivity range of the laser only allowed for a 5° move capability. Current feedback was achieved by measuring the voltage drop across a 0.2 Ω sense resistor. A proportional-integral controller was implemented to move and regulate the actuator 2° off the nominal shipping position. Experiments were conducted for the control designs developed in the previous sections. All tracking trajectories were designed for a 5°, 10 msec move. The control was chosen as in (3.6) and iterative tuning of the state-feedback gain vector resulted in $\mathcal{K} = [150,\ 1,\ 0.5]$. The control loop was executed at 20 kHz which is over 50 times the speed of the closed loop poles ensuring that the dynamics of the zero-order hold could be neglected. Data was collected for multiple groups of 100 seeks to ensure repeatability.

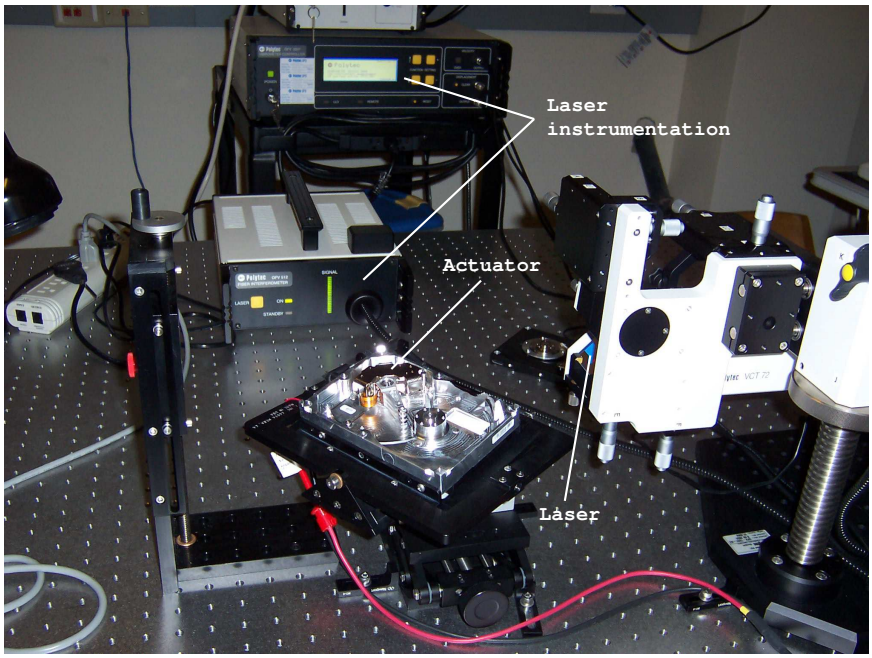

Figure 3.8: Experimental setup for full state feedback magnetic bias seek control

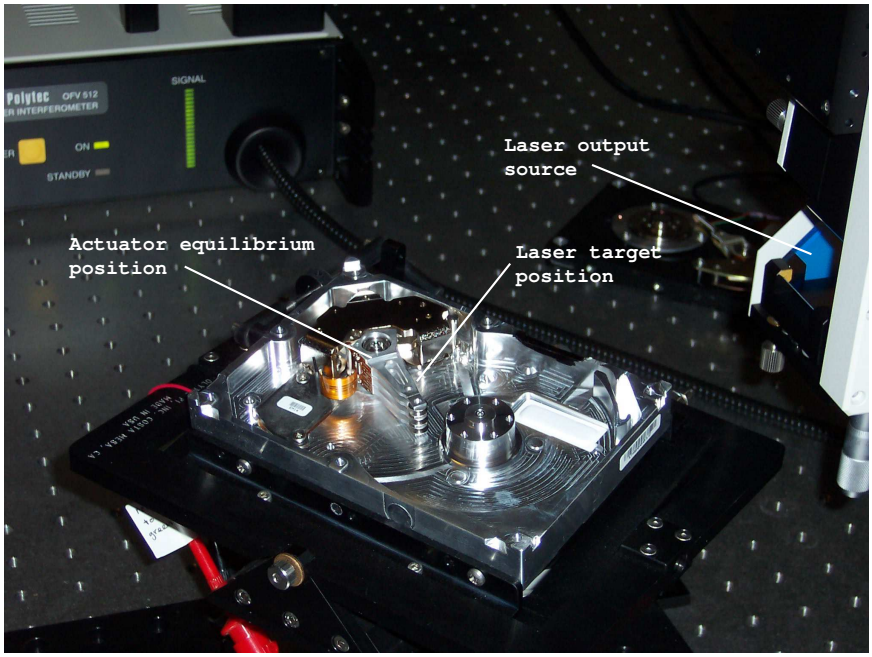

Figure 3.9: Experimental disk drive for full state feedback magnetic bias seek control

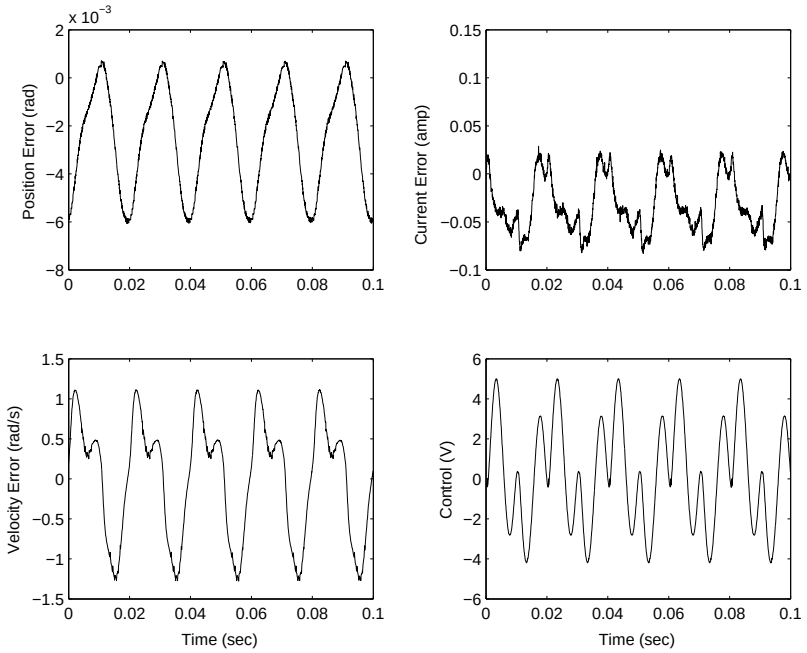

Figure 3.10: State feedback performance (10 seek sample)

Figure 3.10 shows the control and error performance of a representative sample of 10 seeks. For the adaptive control of (3.27) without projection ($\nabla_{\mathcal{P}}^{\top} = 0$), the initial conditions of the bias coefficient estimate were set at the lower bound (-7%). As in the state-feedback case the sample rate was set at 20 kHz and tuning showed the best trajectory tracking coefficients to be such that $\lambda = w_n$, $\alpha_2 = 2w_n$, and $\alpha_3 = w_n$ where $w_n = 400\pi$. Equation (3.25) results in $\alpha_1 = w_n^2$. The adaptation gain matrix was determined iteratively as

$$\Gamma = \text{diag}\{10^{-7},\ 10^{-9},\ 10^{-12},\ 10^{-13},\ 10^{-14},\ 10^{-15}\}. \tag{3.33}$$

It is noted that the gains are considerably larger compared to those used in simulation resulting from the magnetic bias estimated as a function of radian angle rather than degrees. Tracking error performance for a 10 seek sample is shown in Figure 3.11 along with the estimated bias coefficients in Figure 3.12. The position tracking error was significantly less than the state feedback case with comparable power consumption. It was noted that the coefficients would occasionally drift outside the expected

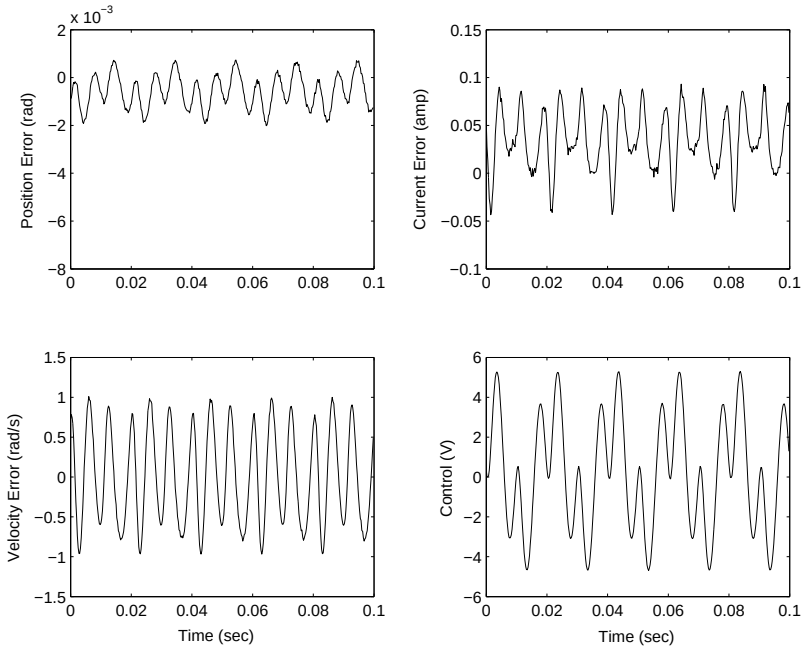

Figure 3.11: Adaptive controller performance (10 seek sample)

boundary limits during a given test run. To ensure that the coefficients remained close to the bounding limits, the gradient projection algorithm of (3.23) was implemented and included in the comparison. The results of the adaptive controller with projection are shown in Figure 3.13. Adaptive control with projection performance remained superior to the state-feedback case, but slightly worse than without projection. Adaptive control with projection gave a 12.4% and 1.6% increase in tracking error norm for position and velocity, respectively, when compared to adaptation without projection. The algorithm did effectively contain the coefficient trajectories as shown in Figure 3.14. Projection seemed to have the most influence on the higher order coefficients and was invoked 1262 times in a 2000 point, 10 seek sample run. The comparison results are summarized in Table 3.2.

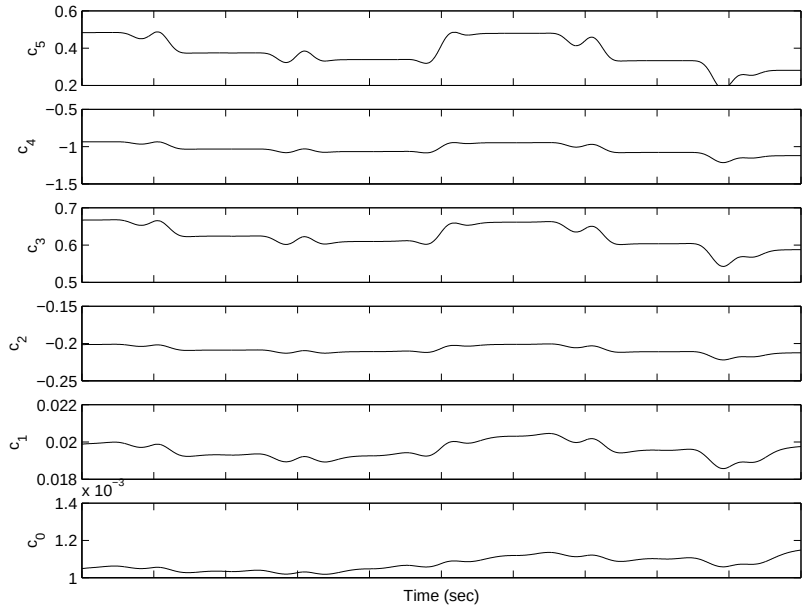

Figure 3.12: Estimated coefficient dynamics

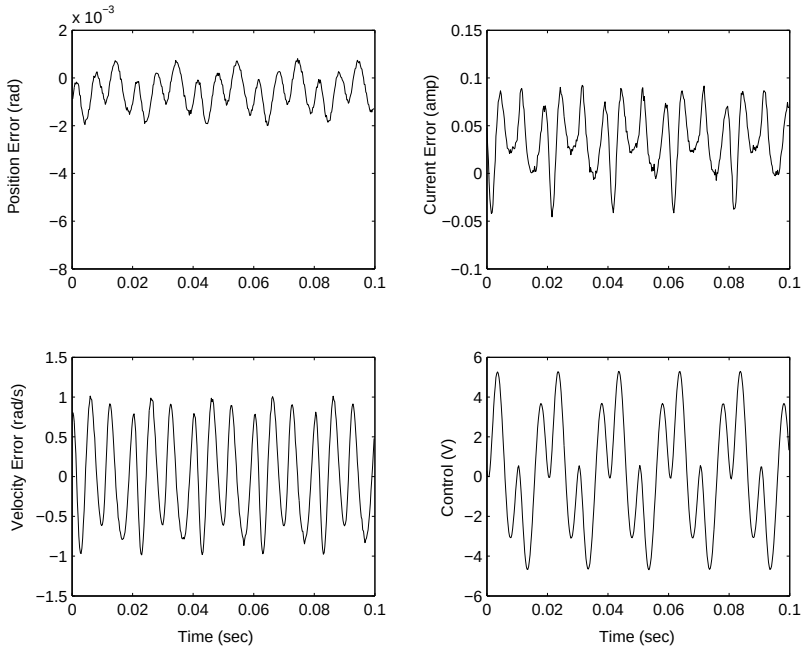

Figure 3.13: Adaptive controller performance with projection (10 seek sample)

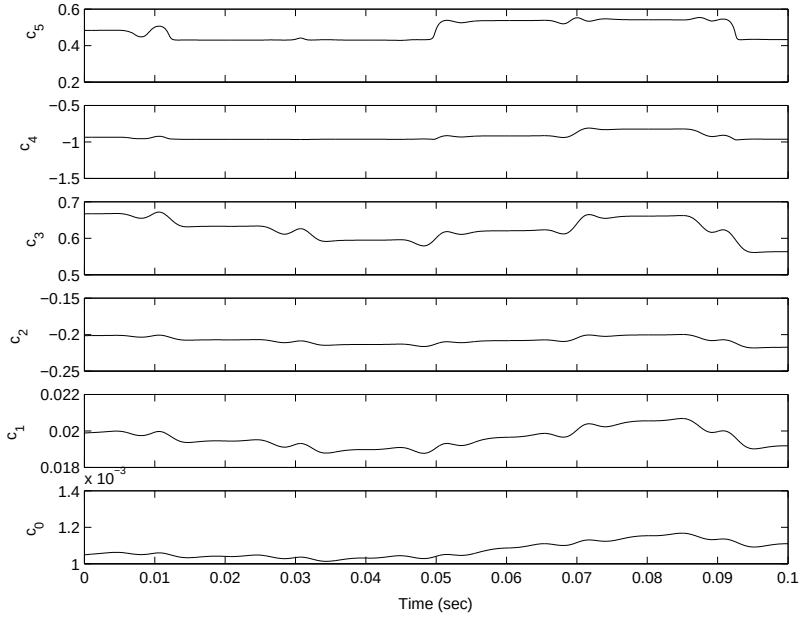

Figure 3.14: Estimated coefficient dynamics with projection

Table 3.2: Controller experimental performance summary

Parameter	State Feedback	Adaptive	Adaptive w/Proj
Pos. error L_2 norm	0.0661	0.0161	0.0181
Vel. error L_2 norm	14.45	11.94	12.13
Max Voltage (V)	5.078	5.534	5.292
Mean power (mW)	793	825	819

Table 3.3: Magnetic bias polynomial coefficients

Order	c_5	c_4	c_3	c_2	c_1	c_0
3	-	-	0.0294	-0.0191	0.0002	0.0014
4	-	-0.2145	0.2802	-0.1133	0.0124	0.0011
5	0.4518	-0.8749	0.6232	-0.1883	0.0186	0.0098

3.4 Modeling Accuracy and Sample Rate Effects

Accurate modeling of the magnetic bias results in increased model complexity. An increase in memory or processor capability might be required to perform the calculations necessary for the adaptive control law computation. It is suggested, however, that a sample rate increase could recover some of the performance lost by reducing the modeling accuracy. Therefore, a feasible solution would still be available for applications that are memory or processor limited. A comparative study was conducted to determine performance trade-offs between modeling accuracy of the magnetic bias and available sample rate resulting from computational requirements.

The bias was fit to polynomials of order three, four, and five. Performance comparisons were made using different estimates of the nonlinear bias function. Reducing the order of the polynomial estimate lowers the accuracy of the model and could increase the tracking error. However, the computation required for the control law is also reduced and, therefore, allows a sample rate increase and potentially improved tracking performance. The coefficients are given in Table 3.3. The control was chosen as (3.11) without projection and the initial conditions of the bias coefficient estimate were set at the lower bound (-7%). The sample rates were set at 30, 25, and 20 kHz for the bias estimate polynomials of 3, 4, and 5, respectively. Tuning showed the best

Table 3.4: Magnetic bias controller adaptation gains

Order	γ_5	γ_4	γ_3	γ_2	γ_1	γ_0
3	-	-	9.0e-11	8.0e-13	3.0e-13	3.0e-15
4	-	4.0e-9	8.0e-11	4.0e-13	9.0e-14	1.0e-15
5	1.0e-7	4.0e-9	1.0e-12	1.0e-13	1.0e-14	1.0e-15

trajectory tracking coefficients to be such that $w_n = 400\pi$ and

$$\lambda = w_n, \quad \alpha_1 = w_n^2, \quad \alpha_2 = 2w_n, \quad \alpha_3 = w_n.$$

The adaptation gains $\Gamma = \text{diag}\{\gamma_n, \cdots, \gamma_0\}$ where n is the bias polynomial estimate order, were determined iteratively and are given in Table 3.4. Reducing the order of the polynomial fit decreases the performance of the controller as expected. However, some or all of the performance could be recovered with a sample rate increase. In fact, a fourth order bias polynomial estimate outperformed the fifth-order estimate when the sample rate was increased by 5 kHz. The third-order estimate came close to achieving that of the fifth-order with a 10 kHz increase. Therefore, if the sampling resources are available, the complexity of the controller can be reduced while maintaining comparable performance. The comparison results are summarized in Table 3.5 and Figure 3.15.

Table 3.5: Bias modeling accuracy-sample rate study (L_2 norm)

Rate→	20 kHz		25 kHz		30 kHz	
Order↓	e_1	e_2	e_1	e_2	e_1	e_2
3	0.0517	17.11	0.0313	14.77	0.0182	11.21
4	0.0329	13.92	0.0153	10.34	-	-
5	0.0161	11.94	-	-	-	-

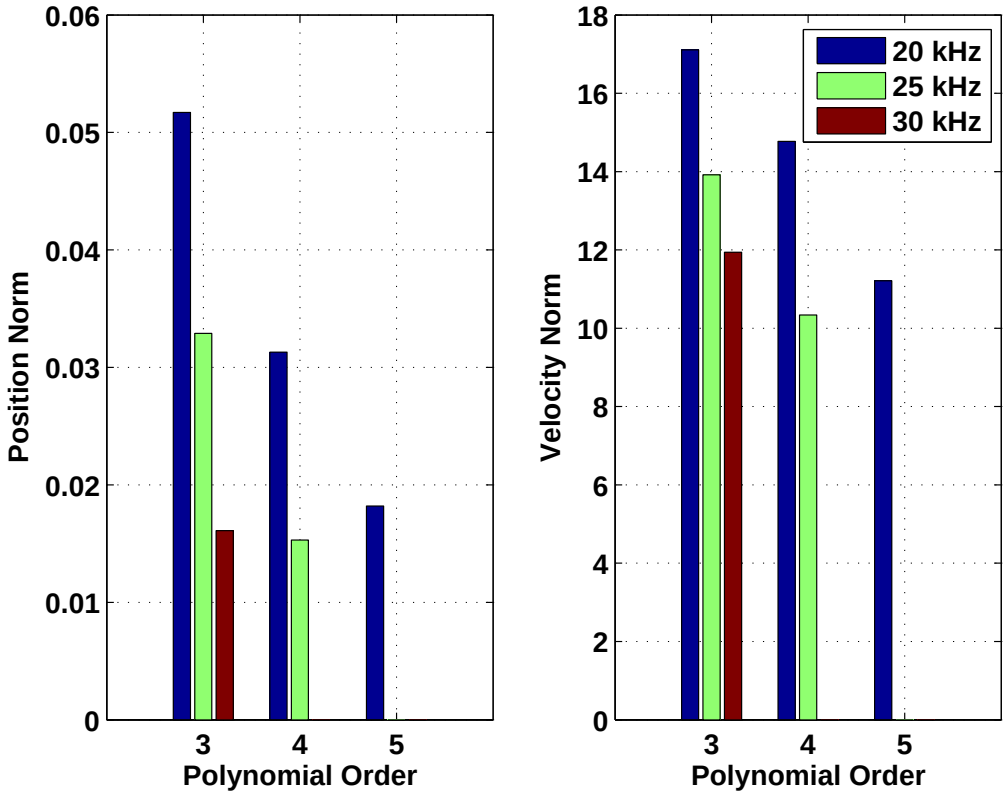

Figure 3.15: Bias modeling accuracy-sample rate study (L_2 norm)

3.5 Output Feedback Design

The previous controllers developed solutions based on the assumption that all states were readily available for feedback. However, direct velocity measurement is typically not available in production disk drives and, therefore, an output feedback solution is necessary. Although the position error signal (PES) would normally be used, this section considers a more restrictive solution based only on current measurement and relies on a nonlinear observer to supply the control law with the required state estimates.

3.5.1 Preliminaries

The dynamic model of (2.18) is modified to support current as the output ($y = i$), resulting in

$$\begin{aligned} \dot{x} &= Ax + Bu + B_\psi \psi(Hx) \\ y &= Cx \end{aligned} \tag{3.34}$$

$$A = \begin{bmatrix} 0 & 1 & 0 \\ 0 & 0 & \frac{K_t}{J} \\ 0 & -\frac{K_t}{L} & -\frac{R}{L} \end{bmatrix}, \quad B = \begin{bmatrix} 0 \\ 0 \\ \frac{1}{L} \end{bmatrix}, \quad B_\psi = \begin{bmatrix} 0 \\ -\frac{1}{J} \\ 0 \end{bmatrix}$$

$$C = [0\ 0\ 1] \quad H = [1\ 0\ 0]$$

The controller developed in the next section requires observability of the linear component. It can be readily determined that the system (3.34) does not satisfy this requirement. The issue can be overcome by redefining the nonlinearity as

$$\phi(x_1) = \mu_1[\psi(x_1) - c_1 x_1] \tag{3.35}$$

and recruiting the linear term, $\mu_1 c_1 x_1$ into A. Equation (3.34) now becomes

$$\begin{aligned} \dot{x} &= A_\phi x + Bu + B_\phi \phi(Hx) \\ y &= Cx \end{aligned} \tag{3.36}$$

where

$$A_\phi = \begin{bmatrix} 0 & 1 & 0 \\ -\mu_1 c_1 & 0 & \mu_0 \\ 0 & -\mu_2 & -\mu_3 \end{bmatrix}, \quad B_\phi = \begin{bmatrix} 0 \\ -1 \\ 0 \end{bmatrix}$$

and

$$\mu_0 = \frac{K_t}{J},\ \mu_1 = \frac{1}{J},\ \mu_2 = \frac{K_t}{L},\ \mu_3 = \frac{R}{L}$$

The output feedback tracking controller is developed with the following assumptions:

Assumption 3.1 *The nonlinearity, $\phi(Hx)$, is Lipschitz with respect to the state,*

$$\|\phi(Hx_a) - \phi(Hx_b)\| \leq \gamma \|Hx_a - Hx_b\| \tag{3.37}$$

$$\forall\, x_a, x_b \in X \quad X := \{x \in \mathbb{R}^3 | x_1 \in \Theta\}$$

where γ is the Lipschitz constant and Θ is the set of all possible actuator sweep angles.

Assumption 3.2 *The pair (A_ϕ, B) is controllable.*

Assumption 3.3 *The pair (A_ϕ, C) is observable.*

Remark 3.1 *Assumption 3.1 will always be satisfied for a polynomial representation* (3.35) *when the polynomial order $k \geq 0$. Assumption 3.2 is always satisfied for the generic disk drive dynamics described by* (3.36) *with $K_t \neq 0$. Assumption 3.3 will be satisfied for all $c_1 \neq 0$.*

The following definition is necessary prior to developing the output feedback control law.

Definition 3.1 [29] *The distance between an observable pair (M, N_o) and the set of pairs with an unobservable, purely imaginary mode is*

$$\delta(M, N_o) = \min_{\omega \in \mathbb{R}} \sigma_{\min} \begin{pmatrix} j\omega I - M \\ N_o \end{pmatrix}$$

where $j = \sqrt{-1}$, I is the identity matrix, and $\sigma_{\min}(\cdot)$ is the minimum singular value of the matrix $(\cdot)$.

Similarly, $\delta(M^\top, N_c^\top)$ is the distance between a controllable pair, (M, N_c), and the set of pairs with an uncontrollable, purely imaginary mode.

3.5.2 Full State Feedback Controller Design

It is desired the system track a predetermined trajectory, x_r, based on the reference model

$$\dot{x}_r = A_\phi x_r + B_\phi \phi(H x_r) \tag{3.38}$$

Consider the control law

$$u = u_{ff} + u_s + u_{fb} \tag{3.39}$$

where

$$u_{ff} = L(\dot{x}_{3r} + \mu_3 x_{3r} + \mu_2 x_{2r}) \tag{3.40}$$

is the feed-forward term, u_s and u_{fb} are the linear stabilization and feedback terms, respectively to be determined. Substituting (3.39) into (3.36) and subtracting (3.38) gives the tracking error dynamics

$$\dot{e} = A_\phi e + B_c(u_s + u_{fb}) + B_\phi(\phi(Hx) - \phi(Hx_r)) \tag{3.41}$$

where $e = x - x_r$ and $B_c = [0\ 0\ 1]^\top$. Now, if A_ϕ is not Hurwitz it can be stabilized using

$$u_s = -\mathcal{K}_s e \tag{3.42}$$

resulting in

$$\dot{e} = A_s e + B_c u_{fb} - B_\phi[\phi(Hx) - \phi(Hx_r)] \tag{3.43}$$

where $\mathcal{K}_s$ is the stablizing gain vector and $A_s = A_\phi - B_c\mathcal{K}_s$ is Hurwitz. Choose

$$u_{fb} = -\frac{\mathcal{K}_c}{\|B_c\|^2} e \tag{3.44}$$

where $\mathcal{K}_c$ is the feedback gain vector,

$$A_c = A_s - \frac{B_c\mathcal{K}_c}{\|B_c\|^2}, \tag{3.45}$$

and consider the Lyapunov function

$$V_c(e) = e^\top P_c e, \quad P_c = P_c^\top,\ P_c > 0 \tag{3.46}$$

Differentiating V_c along the trajectory of (3.43) results in

$$\begin{aligned}\dot{V}_c(e) &= e^\top (A_c^\top P_c + P_c A_c)e + 2e^\top P_c B_\phi[\phi(Hx) - \phi(Hx_r)] \\ &\leq e^\top (A_c^\top P_c + P_c A_c)e + 2\gamma\|B_\phi\|\,\|H\|\,\|P_c e\|\,\|e\| \end{aligned} \tag{3.47}$$

If $\sqrt{\beta} = \|B_\phi\|\,\|H\|$ then

$$e^\top (P_c - \gamma\sqrt{\beta} I)^2 e \geq 0. \tag{3.48}$$

Expanding the left side of (3.48) results in

$$e^\top (P_c P_c + \gamma^2 \beta I)e \geq 2\gamma\sqrt{\beta}\|P_c e\|\,\|e\|.$$

It follows that

$$\dot{V}_c(e) \leq e^\top (A_c^\top P_c + P_c A_c + P_c P_c + \gamma^2\beta I)e. \tag{3.49}$$

So for any $\eta_c > 0$, $\dot{V}_c(e) \leq -\eta_c\|e\|^2$ if

$$A_c^\top P_c + P_c A_c + P_c P_c + \gamma^2\beta I = -\eta_c I \tag{3.50}$$

The choice of the control gain vector

$$\mathcal{K}_c = \frac{1}{2} B_c^\top P_c \tag{3.51}$$

results in

$$A_s^\top P_c + P_c A_s + P_c \left(I - \frac{B_c B_c^\top}{\|B_c\|^2} \right) P_c + (\gamma^2\beta + \eta_c) I = 0 \tag{3.52}$$

Since A_s is Hurwitz, $I - \frac{B_c B_c^\top}{\|B_c\|^2} \geq 0$, and $(\gamma^2\beta + \eta_c) > 0$, a solution, P_c, to the ARE (3.52) exists if the associated Hamiltonian matrix

$$\mathbb{H}_c = \begin{bmatrix} A_s & I - \frac{B_c B_c^\top}{\|B_c\|^2} \\ -(\gamma^2\beta + \eta_c) I & -A_s^\top \end{bmatrix} \tag{3.53}$$

is hyperbolic.

Lemma 3.1 *$\mathbb{H}_c$ is hyperbolic if*

$$\sqrt{\gamma^2\beta+\eta_c} < \delta\left(A_s^\top,\, \sqrt{\gamma^2\beta+\eta_c}\,\frac{B_c^\top}{\|B_c\|}\right), \quad \sqrt{\beta} = \|B_\phi\|\,\|H\| \tag{3.54}$$

Proof. The eigenvalues of $\mathbb{H}_c$ may be obtained by considering

$$\begin{aligned}\det(sI-\mathbb{H}_c) &= \det\begin{bmatrix} sI-A_s & -\left(I-\frac{B_cB_c^\top}{\|B_c\|^2}\right) \\ (\gamma^2\beta+\eta_c)I & sI+A_s^\top \end{bmatrix} \\ &= (-1)^n\det\begin{bmatrix} (\gamma^2\beta+\eta_c)I & sI+A_s^\top \\ sI-A_s & -\left(I-\frac{B_cB_c^\top}{\|B_c\|^2}\right) \end{bmatrix} \end{aligned} \tag{3.55}$$

Since $(\gamma^2\beta+\eta_c)>0$, the determinant of the block matrix (3.55) can be written as

$$\begin{aligned}\det(sI-\mathbb{H}_c) &= (-1)^n\,(\gamma^2\beta+\eta_c)\det\left[\left(-I+\frac{B_cB_c^\top}{\|B_c\|^2}\right)-(sI-A_s)(\gamma^2\beta+\eta_c)^{-1}(sI+A_s^\top)\right] \\ &= (-1)^n\det\left[(\gamma^2\beta+\eta_c)\left(-I+\frac{B_cB_c^\top}{\|B_c\|^2}\right)-(sI-A_s)(sI+A_s^\top)\right]\end{aligned}$$

Letting $s=-j\omega$ and noting that

$$-(-j\omega I-A_s)(-j\omega I+A_s^\top) = (-j\omega I-A_s)(j\omega I-A_s^\top)$$

it follows that $\pm j\omega$ is an eigenvalue of $\mathbb{H}_c$ if the matrix

$$\begin{aligned}\Lambda(-j\omega) &= \left[(-j\omega I-A_s)(j\omega I-A_s^\top)+(\gamma^2\beta+\eta_c)\frac{B_cB_c^\top}{\|B_c\|^2}-(\gamma^2\beta+\eta_c)I\right] \\ &= \begin{bmatrix} j\omega I-A_s^\top \\ \frac{\sqrt{\gamma^2\beta+\eta_c}\,B_c^\top}{\|B_c\|}\end{bmatrix}^*\begin{bmatrix} j\omega I-A_s^\top \\ \frac{\sqrt{\gamma^2\beta+\eta_c}\,B_c^\top}{\|B_c\|}\end{bmatrix}-(\gamma^2\beta+\eta_c)I\end{aligned}$$

is singular. Noting from Definition 3.1 that

$$\delta^2\left(A_s^\top,\, \sqrt{\gamma^2\beta+\eta_c}\frac{B_c^\top}{\|B_c\|}\right) \le \begin{bmatrix} j\omega I-A_s^\top \\ \frac{\sqrt{\gamma^2\beta+\eta_c}\,B_c^\top}{\|B_c\|}\end{bmatrix}^*\begin{bmatrix} j\omega I-A_s^\top \\ \frac{\sqrt{\gamma^2\beta+\eta_c}\,B_c^\top}{\|B_c\|}\end{bmatrix}$$

the eigenvalues of $\mathbb{H}$ will always have nonzero real parts if

$$\delta^2\left(A_s^\top,\, \sqrt{\gamma^2\beta+\eta_c}\,\frac{B_c^\top}{\|B_c\|}\right)-(\gamma^2\beta+\eta_c)>0 \quad \text{or}$$

$$\sqrt{\gamma^2\beta+\eta_c} < \delta\left(A_s^\top,\, \sqrt{\gamma^2\beta+\eta_c}\,\frac{B_c^\top}{\|B_c\|}\right), \quad \sqrt{\beta} = \|B_\phi\|\,\|H\|$$

■

Combining equations (3.40), (3.42), and (3.44) gives the tracking control law

$$u = L(\dot{x}_{3r} + \mu_3 x_{3r} + \mu_2 x_{2r}) - \left(\mathcal{K}_s + \frac{\mathcal{K}_c}{\|B_c\|^2}\right) e \tag{3.56}$$

For the nonlinear disk drive dynamics given by (3.34), the tracking control law (3.56) renders the error dynamics (3.41) with Assumptions 3.1 and 3.2, exponentially stable if (3.54) is satisfied.

3.5.3 Observer Design

Consider the observer

$$\dot{\hat{x}} = A_\phi \hat{x} + Bu - B_\phi \phi(H\hat{x}) + \left(\mathcal{L}_s + \frac{\gamma^2 + \varepsilon_o}{\|C\|^2}\mathcal{L}_{fb}\right)(y - C\hat{x}) \tag{3.57}$$

where $\mathcal{L}_s, \mathcal{L}_{fb} \in \mathbb{R}^3$ are observer gains and $\varepsilon_o \geq -\gamma^2$. Defining the observer error as $\tilde{x} = x - \hat{x}$ results in dynamics

$$\dot{\tilde{x}} = \left[A_\phi - \left(\mathcal{L}_s + \frac{\gamma^2 + \varepsilon_o}{\|C\|^2}\mathcal{L}_{fb}\right) C\right] \tilde{x} + B_\phi[\phi(Hx) - \phi(H\hat{x})] \tag{3.58}$$

Using the Lyapunov function

$$V_o(\tilde{x}) = \tilde{x}^\top P_o \tilde{x}, \quad P_o = P_o^\top,\ P_o > 0 \tag{3.59}$$

and differentiating V_o along the trajectory of (3.58) gives results similar to (3.47)

$$\begin{aligned}\dot{V}_o(\tilde{x}) = \tilde{x}^\top &\left[A_o^\top P_o + P_o A_o - \frac{\gamma^2 + \varepsilon_o}{\|C\|^2}(C^\top \mathcal{L}_{fb}^\top P_o + P_o \mathcal{L}_{fb} C)\right] \tilde{x} \\ &+ 2\tilde{x}^\top P_o B_\phi[\phi(Hx) - \phi(H\hat{x})] \\ \leq \tilde{x}^\top &\left[A_o^\top P_o + P_o A_o - \frac{\gamma^2 + \varepsilon_o}{\|C\|^2}(C^\top \mathcal{L}_{fb}^\top P_o + P_o \mathcal{L}_{fb} C) + P_o P_o + \gamma^2 \beta I\right] \tilde{x}\end{aligned} \tag{3.60}$$

where $A_o = A_\phi - \mathcal{L}_s C$ is Hurwitz. If the observer feedback gain vector is chosen as

$$\mathcal{L}_{fb} = \frac{1}{2} P_o^{-1} C^\top \tag{3.61}$$

then for any $\eta_o > 0$, $\dot{V}_o(e) \leq -\eta_o \|\tilde{x}\|^2$ if

$$A_o^\top P_o + P_o A_o - \frac{\gamma^2 + \varepsilon_o}{\|C\|^2} C^\top C + P_o P_o + (\gamma^2 \beta + \eta_o) I = 0 \tag{3.62}$$

Following the preceding results, a solution, P_o, to the ARE (3.62) exists if the associated Hamiltonian matrix

$$\mathbb{H}_o = \begin{bmatrix} A_o & I \\ -(\gamma^2 \beta + \eta_o) I + \frac{\gamma^2 + \varepsilon_o}{\|C\|^2} C^\top C & -A_o^\top \end{bmatrix} \tag{3.63}$$

is hyperbolic. Using a similar analysis from Lemma 3.1, results in the analogous sufficient condition

$$\sqrt{\gamma^2 \beta + \eta_o} < \delta \left(A_o, \frac{\sqrt{\gamma^2 + \varepsilon_o}}{\|C\|} C \right), \quad \sqrt{\beta} = \|B_\phi\| \, \|H\| \tag{3.64}$$

3.5.4 Output Feedback

Theorem 3.2 *Let $X := \{x \in \mathbb{R}^3 | x_1 \in \Theta\}$ where Θ is the set of all possible actuator sweep angles and $\phi(Hx)$ is Lipschitz according to* (3.37)*. The output feedback tracking control law*

$$u_{of} = L(\dot{x}_{3r} + \mu_3 x_{3r} + \mu_2 x_{2r}) - \mathcal{K}_c \hat{e} \tag{3.65}$$

with $\hat{e} = \hat{x} - x_r$ renders the tracking error dynamics (3.41) *and observer error dynamics* (3.58) *exponentially stable for all $x \in X$.*

Proof. Substituting (3.65) into (3.36) gives

$$\dot{e} = A_c e + B_c K_c \tilde{x} + \phi(Hx) - \phi(Hx_r) \tag{3.66}$$

Now, recall $V_c(e) = e^\top P_c e$, so

$$\dot{V}_c(e) \leq -\eta_c \|e\|^2 + 2 e^\top P_c B_c K_c \tilde{x} \tag{3.67}$$

$$\leq -\eta_c \|e\|^2 + 2 P_c B_c K_c \|e\| \, \|\tilde{x}\| \tag{3.68}$$

$$\leq -\eta_c \|e\|^2 + \xi_c \|e\| \, \|\tilde{x}\| \tag{3.69}$$

where $\xi_c = 2\|P_c B_c K_c\|$. Consider

$$W(e, \tilde{x}) = \xi V_c(e) + V_o(\tilde{x}) \tag{3.70}$$

where $\xi = \frac{\eta_c \eta_o}{\xi_c^2}$. Taking the time derivative of (3.70) yields

$$\dot{W}(e, \tilde{x}) \leq -\frac{\eta_c^2 \eta_o}{\xi_c^2}\|e\|^2 + \frac{\eta_c \eta_o}{\xi_c}\|e\|\,\|\tilde{x}\| - \eta_o\|\tilde{x}\|^2 \tag{3.71}$$

$$\leq -\frac{1}{2}\left(\frac{\eta_c^2 \eta_o}{\xi_c^2}\|e\|^2 + \eta_o\|\tilde{x}\|^2\right) \tag{3.72}$$

where equation (3.72) follows from (3.71) by completing the square and noting that

$$\left(\frac{1}{\sqrt{2}}\frac{\eta_c\sqrt{\eta_o}}{\xi_c}\|e\| - \frac{1}{\sqrt{2}}\sqrt{\eta_o}\|\tilde{x}\|\right)^2 \geq 0 \tag{3.73}$$

Therefore, $W(e, \tilde{x})$ is a Lyapunov function and $e, \tilde{x} \to 0$ exponentially as $t \to \infty$. ■

Remark 3.2 *The number δ is realization dependent. Therefore, a coordinate transformation can be used to reduce the value of γ and increase δ [30]. When using standard SI units, the actuator inertia is typically very small relative to K_t, R, and L, therefore the inertia can be lumped into the Lipschitz nonlinearity where a similarity transformation can be used to reduce the constant.*

3.5.5 Experimental Results

The experimental disk drive possessed similar specifications to that used in Section 3.3.2. Measurement of the actuator physical parameters resulted in 48.06 g-cm^2, 62.4 N-mm/amp, 9.22 Ω, and 1.11 mH for the inertia, torque constant, coil resistance, and coil inductance, respectively. The bias polynomial with coefficients were determined as

$$c_5 = 0.4518;\ c_4 = -0.8749;\ c_3 = 0.6232;\ c_2 = -0.1883;\ c_1 = 0.0186;\ c_0 = 0.0098$$

A reference trajectory was generated based on the method of Section 3.1. To ensure that the bias was significant relative to available torque, the maximum seek current

was limited to 0.5 amps and reflected in the reference trajectory. This results in a maximum bias that is 5% of the current limited torque capability of the actuator. Because only a finite number of drives were available for testing, the limitation also protected the hardware from damage while tuning gains. Smooth trajectories were generated based on the 0.5 amp saturation limit for seek lengths of 0.0873 rad (5°), 0.1745 rad (10°), and 0.3491 rad (20°). The resulting seek times were 9.3 msec, 13.0 msec, and 18.7 msec, respectively. The seek time is actually conservative compared to the capability of the actuator in order to provide the current limitation. This limitation can be relaxed in a production setting and trajectories can be designed for current corresponding to the typical 11 V saturation limit. The Lipschitz constant for ϕ was calculated as $\gamma = 5496,\ \forall\, x \in X$. Because $c_1 > 0$, A_ϕ in (3.36) is stable. Therefore, the stabilization gains $\mathcal{K}_s, \mathcal{L}_s$ are not necessary. However, it was desired to modify the tracking performance of the linear system. The poles of the tracking control law were placed at $[-80\ -76\ -7860]$ resulting in a stabilization gain vector of

$$\mathcal{K}_s = [1078.84\ 19.11\ 7.30]$$

A performance gain was also desired for the observer and placement of the observer stabilization poles resulted in

$$\mathcal{L}_s^\top = [-36.55\ -3815.6\ 1181.3]$$

A similarity transformation $e = T_c e'$ as discussed in [30] where

$$\|T_c^{-1}\phi(HT_c x_a) - T_c^{-1}\phi(HT_c x_b)\| \leq \gamma' \|x_a - x_b\| \tag{3.74}$$

can be used to reduce the Lipschitz constant and increase the value of δ. Transformations were chosen as

$$T_c = \text{diag}\{1\ 10^4\ 200\}, \quad e = T_c e'$$
$$T_o = \text{diag}\{1\ 10^4\ 1\}, \qquad \tilde{x} = T_o \tilde{x}'$$

resulting in the tracking controller and observer Lipschitz constants $\gamma_c' = 0.5505$ and $\gamma_o' = 0.5496$, respectively.

To get an initial estimate of appropriate controller and observer gains and ensure convergence using only current feedback, simulations were conducted for the three designated seek lengths. A satisfactory solution was determined through iteration with state feedback controller gain vector

$$\mathcal{K}_{sim} = \mathcal{K}_s + \frac{\mathcal{K}_c}{\|B_c\|^2} = [1244.63\ 20.12\ 9.33]$$

and $\eta_c = 0.01$ resulting in $\delta = 0.596$. An initial observer gain vector

$$\mathcal{L}_{sim}^{\top} = \left(\mathcal{L}_s + \frac{\gamma^2 + \varepsilon_o}{\|C\|^2}\mathcal{L}_{fb}\right)^{\top} = [-37.20\ -3848.42\ 1243.02]$$

was determined with $\eta_o = 10^{-4}$ and $\varepsilon_o = -0.3$ resulting in $\delta = 0.5498$. Therefore, both conditions (3.54) and (3.64) were satisfied with the corresponding gain vectors. Simulation results for a 0.1745 rad seek are depicted in Figure 3.16.

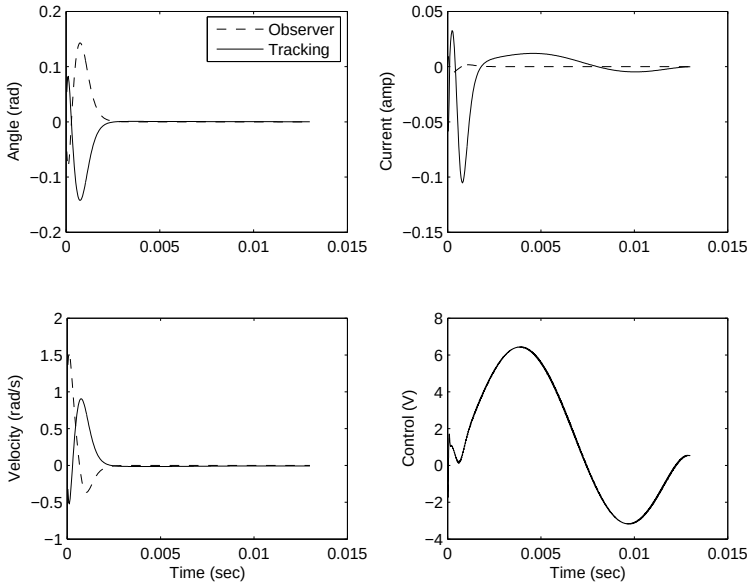

Figure 3.16: Simulation error results (0.1745 rad)

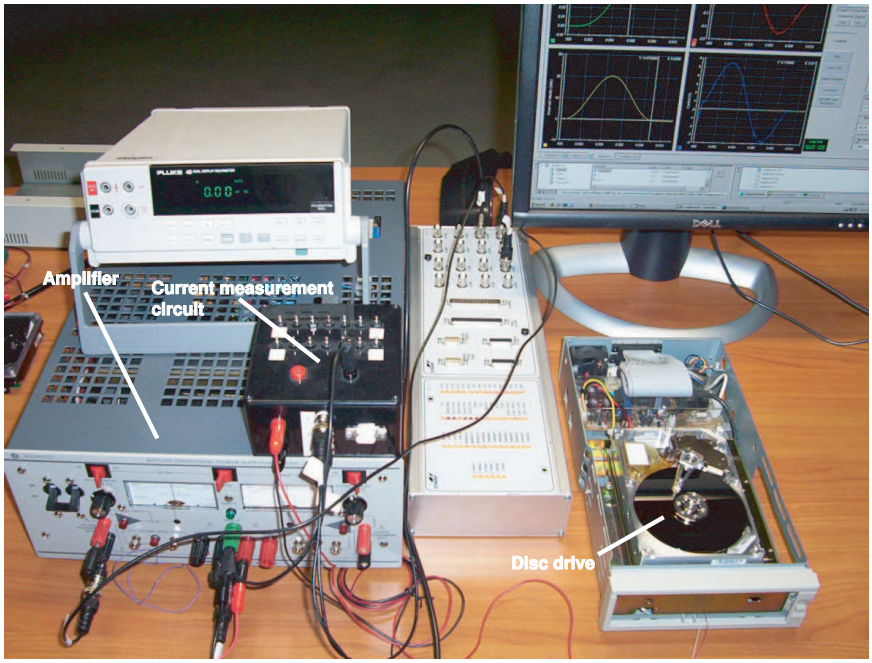

Figure 3.17: Experimental setup

Loading the states with initial conditions $[x_1\ x_2\ x_3] = [0.01\ 1\ 0.1]$, convergence is noted for both the tracking and observer errors while the controller output limits the current within the required bounds. The gains $\mathcal{K}_{sim}$ and $\mathcal{L}_{sim}$ were used as preliminary gains for experimental evaluation of the output feedback controller. Within the experimental platform, the actuator was driven by a digital signal processor (DSP) board with analog I/O peripherals. Voltage output from the DSP board was injected through a bipolar amplifier and into the disk drive actuator. Current feedback was achieved by recording the voltage across a 0.2 Ω sense resistor connected in series with the actuator coil. The experimental setup is shown in Figure 3.17. The initial gains from simulation analysis resulted in performance that exceeded the 0.5 amp limitation. The controller and observer gains were retuned to produce the desired performance. The final tracking control gain vector of

$$\mathcal{K}_{cx} = [962.21\ 12.19\ 9.28] \tag{3.75}$$

was checked to ensure

$$A_{cx}^{\top}P_{cx} + P_{cx}A_{cx} + P_{cx}P_{cx} + (\gamma^2\beta^2 + \eta_c)I = 0 \tag{3.76}$$

was satisfied where $A_{cx} = A - B_c\mathcal{K}_{cx}$ and

$$P_{cx} = \begin{bmatrix} 28.4028 & -0.0677 & -0.1418 \\ -0.0677 & 0.0071 & 0.0137 \\ -0.1418 & 0.0137 & 0.0269 \end{bmatrix}$$

Similarly, the observer gains were tuned to

$$\mathcal{L}_{ox}^{\top} = [-104.25 \ -2559.17 \ 1642.60] \tag{3.77}$$

where $A_{ox} = A - L_{ox}C$ and

$$A_{ox}^{\top}P_{ox} + P_{ox}A_{ox} + P_{ox}P_{ox} + (\gamma^2\beta^2 + \eta_o)I = 0 \tag{3.78}$$

is satisfied resulting in

$$P_{ox} = \begin{bmatrix} 2.7747 & -0.0009 & -0.0327 \\ -0.0009 & 0.0012 & 0.0023 \\ -0.0327 & 0.0023 & 0.0048 \end{bmatrix}$$

Figures 3.18 and 3.19 show the results of the output feedback tracking controller implemented at 25 kHz for 0.0873 rad and 0.1745 rad seeks, respectively. The observer was loaded with initial conditions $[\hat{x}_1 \ \hat{x}_2 \ \hat{x}_3] = [0 \ 0 \ 0]$. The controller immediately compensates for bias error with some overshoot indicating the gains could be relaxed further for improved shaping of the initial transient response. The tracking errors are shown in Figures 3.20 and 3.21 along with corresponding norms given in Table 3.6. Position and velocity error increased with seek length while current error decreased. Also, the current observer exhibited improved performance as the seek length increased. The observer error current norms were 0.3795, 0.3469, and 0.2958, for seek lengths 0.0873, 0.1745, and 0.3491 rad, respectively. An additional trial of the 0.0873

rad seek is presented (Fig. 3.22) with the observer initialized at $[\hat{x}_1\ \hat{x}_2\ \hat{x}_3] = [0\ 0\ 0.1]^\top$ to demonstrate convergence.

Remark 3.3 *The transformation T_c in (3.74) modifies the Lipschitz condition. The nonlinearity now becomes a function of $t_{11}x_1$ where $t_{11} = T_c(1,1)$ is the first diagonal element of T_c. Therefore, choosing $t_{11} = 1$ preserves the scope of the Lipschitz constant to remain in the set Θ.*

Table 3.6: Error norms

Length	0.0873 rad	0.1745 rad	0.3491 rad
Position	0.0113	0.0166	0.0311
Velocity	2.9831	3.6380	4.6177
Current	0.5254	0.5186	0.3654
Observer	0.3795	0.3469	0.2958

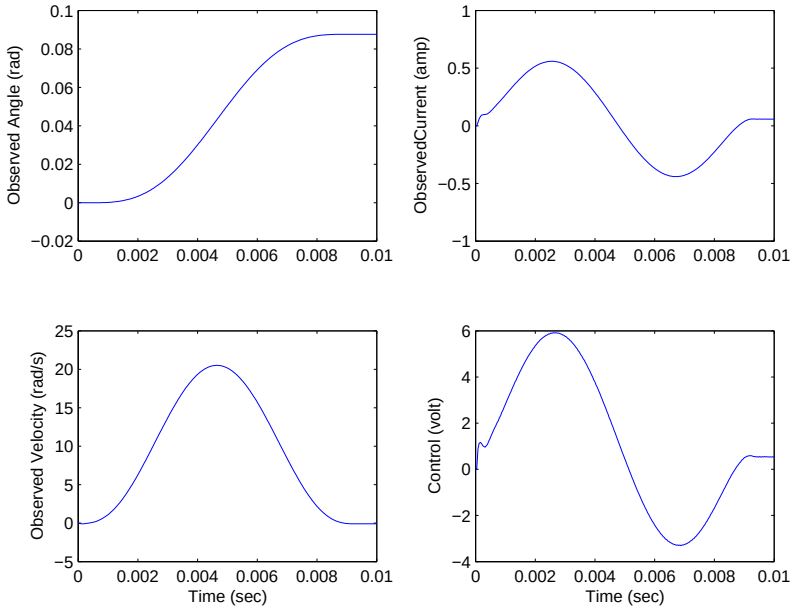

Figure 3.18: Experimental seek results (0.0873 rad)

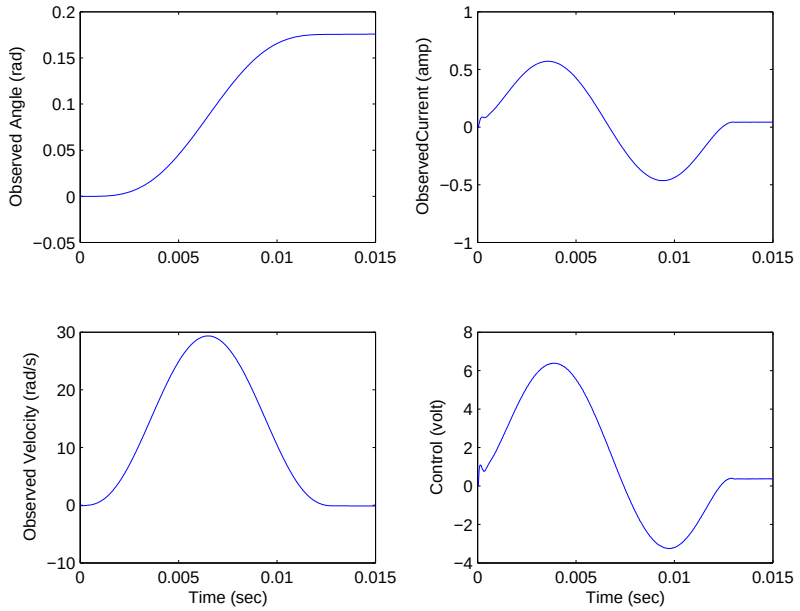

Figure 3.19: Experimental seek results (0.1745 rad)

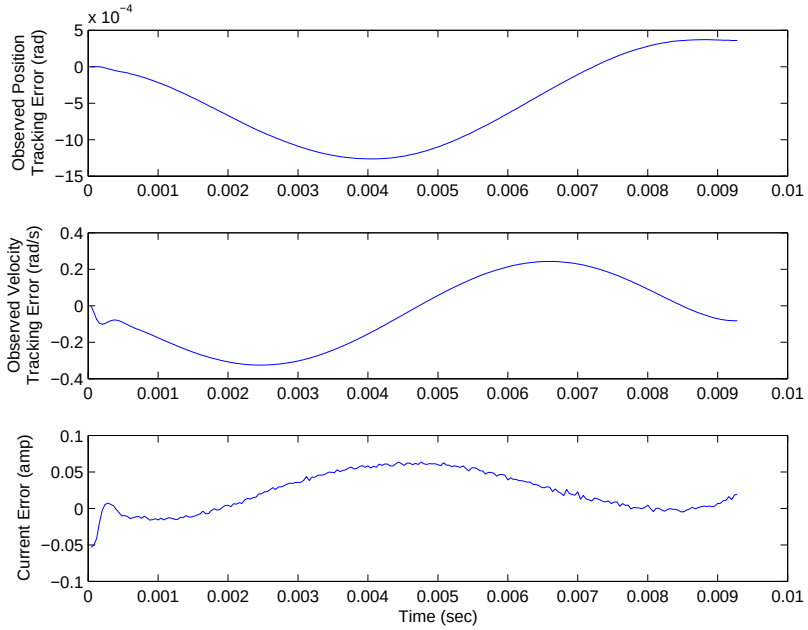

Figure 3.20: Experimental seek error (0.0873 rad)

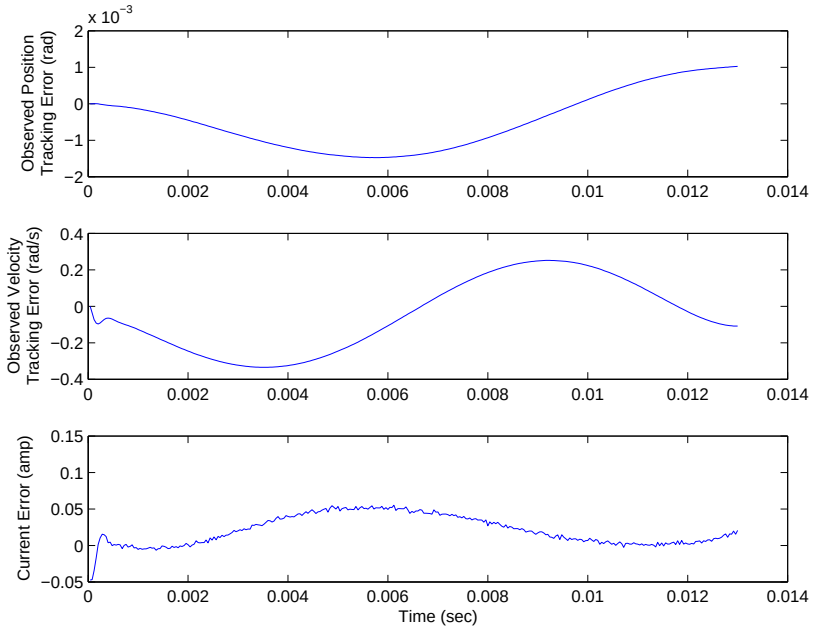

Figure 3.21: Experimental seek error (0.1745 rad)

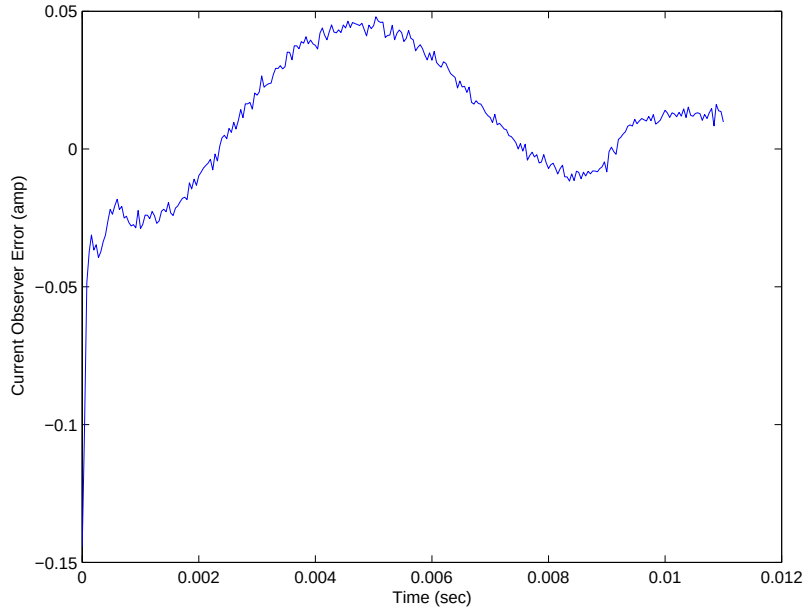

Figure 3.22: Experimental seek with observer initial condition (0.0873 rad)

3.6 Summary

Efforts were undertaken to evaluate seek control designs that compensate for a disk drive actuator influenced by nonlinear bias effects. A linear state-feedback and an adaptive controller were developed to track predetermined reference trajectories. Simulation results revealed that the performance of both controllers was within the required specifications. Overall, the adaptive controller was capable of tracking with less error and comparable power. Experiments were conducted to verify the simulation results and experiments confirmed that the adaptive control outperforms state-feedback with slightly more power consumption. Since bounds on the bias estimate were known, a projection algorithm was implemented to constrain the bias estimate within the known bounds. Although the performance criteria were met, adding projection resulted in a tracking performance reduction compared to the control law without projection. The adaptive controller adds a degree of complexity to the overall implementation and practical memory or processor resources may not be available. Therefore, performance effects from variation in bias estimate accuracy and sample rate were investigated. It was determined that controller performance lost by a reduction in bias modeling accuracy could be recovered by an increase in sample rate. Therefore, if sampling resources are available, the complexity of the controller can be reduced without a significant sacrifice in performance.

Because direct velocity measurement is typically unavailable in production disk drives, the research also investigated solutions in the absence of full-state feedback. The bias nonlinearity was shown to be locally Lipschitz and an output feedback tracking controller, using only current measurement, was developed for the actuator performing a seek maneuver. The output feedback controller was shown to be exponentially stable and satisfy the separation principle. Experiments show the controller

to successfully track predetermined reference trajectories with a bias 5% of the maximum available torque. The position and velocity tracking error increased with seek length while current error decreased. Experiments also revealed observer convergence with initial condition variation.

CHAPTER 4

THE COMMUTATIONAL RAMP LOAD ACTUATOR

The following chapter focuses on the design of a disk drive actuator with a unique application to ramp loading. The solution retains the linear shock resistance of ramp loading while realizing the cost and performance benefits of a conventional actuator. Material costs from larger magnets and coils typically inherited with ramp load designs are eliminated.

The ramp load actuator design and performance requirements are presented in Section 4.1 along with specifications for rotary shock. A nominal ramp load actuator is designed in parallel and compared with the new proposed commutational design. Section 4.2 develops a model of the system and reveals conditions at which the actuator is uncontrollable. The shock and move-time performance is verified in Section 4.3 with simulation analysis. In Section 4.4, a unique disk drive is fabricated with the designed actuator to support commutational ramp loading. The actuator physical parameters are measured to verify and validate the proposed design. A summary is given in Section 4.5.

4.1 Actuator Design

This section discusses the details of a disk drive actuator design for commutational ramp loading. Performance criteria and design constraints are outlined to establish target goals. Voice-coil motor actuators for both nominal and commutational configurations are developed in parallel for comparison. The framework for a ramp and magnetic bias design is also presented for the commutational configuration.

4.1.1 Design Constraints/Requirements

Because the overall geometric form factor and operating environment remain within the industry standards, the commutational ramp load disk drive maintains design constraints analogous to those described in Section 2.1. However, contrary to the actuator designed in Chapter 2, this particular disk drive is targeted for a high-end, server application where data throughput is considered a top priority. Therefore, more emphasis is required on actuator performance rather than cost and rotational shock resistance. The requirements being considered for this particular disk drive application are given in Table 4.1.

Table 4.1: Actuator design constraints

Parameter	Spec
Max third-stroke move-time	6 msec
Max PCB Flux leakage	100 Gauss
Coil mass	1.25 grams
Rotary shock amplitude	30 krad/s^2
Rotary shock pulse width	2 msec
Voltage saturation limit	11 V
Actuator profile	2236 mm^2
Acutator height	15.75 mm
Data zone width	20.93 mm

4.1.2 Voice Coil Motor

For comparison, a nominal ramp load voice-coil motor was designed in parallel with the new, proposed commutational actuator. Both designs were optimized based on the constraints defined in the previous section. The following differences highlight

the additional design flexibility inherent to the proposed, commutational ramp load actuator:

1. Decreased magnet arc length results in reduced active magnet surface area. Since gap flux density is inversely proportional to magnet surface area, gap flux density increases along with available torque. A cost reduction is also realized.

2. The arc length reduction allows a decrease in the *inactive* coil lengths. Since this area provides no torque contribution, it can be eliminated resulting in a potential rotary arm inertia reduction. If it is desired to maintain the inertia, *active* length can be added to the coil thereby minimizing a torque generation performance impact.

3. The ramp arc length can be increased allowing for increased travel distance along the ramp. Therefore, ramp friction along with magnetic and flex bias forces can be used to combat the effects of rotational shocks possibly rendering a latch requirement unnecessary.

4. Following from items 1 and 3, if performance takes priority over cost, the designer has the option of using the latch space for extra steel to provide an additional flux path which improves the efficiency of the magnetic circuit. Increased magnet thickness would increase the gap flux density along with available torque.

Two motors were developed using the geometric constraints of Section 4.1.1. The high performance design path relative to item 4 was chosen for the proposed commutational ramp load actuator design. Therefore, the coil and rotary arm were designed for minimal inertia within resonance stiffness constraints. Additional steel will be added to enhance the flux density of the magnetic circuit and the rotary shock specification will be met without an additional latching mechanism. The design methods used for

the coil and magnetic circuit are analogous to those in Section 2.2. In order to balance the rotary arm, a coil mass of 1.25 grams was required and pure copper was selected as the material for the conductor. Iteration on the diameter and length was performed until the mass and profile targets were met for both coil designs. The resistance and inductance of the coil was calculated using (2.1) and (2.2), respectively. Table 4.2 lists the results from the coil lumped parameter design for both actuators. The coil design coupled with the arm resulted in a motor inertia of 38.76 and 37.63 $g \cdot cm^2$ for the nominal and commutational L/UL rotary arms, respectively. The arm length was 45.72 mm resulting in a sweep angle of 0.4619 rad. As described in Section 2.2, form factor constraints restrict the magnetic circuit profile and the air gap is fixed by the coil thickness.

Table 4.2: Lumped parameter coil design.

Parameter	Nom. L/UL	Comm. L/UL
Conductor	Copper	Copper
Wire diam. (mm)	0.1549	0.1575
Mean turn (mm)	77.47	67.1
Bobbin area (mm^2)	37.67	31.39
Thickness (mm)	1.194	1.524
Turns	96	104
Resistance (Ω)	6.56	6.21
Inductance (mH)	0.335	0.323
Mass (g)	1.25	1.24

Therefore, optimization becomes a function of magnet and steel pole thickness. Neodymium-Iron-Boron high energy magnet material was used with an energy of 398 kJ/m^3. The optimized magnetic circuit design parameters of Table 4.3 resulted in demagnetization load lines [21] of 1.85 and 2.3 and data zone torque factors, K_t,

Table 4.3: Magnetic circuit design comparison

Parameter	Nom. L/UL	Comm. L/UL
Overall height (mm)	15.875	15.875
Pole transition length (mm)	27.94	27.94
Pole thickness (mm)	4.572	3.02
Magnet thickness (mm)	2.032	2.89
Magnet area (mm^2)	346.77	314.51
Air gap thickness (mm)	2.201	2.5146
Steel saturation (Tesla)	1.7	1.7
Air gap flux density (Tesla)	0.912	0.963

of 0.0567 and 0.0651 $N \cdot m$/amp for the nominal and commutational L/UL designs, respectively. The design was further refined with magnetic finite-element modeling.

4.1.3 Magnetic Bias Design

Latches, in ramp load disk drives, are used to hold the actuator arm at the nominal shipping location in the event of a rotational shock. The nominal shipping location is typically a state when the arm is resting against a rigid member called the outer crash stop (OCS) with R/W heads parked off the disk surface. With the proposed commutational ramp load actuator, it was desired to design a bias force across the ramp angle to restore the arm back to the nominal shipping location after the impact of a rotational shock. The methods from Section 2.2.3 were used to determine the necessary bias energy. However, in this case the strategy is to design the magnetic bias torque, *complemented with ramp friction*, that applies an energy greater than or equal to that of the shock ($E_b \geq E_s$). The total bias energy prohibits the arm from traveling past a desired angular displacement. For this design, it is required that the arm angular displacement resulting from rotational shock be less than the total

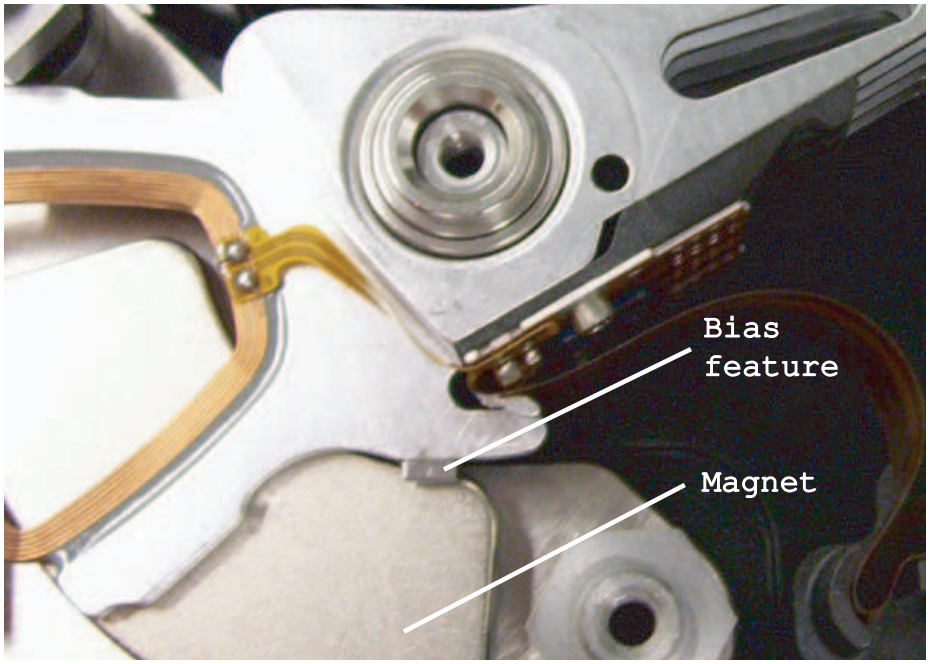

Figure 4.1: Magnetic bias feature

ramp angle, θ_r. Using equations (2.10) through (2.12) and the shock specifications of Table 4.1, the shock energy was determined to be 2.75 mJ. As in Section 2.2.3, a passive magnetic bias was obtained by attaching a steel member to the arm and partially protruding into the air gap of the magnetic circuit. Figure 4.1 illustrates the magnetic bias feature design for the commutational ramp load actuator. To avoid the issues of bias impact during seeking operations described in Chapter 3, it was desired the bias dissipate prior to actuator arm entry into the data zone. During the shock phase, bias and friction work together to bring the arm to rest after traveling some angular displacement along the ramp. A subsequent restoration phase must occur to return the arm back to the OCS. Because the friction forces oppose the direction of actuator motion, the magnetic bias must overcome friction during the restoration phase. The overall bias design results in the following energy relationships

$$E_b = E_m + E_f \geq E_s, \quad E_m > E_f \tag{4.1}$$

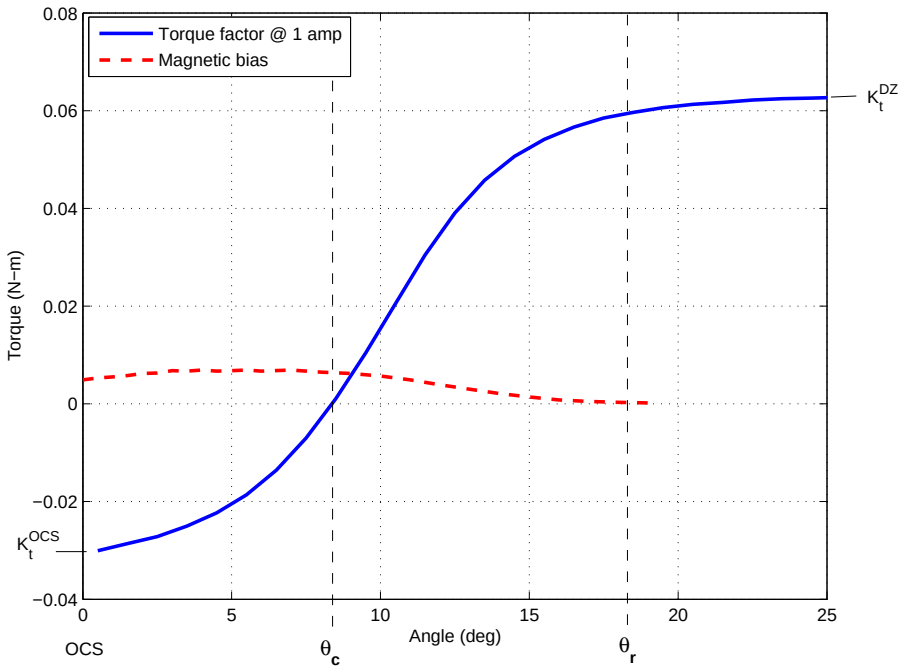

Figure 4.2: Actuator torque profiles along the ramp angle, θ_r.

where E_m and E_f are the energies from magnetic bias and friction, respectively. Using finite-element analysis, shaping of the magnetic torque profile was achieved by changing the location and geometric parameters of the steel. The energy of the torque profile throughout the ramp angle was calculated from (2.13), where $\theta_T = \theta_r$, and desired to be larger than the shock energy computed from (2.12). The total bias energy, ψ, contains both magnetic and friction components

$$\psi(\theta) = T_b(\theta) + T_{fx}, \quad T_b(\theta) = \sum_{k=0}^{n} c_k \theta^k \tag{4.2}$$

where the bias torque, T_b, can be represented as a polynomial function of angular position with coefficients, c_k, and T_{fx} is the maximum dynamic friction component represented by viscous and coloumb effects. The resulting FEM torque factor and magnetic bias characteristics along the ramp angle are shown in Figure 4.2.

4.1.4 Ramp Design

Traditional ramp L/UL designs require additional magnet material to provide actuation for rotating the actuator arm off the disks. Typical ramp designs minimize arc length to reduce the extra costs associated with magnetic material. For the commutational L/UL actuator, more angular rotation off the disk is actually preferred. It is desirable to rotate the arm far enough off the disks so that the single coil active length is within the region of uniform magnetic field (recall Fig. 1.10). This will maximize the available torque at the beginning of a load maneuver. Also, greater travel along the ramp will increase the energy available for a magnetic bias and friction to resist the effects of rotational shock. Other than the total ramp arc length, the standard considerations were taken into account when designing the ramp. The maximum vertical load velocity is the velocity the heads can depart the ramp without impacting the disk surface. This velocity is a function of the air bearing hydrodynamic analysis. Based on the air bearing hydrodynamics, the maximum vertical load velocity was determined to be 54 mm/s. The ramp thickness was set by the vertical geometric restrictions on disk spacing. The desired ramp arc length and ramp thickness resulted in a departure angle of 0.21 rad relative to the disk surface. The maximum allowable horizontal loading velocity was 254 mm/s and determined from the vertical velocity and ramp departure angle.

An injection molding process was desired for ramp manufacture and a polyphenylene sulphide (PPS) was selected as the ramp material. The PPS was impregnated with 5% polytetrafluoroethylene (Teflon®) to achieve a desired $\mu = 0.15$ friction coefficient between the ramp and lift tab satisfying equation (4.1). A 5% carbon fiber was also used for electrostatic discharge protection. Results of the ramp design are summarized in Table 4.4.

Table 4.4: Ramp design parameters

Parameter	Spec
Ramp thickness	1.5 mm
Ramp departure angle	0.21 rad
Ramp centerline radius	48.3 mm
Ramp vertical spacing	2.2 mm
Lift tab/ramp friction coef.	0.15
Max vertical load velocity	54 mm/s
Max horizontal load velocity	254 mm/s

4.2 Modeling

The ramp load disk drive actuator can be described by a combination of mechanical and electrical dynamic equations. The mechanical dynamics are represented by

$$J\ddot{\theta} = K_t(\theta)i - T_b(\theta) - T_f \text{ sat}(\dot{\theta}) \tag{4.3}$$

where θ is the actuator arm angular position, J is the actuator inertia, and i is the current applied in the coil. The torque factor, K_t, which is relatively constant during operation in the data zone, becomes a function of the actuator arm angle while on the ramp. There exists a condition rendering the actuator uncontrollable by induced current while traveling on the ramp. Figure 4.2 illustrates the torque factor characteristics along the ramp angle. The uncontrollable condition occurs at a "critical angle", θ_c, corresponding to $K_t(\theta_c) = 0$. The critical angle is measured as the actuator rotates counter-clockwise from the parked position at the outer crash stop (OCS). The ramp angle, θ_r, is the total angle the actuator travels from the OCS to the end of the ramp. Since the magnitude of the torque factor decreases as the actuator approaches the critical angle, it is advantageous to design the ramp angle such that a single active length is within the uniform magnetic field region of the air

gap when parked at the OCS. This will ensure torque is maximized at the beginning of a maneuver and provides the relationship

$$K_t^{DZ} \approx -2K_t^{OCS}$$

where K_t^{DZ} and K_t^{OCS} are the torque factor in the data zone and at the outer crash stop, respectively. As described in Section 4.1.3, the bias torque, $T_b(\theta)$, is a function of actuator arm angle and is required to prevent an unrecoverable condition at θ_c that may be induced by an external disturbance. The bias assists the actuator in returning to the OCS without requiring current to be present in the coil. The friction torque, $T_f \,\mathrm{sat}(\dot{\theta})$, results from the suspension lift tab/ramp surface interaction during a L/UL operation and is dependent on the direction of actuator motion. A saturation function is used to represent viscous and coloumb effects

$$T_f \,\mathrm{sat}(\dot{\theta}) = \begin{cases} T_{fx}, & \dot{\theta} > \omega_x \\ \frac{T_{fx}}{\omega_x}\dot{\theta}, & -\omega_x \leq \dot{\theta} \leq \omega_x \\ -T_{fx}, & \dot{\theta} < -\omega_x \end{cases} \tag{4.4}$$

where T_{fx} is the maximum dynamic friction torque and ω_x is the angular velocity at which that torque is attained. Equation (4.5) represents the electrical dynamics where R and L are the coil resistance and inductance, respectively.

$$V_s = Ri + L\frac{di}{dt} + K_t(\theta)\dot{\theta} \tag{4.5}$$

The supply voltage, V_s, is available as input to the system. Referring to Figure 4.2 and noting that

$$K_t(\theta) \begin{cases} < 0, & \theta < \theta_c \\ = 0, & \theta = \theta_c \\ > 0, & \theta > \theta_c \end{cases} \tag{4.6}$$

the commutation requirement becomes apparent by rearranging (4.3) and (4.5) as

$$\frac{d^2\theta}{dt^2} = \frac{1}{J}\left[K_t(\theta)i - T_b(\theta) - T_f \,\mathrm{sat}(\dot{\theta})\right] \tag{4.7}$$

$$\frac{di}{dt} = \frac{1}{L}\left[V_s - K_t(\theta)\dot{\theta} - Ri\right] \tag{4.8}$$

When $\theta < \theta_c$, $K_t(\theta) < 0$. Therefore, from (4.7), $i < 0$ is required to overcome the bias and friction torques and move the actuator a positive angular displacement toward the end of the ramp. When $\theta > \theta_c$, $K_t(\theta) > 0$ and the current must change sign ($i > 0$) to maintain the direction of actuator motion.

The motor torque factor and bias can both be represented as m and n-th order polynomial expressions, respectively of the form

$$K_t(\theta) = \sum_{k=0}^{m} b_k \theta^k \qquad T_b(\theta) = \sum_{k=0}^{n} c_k \theta^k \tag{4.9}$$

where b_k and c_k are the k-th order coefficients. For $\theta > \theta_r$, magnetic bias and friction torque vanish and $K_t^{DZ} = K_t(\theta > \theta_r)$ is relatively constant throughout the data zone resulting in a linear model representation.

4.3 Performance Analysis

It is necessary to determine if the design meets the performance requirements outlined in Section 4.1.1. Using the resulting design parameters of the previous section, fulfillment of the requirements are evaluated through simulation.

4.3.1 Non-operational Shock Performance

Based on the bias and ramp designs of Section 4.1.3 and 4.1.4, respectively, the system resistance to a rotational shock could be determined. The drive state is non-operational, so the supply voltage is removed and the shock input, α_s, as defined in (2.9) enters the dynamics of (4.7) and (4.8) as

$$J\frac{d^2\theta}{dt^2} = K_t(\theta)i - T_b(\theta) - T_f \,\mathrm{sat}(\dot{\theta}) + J\alpha_s \tag{4.10}$$

$$L\frac{di}{dt} = -K_t(\theta)\dot{\theta} - Ri \tag{4.11}$$

Table 4.5 depicts the results of a tolerance analysis on the system physical parameters. Worst-case bounds were chosen on each parameter that would exhibit maximum

Table 4.5: System physical parameters for shock robustness

Parameter	Spec
Acutator inertia	37.63 ± 1.13 g $\cdot$ cm^2
Torque factor	$\pm 7\%$
Coil resistance	$6.21 \pm 0.31\,\Omega$
Coil inductance	0.323$\pm$0.013 mH
Bias feature volume	7.38$\pm$0.15 mm^3
Bias feature position	$\pm$0.15 mm
Ramp dynamic friction	0.12$\pm$0.014 N$\cdot$mm
Lift tab/ramp position	0$\pm$0.0037 rad

angular displacement of the rotary arm for the half-sine pulse acceleration shock. Simulations reveal the system can withstand up to 34 krad/s^2 and be restored back to the nominal, parked position at the OCS (Fig. 4.3) meeting the 30 krad/s^2 minimum requirement of Section 4.1.1. The peak displacement is about 0.28 rad which is less than the ramp angle of $\theta_r = 0.314$ rad. In this case, both bias and friction work against the actuator arm response to a shock. When the actuator finally rests at some point within the ramp angle, the bias is required to restore the actuator arm back to the OCS. Recall that friction torque works against the bias during the restoration stage. Therefore, the bias torque must always exceed the friction torque at all positions within the ramp angle. This may discourage the designer from relying too heavily on friction for rotary shock protection as head population increases.

4.3.2 Move-time Performance

The move-time performance of the motor was evaluated based on an open-loop, time-optimal maneuver. The objective of the time-optimal maneuver is to choose an input that moves the actuator from rest to a desired position, θ_f, in the shortest

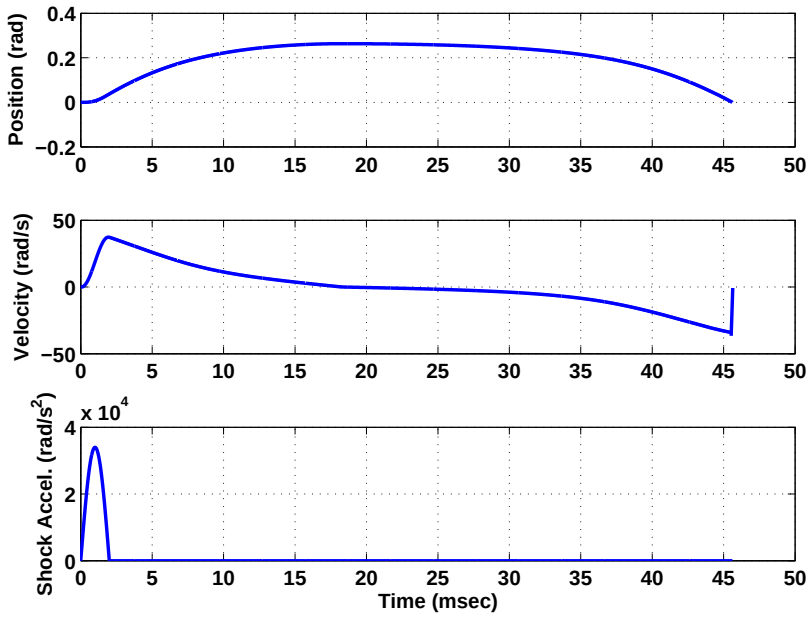

Figure 4.3: Rotational shock performance

possible time. The optimal input to obtain minimum-time response is maximum effort throughout the interval of operation [31]. For a stable, linear differential equation of order n, it has been shown [32] that the solution will be optimized if the input is chosen to take the saturation voltage value of $+V_{sat}$ or $-V_{sat}$ in the required time interval $[0, t_f]$ and reverse polarity $n-1$ times at appropriate instances. Bias from magnetic and friction influences are no longer present in the data zone and the torque factor becomes constant. Therefore, the third-order dynamics of (4.3) and (4.5) become linear. For a third-order linear system, the input voltage command will be maximum available and switch sign twice

$$V_s = \begin{cases} V_{sat}, & 0 \le t \le t_1 \\ -V_{sat}, & t_1 \le t \le t_2 \\ V_{sat}, & t_2 \le t < t_f \\ 0, & t \ge t_f \end{cases} \tag{4.12}$$

Table 4.6: Dynamic model parameter comparison

Parameter	Nominal L/UL	Commutative L/UL
Torque factor (N-mm/amp)	56.73	65.06
Inertia (g-cm^2)	38.76	37.63
Coil resistance (Ω)	6.56	6.21
Coil inductance (mH)	0.335	0.323
Voltage limit (V)	11	11
Move angle (rad)	0.154	0.154

The input switches polarity within the interval at times t_1 and t_2. The switch times of the third-order system were determined using the boundary conditions and solving a set of simultaneous equations. The equations are elaborate, however, and require a numerical, iterative solution [33]. Switch and move-time results were computed for the values listed in Table 4.6. The third-stroke, time-optimal moves were completed in 5.11 msec and 4.60 msec for the nominal and commutative designs, respectively. Therefore, a 10% performance increase was noticed with the commutative design using the enhancement items discussed in Section 4.1.2. Figure 4.4 shows the time-optimal move comparison across the data zone.

4.4 Experimental Validation

This section discusses the verification and validation of the overall ramp load actuator system. Extensive measurements were taken to verify the design parameters calculated in Section 4.1. Two disk drives were fabricated and experiments were performed to determine the actual shock capability of both. The open-loop characteristics of the system are discussed in Section 4.4.3 and the behavior of the actuator as it moves through the critical angle is revealed.

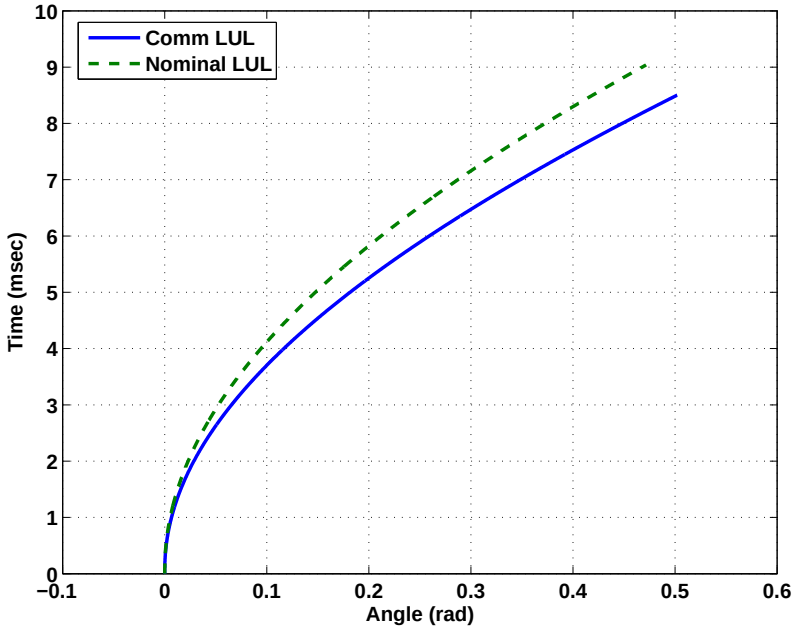

Figure 4.4: Time-optimal move comparison in the data zone

4.4.1 Actuator Physical Parameters

A prototype disk drive was fabricated (Fig. 4.5) corresponding to the design of the previous sections. An effort was undertaken to verify the design of all performance parameters contributing to the system dynamics. A linear stepper motor was outfitted with a gaussmeter probe to measure gap and leakage flux densities. The magnetic circuit assembly was mounted to a rotational stepper motor to produce angular motion relative to the probe. The system was automated and gauss measurements were taken at 1.27 mm and 0.0157 rad increments of linear and angular displacement, respectively. The gap flux density results are shown in Figure 4.6. The gap flux density becomes more uniform approaching the magnet pole center, typical in disk drive magnetic circuit designs, and peaks at approximately 0.929 Tesla. The leakage was measured in a plane 3.71 mm from the lower steel surface simulating the nominal distance of the PCB location. Figure 4.7 shows the PCB measurement area influenced by flux leakage underneath the magnetic circuit. The maximum leakage flux density

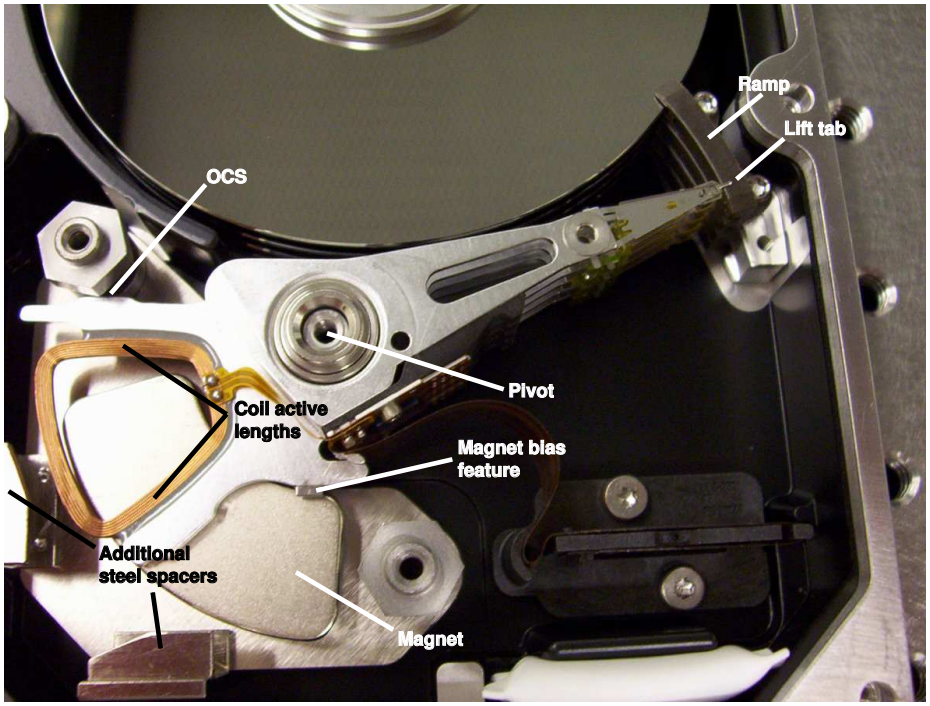

Figure 4.5: Commutational ramp load disk drive.

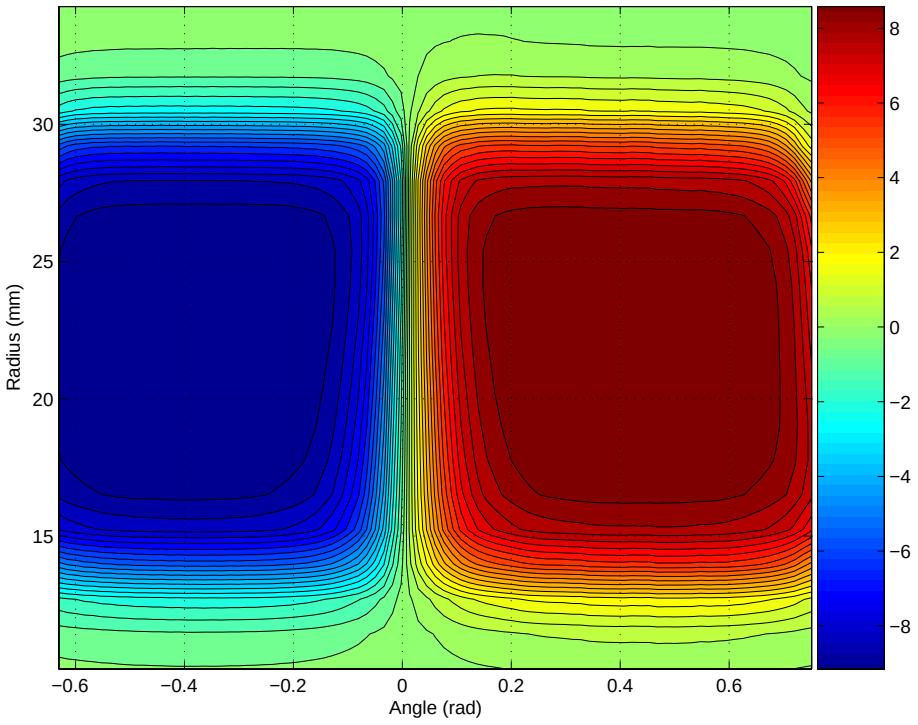

Figure 4.6: Measured air gap flux density (Tesla)

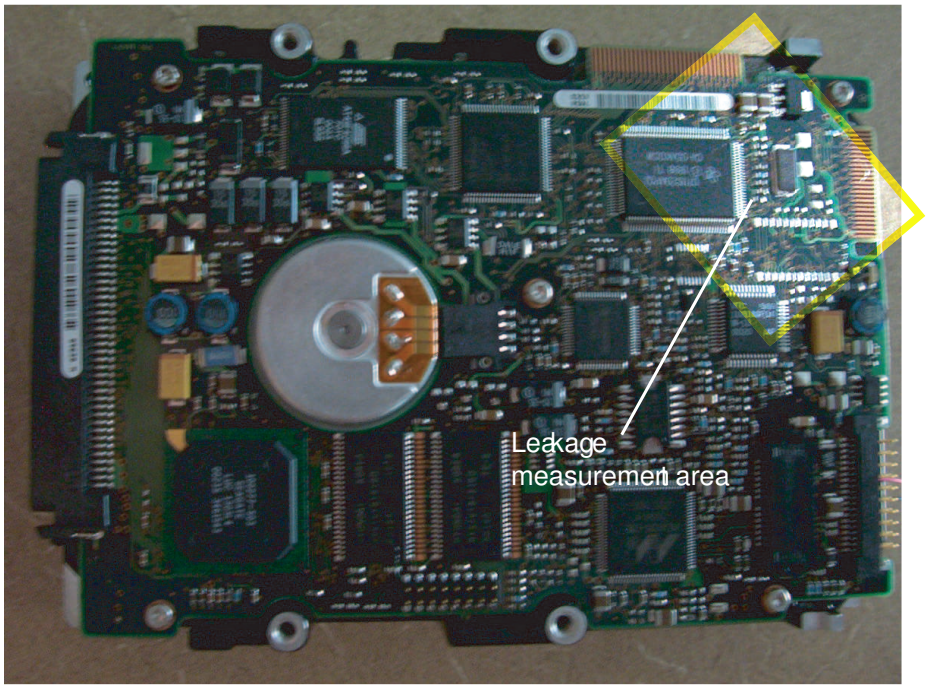

Figure 4.7: Leakage measurement area at PCB location

of 81.6 Gauss (Fig. 4.8) occurred along the magnetic pole transition projection well below the requirement of Table 4.1.

A test fixture was available where a ramp could be supported by two perpendicularly aligned load cells. As the actuator moved along the ramp, the normal and tangential force produced by the lift tab was recorded. The lift tab normal force on the ramp, F_s, was measured at 2.5 grams. The ratio of the tangential force and normal force resulted in the desired friction coefficient, $\mu = 0.15$. The torque resulting from friction is $T_f = n_h\, r_p \mu F_s$, where r_p =0.048 m is the distance from actuator pivot to lift tab and $n_h = 4$ is the number of heads (lift tabs) with which the actuator is populated.

A fixture was designed that allowed a torque sensor to be attached directly to the actuator pivot. Current was injected in the coil of a rotary arm without magnetic bias and the resulting torque was recorded. Beginning with the actuator arm parked at the OCS, the torque factor was measured across the entire sweep angle of approximately

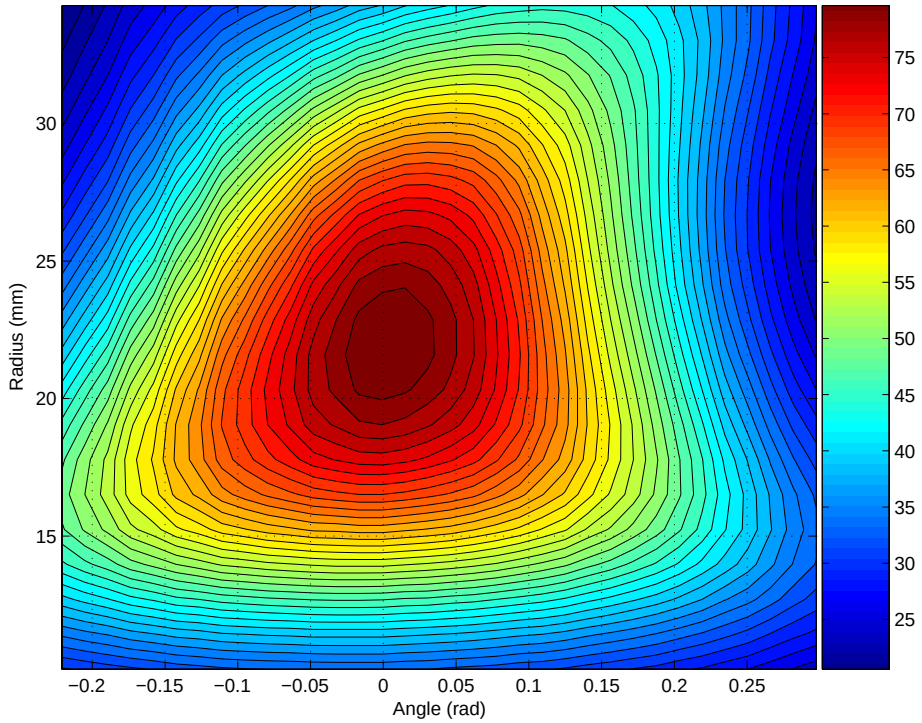

Figure 4.8: Leakage flux density at PCB location (Gauss)

45°. The first 18° of rotation occurs on the ramp ($\theta_r = 18°$) in which the motor torque factor undergoes a sign change. The critical angle was measured at $\theta_c = 8.3°$, where $K_t(\theta_c) = 0$. The test was repeated without current injection for a magnetically biased actuator. Measurements for torque factor and bias along the sweep angle were compared to theoretical results and shown in Figure 4.9. A reduction of 4.4% and 3.6% were noted for torque factor and bias, respectively. The polynomial coefficients corresponding to (4.9) are given in Table 4.7.

Table 4.7: Polynomial coefficients

$k \longrightarrow$	6	5	4	3	2	1	0
b_k	921.46	-586.51	58.82	19.59	-2.379	0.1705	-0.0316
c_k	–	–	–	0.6989	-0.4666	0.0636	0.0046

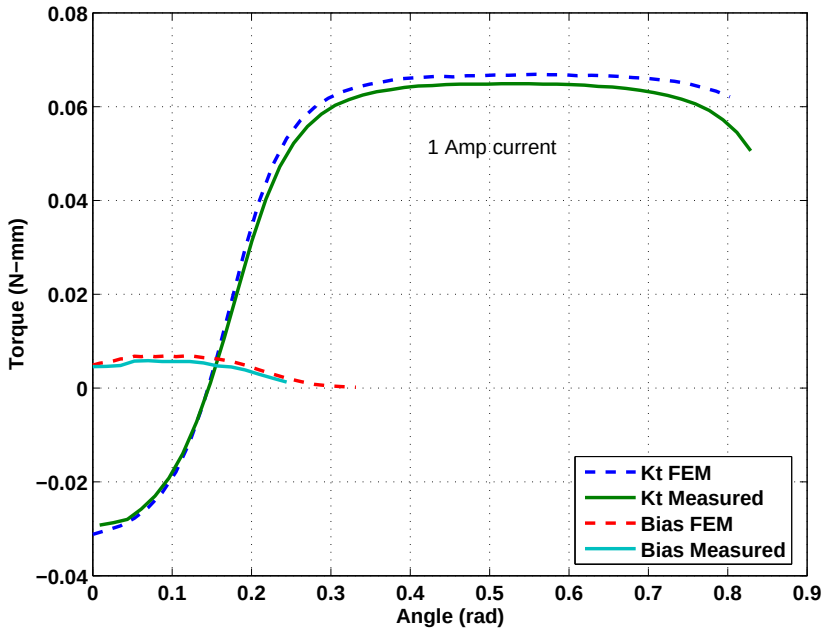

Figure 4.9: Comparisons for torque factor and bias

The inertia was determined by mounting the rotary arm assembly pivot to a structure with a known torsional spring constant. An impulse was delivered to the inertia/spring system and the natural frequency was observed resulting in $J = k_t/\omega_n^2$, where k_t is the torsional spring constant and ω_n is the measured natural frequency. The inertia was calculated to be 38.49 g$\cdot$cm^2 which is approximately 2.3% more than predicted in Section 4.1.2. Resistance and inductance were measured with standard metering equipment resulting in values of 6.26 Ω and 0.311 mH, respectively. Reevaluation of the shock and move-time performance for the measured values resulted in 32 krad/s^2 and 4.76 msec, respectively.

4.4.2 Rotational Shock Performance

Two of the prototype disk drives were tested for shock performance on a rotary shock table. The table rotation axis was located about the actuator arm pivot center to represent a worst case rotational shock. The experiments were designed as pass/fail

by inspecting the drive for damage after each shock. Shock levels of 20, 30, 35, and 40 krad/s^2 were imparted to each drive. The actuator arms on both drives were restored back to the OCS for levels up to 35 krad/s^2 without failure meeting the 30 krad/s^2 specification. Shock tests at 40 krad/s^2, however, forced the heads off the ramp and into the data zone. The heads adhered to the surface of the disk and could not be recovered. Disk slippage was noticed on one drive after testing at 35 krad/s^2 resulting from insufficient clamping force on the disk pack.

4.4.3 Open-Loop Analysis

An experiment was performed to demonstrate the dynamic characteristics of the actuator moving through the critical angle. The actuator was driven by digital signal processor (DSP) hardware with analog I/O peripherals. Voltage output from the DSP hardware was injected through a bipolar amplifier and into the ramp L/UL disk drive of Figure 4.5. Current feedback was achieved by measuring the voltage drop across a 0.2 Ω sense resistor connected in series with the actuator coil. The experimental setup is shown in Figure 4.10. With the actuator arm positioned on the ramp against the OCS, a -6 volt, 7 msec pulse was injected into the coil. The procedure was repeated with the R/W heads positioned off the ramp and inside the data zone. The behavior of current was recorded for both scenarios and is shown in Figure 4.11. Notice that as the actuator arm moves along the ramp, the critical angle, θ_c, can be identified by a polarity reversal in the current measurement when the input voltage is zero. Although the arm is moving, the back-emf (torque) factor is zero at θ_c, hence current is not induced. Any maneuver in the data zone, however, always induces a current in the coil even after the voltage is removed. The rate of current decay is larger in the data zone resulting from a higher back-emf (torque) factor in that area.

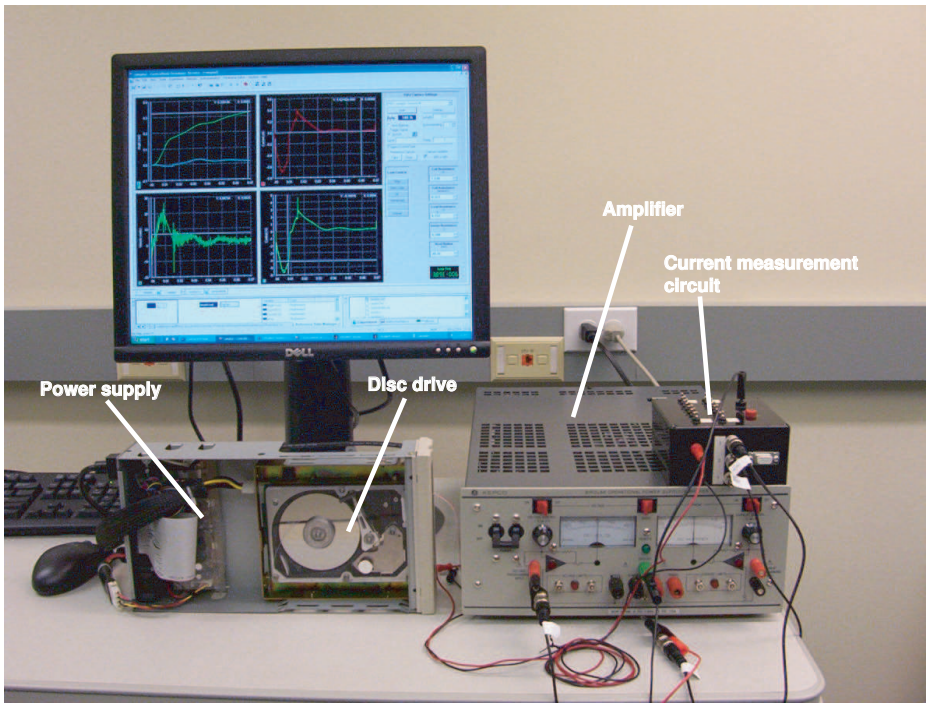

Figure 4.10: Experimental setup for ramp load control

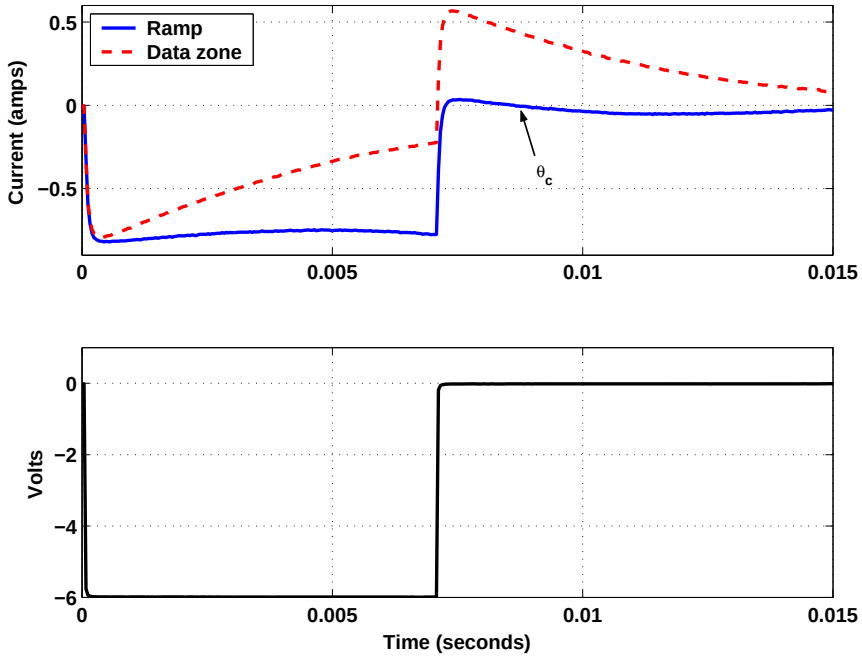

Figure 4.11: Open-loop maneuver comparison

4.5 Summary

A unique actuator system for disk drive ramp loading was designed, possessing both low cost and higher performance characteristics over nominal designs used in industry today. When compared to a nominal ramp load design, a 10% reduction in move-time was exhibited with the proposed commutational actuator design. Therefore, it is no longer necessary to trade-off increases in move-time or material costs for the shock resistant advantages of ramp loading. A low cost, magnetic bias was designed to restore the actuator to the nominal shipping location and prevent equilibrium in a region of uncontrollability exhibited along the ramp angle. The bias, when combined with ramp friction, also allows the actuator to meet common industry non-operational, rotary shock requirements. A prototype disk drive was manufactured using the proposed design criteria and experiments were conducted to validate the design parameters.

CHAPTER 5

DYNAMIC ANALYSIS OF THE COMMUTATIONAL RAMP LOAD ACTUATOR

The disk drive actuator designed in the previous chapter provides a lower cost, ramp load solution compared to existing ramp load designs used in industry today. Linear shock resistance is preserved and a performance increase is realized by optimizing the magnetic circuit and arm inertia with the resulting new geometry. There exists, however, a location on the ramp where the actuator exhibits an uncontrollable, input singularity. This chapter characterizes the commutational ramp load (CRL) actuator dynamics in detail and compares the behavior to that of the well-known ball and beam system (BBS) that has enjoyed considerable attention throughout the literature. Although both systems possess similar characteristics, analysis reveals the deficiency of existing control solutions to properly handle the CRL actuator dynamics. The chapter concludes with a sufficient condition for successfully maneuvering through the uncontrollable singularity providing a basis for reference trajectory design. Some mathematical preliminaries necessary for the following theoretical development initiate the discussion.

5.1 Preliminaries

Consider the SISO system of the form

$$\begin{aligned} \dot{x} &= f(x) + g(x)u \\ y &= h(x) \end{aligned} \tag{5.1}$$

defined on a smooth, connected, n-dimensional manifold, M. The mappings $f : M \to \mathbb{R}^n$ and $g : M \to \mathbb{R}^n$ are drift and input vector fields defined on M, respectively. The output map $h : M \to \mathbb{R}$ is also smooth.

Definition 5.1 *A function $\delta(x)$ is $O(x)^m$ if there exists $k \in \mathbb{R} \setminus 0$ such that*

$$\lim_{|x|\to 0} \frac{|\delta(x)|}{|x|^m} = k.$$

Let $U_\epsilon \subset M$ such that when $\delta < \epsilon,\ \sup\{\delta \mid B_\delta \subset U_\epsilon\} = \epsilon$ where B_δ is a ball of radius δ centered at the origin.

Definition 5.2 *A function $\beta : \mathbb{R}^n \times \mathbb{R} \to \mathbb{R}$ is said to be uniformly higher order on $U_\epsilon \times B_\sigma \subset \mathbb{R}^n \times \mathbb{R},\ \epsilon > 0$, if for some $\sigma > 0$, there exists a monotone increasing function, $W(\epsilon)$, such that*

$$|\beta(x,u)| \leq \epsilon W(\epsilon)[|x| + |u|], \quad x \in U_\epsilon,\ |u| \leq \sigma. \tag{5.2}$$

Because the control task will invariably be that of steering the system (5.1) to track some predetermined reference trajectory, it is of interest to determine what states, $x_f \in M$ are *reachable* from some other arbitrary initial state, $x_0 \in M$. Let $V^\infty(M)$ be the Lie algebra of C^∞ vector fields on M.

Definition 5.3 *The controllability algebra, $\mathcal{C}$, is the smallest subalgebra of $V^\infty(M)$ that contains f, g.*

Definition 5.4 *The controllability distribution, $\Delta_\mathcal{C}(x)$ is the distribution generated by the controllability algebra*

$$\Delta_\mathcal{C}(x) = \text{span}\{X(x) \mid X \in \mathcal{C}\}.$$

Since $\mathcal{C}$ is a subalgebra it follows that $\Delta_\mathcal{C}$ is involutive.

Definition 5.5 (Reachability) *The system* (5.1) *is locally reachable from a point* $x_0 \in M$ *if there exists a neighborhood* V *of* x_0 *such that for each* $x_f \in V$*, there exists* $T > 0$*, class* K *function* ζ*, and* $u = \{u(t) \mid \|u\| \leq \zeta(\|x\|), t \in [0, T]\}$*, where the system starting at* x_0 *and time* $t = 0$*, reaches* x_f *at time* T*.*

Let $R^V(x_0, T)$ be the reachable set from x_0 at time $T > 0$, following trajectories which remain for $t \leq T$ in the neighborhood V of x_0. Furthermore, define the cumulative reachable set as

$$R_T^V(x_0) = \bigcup_{\tau \leq T} R^V(x_0, \tau)$$

Theorem 5.1 (Controllability rank condition) *Consider the nonlinear system* (5.1) *with dynamics on an* n*-dimensional manifold,* M *and local coordinates* $(x_1, \ldots, x_n)$*. If*

$$\dim \ \Delta_{\mathcal{C}}(x_0) = n \tag{5.3}$$

at a point $x_0 \in M$*, then for any neighborhood* V *of* x_0 *and* $T > 0$ *the set* $R_T^V(x_0)$ *contains a non-empty subset of* M*. If* (5.3) *holds for all* $x \in M$*, then the system is locally reachable.*

Although a system may violate Theorem 5.1, observing a condition where $0 < \dim \ \Delta_{\mathcal{C}}(x_0) < n$ may warrant further analysis as the following definition and lemma suggest.

Definition 5.6 *A submanifold* S_x *is an integral manifold of a distribution* Δ *on* M *if*

$$T_x S = \Delta(x), \quad \forall\, x \in S_x$$

where $T_x S$ is the tangent space of S_x at x.

Lemma 5.1 *If $\Delta_{\mathcal{C}}(x_0)$ is a controllability distribution of* (5.1) *at x_0 and* $\dim \Delta_{\mathcal{C}}(x_0) = k < n$*, then there exists a submanifold*

$$S_{x_0} := \{x \in M \mid x_{k+1} = p_{k+1}, \ldots, x_n = p_n\} \tag{5.4}$$

such that S_{x_0} is an integral manifold of $\Delta_{\mathcal{C}}(x_0)$ for each fixed set of constants, $p_{k+1}, \ldots, p_n$.

The totality of submanifolds parameterized by constants $p_{k+1}, \ldots, p_n$ forms a foliation of M and each submanifold (5.4) is a leaf of this foliation.

The interested reader is referred to [34, 35, 36, 37] for a more comprehensive insight to the material of this section.

5.2 Approximate Input/Output Linearization of Nonregular Systems

The input/output relationship of (5.1) can be characterized by taking consecutive Lie derivatives of the output until the input appears

$$\begin{aligned} y &= h(x) \\ \dot{y} &= L_f h(x) \\ &\vdots \\ y^{(\gamma-1)} &= L_f^{\gamma-1} h(x) \\ y^{(\gamma)} &= L_f^{\gamma} h(x) + L_g L_f^{\gamma-1} h(x) u \end{aligned} \tag{5.5}$$

where $\gamma \leq n$ is the system relative degree. Since M is smooth and connected, it is always possible to find a diffeomorphism, $\Pi : x \mapsto (\xi, \eta)$, representing the system in

a cascaded canonical form as

$$\begin{aligned}
\dot{\xi}_1 &= \xi_2 \\
\dot{\xi}_2 &= \xi_3 \\
&\vdots \qquad (5.6) \\
\dot{\xi}_{\gamma-1} &= \xi_\gamma \\
\dot{\xi}_\gamma &= \rho(\xi) + \beta(\xi)u \\
\dot{\eta} &= q(\xi, \eta) \qquad (5.7)
\end{aligned}$$

where $\xi_1 = h(x)$. The system represented as (5.6)-(5.7) is said to be in *normal form* [34] and the $n - \gamma$ equations (5.7) are the system internal dynamics. A system satisfying Theorem 5.1 guarantees the existence of an output which renders the system relative degree $\gamma = n$. Normally, the control input

$$u = -\frac{L_f^\gamma h(x) - v}{L_g L_f^{\gamma-1} h(x)} \tag{5.8}$$

will result in $y^{(\gamma)} = v$ and is sufficient to yield linear, stable input/output error tracking of a reference, y_r, if v induces a Hurwitz polynomial,

$$v = y_r^{(\gamma)} + a_{\gamma-1}(y_r^{\gamma-1} - y^{\gamma-1}) + \cdots + a_0(y_r - y).$$

However, if there exists a submanifold $M_s \subset M$ where

$$M_s = \{x \in M \mid L_g L_f^{\gamma-1} h(x) = 0\}$$

then an input singular condition exists in the control law (5.8), the relative degree becomes undefined, and exact input/output linearization is not achievable. This condition can be overcome by approximating the output and corresponding derivatives on the singular submanifold, M_s [15]. In the following study, it is assumed that there exists a singular point $\{x_s \in M_s \mid x_s = L_g L_f^{\gamma-1} h(x_s) = 0\}$. If this is not the case, the system can be transformed to a new set of coordinates through an appropriate

diffeomorphism. Consider a set of $\mathcal{C}^\infty$ functions $\alpha_k(x)$ and $\beta_k(x),\ k = 1, \ldots, \gamma$ where

$$h(x) = \alpha_1(x) + \beta_0(x, u) \tag{5.9}$$

and $\beta_0(x, u)$ is $O(x, u)^2$. Differentiating $\alpha_1(x)$ along system trajectories gives

$$\dot{\alpha}_1(x) = L_f\alpha_1(x) + L_g\alpha_1(x)u \tag{5.10}$$

If $L_g\alpha_1(x)$ is $O(x)^m, m \geq 1$, the term is small in a neighborhood of x_s relative to other system terms and can be neglected. Choosing $\alpha_2(x)$ such that

$$L_{f+gu}\alpha_1(x) = \alpha_2(x) + \beta_1(x, u) \tag{5.11}$$

where $\beta_1(x, u)$ is $O(x, u)^2$ results in a similar analysis. Continuing the procedure until the control term $L_g\alpha_\gamma(x)$ is $O(x)^1$ results in

$$L_{f+gu}\alpha_\gamma(x) = b(x) + a(x)u + \beta_\gamma(x) \tag{5.12}$$

where $a(x)$ is $O(x)^1$ and an approximate input/output map with relative degree γ is achieved.

Definition 5.7 (Robust relative degree) *A nonlinear system* (5.1) *has a robust relative degree, γ, if there exist smooth functions $\alpha_k(x),\ k = 1, \ldots, \gamma$ such that*

$$\begin{aligned} h(x) &= \alpha_1(x) + \beta_0(x, u) \\ L_{f+gu}\alpha_k(x) &= \alpha_{k+1}(x) + \beta_k(x, u), \quad k = 1, \ldots, \gamma - 1 \\ L_{f+gu}\alpha_\gamma(x) &= b(x) + a(x)u + \beta_\gamma(x) \end{aligned} \tag{5.13}$$

where the functions $\beta_k(x, u),\ k = 0, \ldots, \gamma$ are $O(x, u)^2$ and $a(x)$ is $O(x)^1$.

The neglected functions, $\beta_k(x, u)$, are $O(x, u)^2$ in a neighborhood of the origin. The approximation can be extended to larger regions if the functions further satisfy Definition 5.2.

Theorem 5.2 [15] *Consider the dynamics* (5.1) *defined on* M *and that there exists a singular submanifold* $M_s \subset M$. *Let* U_ϵ *be a neighborhood of some* $x_s \in M_s$ *centered at the origin and suppose that*

- *the zero dynamics of the approximate system,* $\dot{\eta} = q(0, \eta)$, *are exponentially stable and* q *is Lipschitz in* ξ *and* η.
- *the functions* $\beta_k(x, u)$ *are uniformly higher order on* $U_\epsilon \times B_\sigma$.

Then for sufficiently small ϵ *and for desired trajectories with sufficiently small values, the state of the closed loop system with control law*

$$u = \frac{-b(x) + v}{a(x)}$$

will remain bounded and the tracking error will be $O(\epsilon)$.

Stability is only guaranteed, however, within some operating range U_ϵ and when the neglected β_k terms become large outside U_ϵ, unbounded errors and instability can occur. Solutions developed in [17, 18] expand the operating range by using approximate tracking near M_s and switching to the exact law prior to departing U_ϵ.

5.3 The Ball and Beam System

Many of the proposed solutions pertaining to input singularities are developed using the classic ball and beam system (BBS) as a demonstrative platform. The BBS consists of a beam free to rotate in a vertical plane by applying a torque at the center of rotation and a ball free to roll along the length of the beam (Fig 5.1). It is required that the ball remain in contact with the beam and roll without slippage. The control objective is to apply a torque input to the beam such that the ball tracks a given reference trajectory. Let the moment of inertia of the beam be J_m, the mass and moment of inertia of the ball be m and J_l, respectively, the radius of the ball be r_l, and the acceleration of gravity be G. Choosing the beam angle θ and the ball

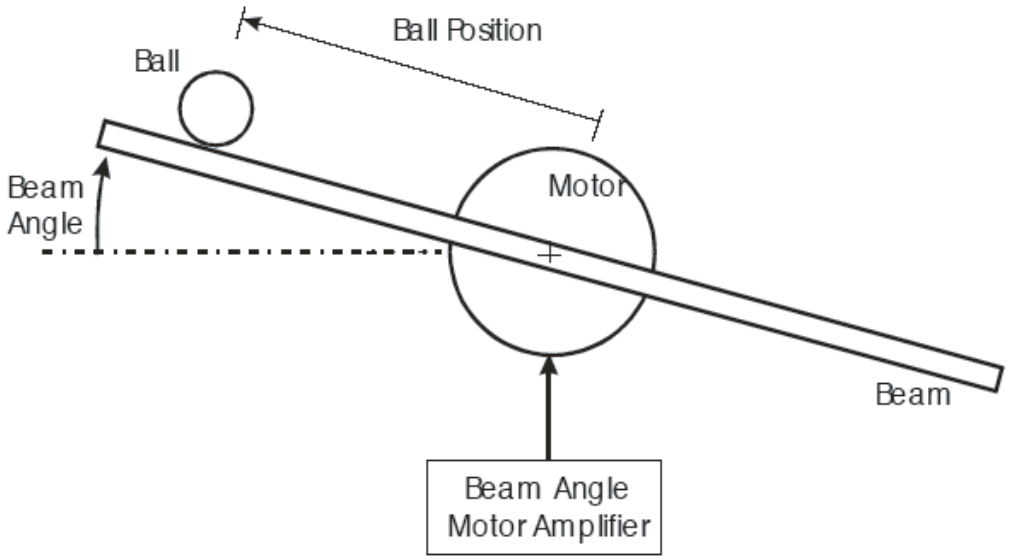

Figure 5.1: Ball and beam system.

displacement r as position coordinates for the system, the equations of motion are given by

$$\left(\frac{J_l}{r_l^2} + m\right)\ddot{r} + mG\sin\theta - mr\dot{\theta}^2 = 0 \tag{5.14}$$

$$(mr^2 + J_m + J_l)\ddot{\theta} + 2mr\dot{r}\dot{\theta} + mGr\cos\theta = \tau \tag{5.15}$$

where τ is the torque applied to the beam. For simplicity, the cumulative inertia term is assigned

$$\frac{m}{\frac{J_l}{r_l^2} + m} = 1$$

Additionally, representing the coordinates of the input space using the nonlinear transformation

$$\tau = (mr^2 + J_m + J_l)\,u + 2mr\dot{r}\dot{\theta} + mGr\cos\theta \tag{5.16}$$

results in a new input, u. Defining the system in local physical coordinates $[r\ \dot{r}\ \theta\ \dot{\theta}]^T = [x_1\ x_2\ x_3\ x_4]^T$, the system can be written in state-space form as

$$\begin{aligned} \dot{x}_1 &= x_2 \\ \dot{x}_2 &= x_1 x_4^2 - G \sin x_3 \\ \dot{x}_3 &= x_4 \\ \dot{x}_4 &= u \\ y &= x_1 \end{aligned} \tag{5.17}$$

Following the usual input/output linearization procedure (5.5), the output, $y = x_1$, is differentiated until the input appears

$$\begin{aligned} y &= x_1 \\ \dot{y} &= x_2 \\ \ddot{y} &= x_1 x_4^2 - G \sin x_3 \\ \dddot{y} &= \underbrace{x_2 x_4^2 - x_4 \cos x_3}_{b(x)} + \underbrace{2 x_1 x_4}_{a(x)} u \end{aligned} \tag{5.18}$$

If $a(x)$ is nonzero in the region of interest, then the system relative degree is three and the control law

$$u = \frac{-b(x) + v}{a(x)} \tag{5.19}$$

will yield a linear input/output relationship described by $\dddot{y} = v$. However, the control coefficient, $a(x)$, is zero whenever the beam angular velocity, $x_4 = \dot{\theta}$, or ball position, $x_1 = r$, are zero creating a singular condition in the control input and defining a singular submanifold, $M_s := \{x \in \mathbb{R}^4 \mid x_1 x_4 = 0\}$. Further analysis of (5.18) also reveals a relative degree that becomes undefined for all $x \in M_s$.

Linearization of (5.17) about $x_s^T = [x_1\ x_2\ x_3\ x_4]^T = [0\ 0\ 0\ 0]^T$ gives

$$\dot{x} = Ax + Bu \tag{5.20}$$

where

$$A = \begin{bmatrix} 0 & 1 & 0 & 0 \\ 0 & 0 & 1 & 0 \\ 0 & 0 & 0 & 1 \\ 0 & 0 & 0 & 0 \end{bmatrix} \quad B = \begin{bmatrix} 0 \\ 0 \\ 0 \\ 1 \end{bmatrix} \tag{5.21}$$

It can be readily determined that the *linear* controllability matrix,

$$\mathcal{C}_l = [B \mid AB \mid A^2B \mid A^3B]$$

is full rank thereby implying $R_T^V(x_s) \neq \emptyset$ for the *nonlinear* system [36]. Therefore, any nonzero control input (torque) will produce a nonzero beam angular velocity ($\dot{\theta} \neq 0$), setting the ball in motion to produce a new ball position ($r \neq 0$) in a neighborhood of the singular point.

Consider constructing an approximate system using the technique of Section 5.2. A nonlinear change of coordinates letting $\xi_1 = \alpha_1(x) = x_1$ and choosing $\alpha_i(\cdot)$ at each step gives

$$\begin{aligned}
\dot{\xi}_1 &= \underbrace{x_2}_{\xi_2=\alpha_2(x)} & \dot{\xi}_1 &= \xi_2 \\
\dot{\xi}_2 &= \underbrace{-G\sin x_3 + x_1 x_4^2}_{\xi_3=\alpha_3(x)} & \dot{\xi}_2 &= \xi_3 \\
\dot{\xi}_3 &= \underbrace{-Gx_4\cos x_3 + x_2 x_4^2}_{\xi_4=\alpha_4(x)} + \underbrace{2x_1 x_4\ u}_{\beta_3(x,u)} & \dot{\xi}_3 &= \xi_4 + \beta_3(x,u) \\
\dot{\xi}_4 &= \underbrace{x_1 x_4^2}_{b(x)} - \underbrace{(G\cos x_3 - 2x_2 x_4)}_{a(x)}\, u & \dot{\xi}_4 &= b(x) + a(x)u
\end{aligned} \tag{5.22}$$

where the term $\beta_3(x,u)$ is neglected. By Definition 5.7, the system has robust relative degree $\gamma = 4$. The control law (5.19) can now be used to linearize the *approximate* system (5.22) and, by Theorem 5.2, maneuver the ball through the singular manifold, M_s, with bounded tracking error.

5.4 The Disk Drive Commutational L/UL Actuator

Using results from Chapter 4, the dynamics of the CRL actuator in local physical coordinates $x_1 = \theta$, $x_2 = \dot{\theta}$, $x_3 = i$, and $u = V_s$ gives the third-order state space representation

$$\begin{aligned} \dot{x}_1 &= x_2 \\ \dot{x}_2 &= \frac{1}{J}[K_t(x_1)x_3 - T_b(x_1) - T_f \,\mathrm{sat}(x_2)] \\ \dot{x}_3 &= \frac{1}{L}[-K_t(x_1)x_2 - Rx_3 + u] \end{aligned} \tag{5.23}$$

defined on M. For the purpose of analysis, consider $T_b(x_1) = T_f = 0,\ \forall\, x \in M$ such that

$$\begin{aligned} \dot{x}_1 &= x_2 \\ \dot{x}_2 &= K_t(x_1)x_3 \\ \dot{x}_3 &= -K_t(x_1)x_2 - x_3 + u \end{aligned} \tag{5.24}$$

where inertia, resistance, and inductance all take values of unity. The drift and input vector fields in (5.1) take the form

$$f(x) = \begin{bmatrix} x_2 \\ K_t(x_1)x_3 \\ -K_t(x_1)x_2 - x_3 \end{bmatrix}, \quad g(x) = \begin{bmatrix} 0 \\ 0 \\ 1 \end{bmatrix} \tag{5.25}$$

With output, $y = x_2$, the input/output relationship is

$$\begin{aligned} y &= x_2 \\ \dot{y} &= K_t(x_1)x_3 \\ \ddot{y} &= \underbrace{\frac{\partial K_t}{\partial x_1}x_2x_3 - K_t^2(x_1)x_2 - K_t(x_1)x_3}_{b(x)} + \underbrace{K_t(x_1)}_{a(x)}u \end{aligned}$$

If $K_t(x_1)$ is nonzero in the region of interest, then the system has relative degree $\gamma = 2$ and the control law (5.19) can be used to provide a linear input/output relationship.

However, if there exists some $\{x \in M \mid K_t(x_1) = 0\}$, then a singular condition exists along with an undefined relative degree. An approximate system using the method of Section 5.2 with diffeomorphism $\Pi : x \mapsto (\xi, \eta)$ where $\xi_1 = \alpha_1(x) = x_2$ gives

$$\begin{aligned}
\dot{\xi}_1 &= \underbrace{K_t(x_1)x_3}_{\xi_2=\alpha_2(x)} \\
\dot{\xi}_2 &= \underbrace{\frac{\partial K_t}{\partial x_1}x_2x_3 - K_t^2(x_1)x_2 - K_t(x_1)x_3}_{\xi_3=\alpha_3(x)} + \underbrace{K_t(x_1)u}_{\beta_2(x)} \\
\dot{\xi}_3 &= K_t^2(x_1)x_2 - 3\frac{\partial K_t}{\partial x_1}K_t(x_1)x_2^2 \\
&\quad + \left[\frac{\partial^2 K_t}{\partial x_1^2}x_2^2 + \frac{\partial K_t}{\partial x_1}K_t(x_1)x_3 - 2\frac{\partial K_t}{\partial x_1}x_2 - K_t^3(x_1) + K_t(x_1)\right]x_3 \\
&\quad - \left[\frac{\partial K_t}{\partial x_1}x_2 + K_t(x_1)\right]u \\
&\vdots \\
\dot{\xi}_k &= \alpha_{k+1}(K_t(x_1), x_2, x_3) + \beta_k(x, u) \\
\dot{\eta} &= x_1
\end{aligned} \tag{5.26}$$

Analysis of (5.26) reveals that all terms with x_3 and u are products with K_t and x_2 defining a singular submanifold

$$M_s := \left\{ x \in M \;\middle|\; \frac{\partial K_t}{\partial x_1}x_2 = K_t(x_1) \right\}$$

Therefore, the CRL system also fails to have a robust relative degree. It is of interest to determine the reachable set from the singular manifold. Even if exact input/output linearization cannot be achieved from M_s, the potential of reaching other states may exist as in the ball and beam example. Without loss of generality, assume for the *exact* system, $K_t(0) = 0$ and the equilibrium point $x_c^T = [0\ 0\ 0] \in M_s$. Consider the controllability subalgebra, $\mathcal{C}$, at x_c on M_s formed by taking successive Lie brackets of f and g on M_s

$$ad_f g = [f, g] = \frac{\partial g}{\partial x}f - \frac{\partial f}{\partial x}g \tag{5.27}$$

where

$$f(x_c) = \begin{bmatrix} 0 \\ 0 \\ 0 \end{bmatrix} \quad \frac{\partial f}{\partial x}(x_c) = \begin{bmatrix} 0 & 1 & 0 \\ 0 & 0 & 0 \\ 0 & 0 & -1 \end{bmatrix} \quad g(x_c) = \begin{bmatrix} 0 \\ 0 \\ 1 \end{bmatrix} \quad \frac{\partial g}{\partial x}(x_c) = [\mathbf{0}] \tag{5.28}$$

Repeated Lie brackets take the form

$$ad_f^k g = -\frac{\partial f}{\partial x}(x_c)\, ad_f^{(k-1)}, \quad k = 0, 1, 2, \ldots \tag{5.29}$$

resulting in

$$\mathcal{C}(x_c) = \begin{bmatrix} 0 & \cdots \\ 0 & \cdots \\ (-1)^k & \cdots \end{bmatrix}, \quad k = 0, 1, 2, \ldots \tag{5.30}$$

Therefore, the controllability distribution $\Delta_{\mathcal{C}}(x_c) = \text{span}\{\mathcal{C}(x_c)\}$ has dimension $\dim \Delta_{\mathcal{C}}(x_c) = 1$ and the system is not locally reachable at x_c. Furthermore, there exists no output resulting in a relative degree $\gamma = 3$ system on x_c. However, Lemma 5.1 suggests that $R_T^V(x_c)$ is non-empty and that some portion of the system can continue to be manipulated with control input leading to the following theorem

Theorem 5.3 *Consider the CRL system with dynamics* (5.24) *and controllability distribution* $\Delta_{\mathcal{C}}(x_c)$ *where* $\dim \Delta_{\mathcal{C}}(x_c) = 1 < 3$. *There exists a neighborhood* U *of* x_c *and constant* p_2 *such that the submanifold*

$$S_{x_c} := \{x \in M_s \mid x_1 = 0, x_2 = p_2\}$$

is an integral manifold of $\Delta_{\mathcal{C}}(x_c)$ *Then for any neighborhood* U *of* x_c *and for all* $T > 0$, $R_T^V(x_c)$ *is contained in* S_{x_c}. *Furthermore,* $R_T^V(x_c)$ *contains a non-empty open set of the integral manifold* S_{x_c}. *Hence the system restricted to* S_{x_c} *is locally reachable.*

Proof. Since $f(x) + g(x)u \in \mathcal{C}$ for any u and $x \in M$, the system (5.24) for x_c can be restricted to S_{x_c} which, by Lemma 5.1, is an integral manifold of

$$\dim\{S_{x_c}\} = \dim\{\Delta_{\mathcal{C}}(x_c)\}.$$

The existence of a non-empty $R_T^V(x_c)$ follows from Theorem 5.1. ■

The submanifold S_{x_c} is a leaf of the foliation generated by parameterizing all admissible values of angular velocity according to $x_2 = p_2$ for each constant p_2. Theorem 5.3 can be applied to each foliation leaf resulting in a velocity independent reachable set. The reachable set in this case is the set of all admissible values of current with dynamics described by

$$\dot{x}_3 = -K_t(x_1)x_2 - x_3 + u \tag{5.31}$$

and the point $x_c \in M_c$ is defined as an *uncontrollable, input singularity* or a "critical point" where $M_c := \{x \in M_s \mid \dim \Delta_{\mathcal{C}}(x_c) < n\}$.

This phenomena may be further investigated by revisiting the BBS without the influence of gravity ($G = 0$). Mathematically, the system of (5.17) now becomes

$$\begin{aligned} \dot{x}_1 &= x_2 \\ \dot{x}_2 &= x_1 x_4^2 \\ \dot{x}_3 &= x_4 \\ \dot{x}_4 &= u \end{aligned} \tag{5.32}$$

and continues to exhibit an undefined relative degree. Following the system approximation construction procedure as in (5.22) gives

$$
\begin{aligned}
\dot{\xi}_1 &= \underbrace{x_2}_{\xi_2=\alpha_2(x)} \\
\dot{\xi}_2 &= \underbrace{x_1 x_4^2}_{\xi_3=\alpha_3(x)} \\
\dot{\xi}_3 &= \underbrace{x_2 x_4^2}_{\xi_4=\alpha_4(x)} + \underbrace{2x_1 x_4\, u}_{\beta_3(x,u)} \\
\dot{\xi}_4 &= \underbrace{x_1 x_4^3}_{\xi_4=\alpha_4(x)} + \underbrace{2x_2 x_4\, u}_{\beta_4(x,u)} \\
&\vdots \\
\dot{\xi}_k &= \alpha_{k+1}(x_1, x_2, x_4) + \beta_k(x_1, x_2, x_4)u
\end{aligned}
\tag{5.33}
$$

where all terms with u are products of x_4. Therefore, without gravity, the BBS also fails to possess a robust relative degree. Furthermore, the absence of gravity alters controllability about the singular point. Reevaluation of the system controllability at $x_c^T = [x_1 \;\; x_2 \;\; x_3 \;\; x_4]^T = [0 \;\; 0 \;\; 0 \;\; 0]^T$ with the new dynamics of (5.33) gives the controllability subalgebra

$$
\mathcal{C}(x_c) = [ad_f^0 g \mid ad_f g] = \begin{bmatrix} 0 & 0 \\ 0 & 0 \\ 0 & -1 \\ 1 & 0 \end{bmatrix}, \quad ad_f^k g = [\mathbf{0}]\,,\ \forall\, k > 1 \tag{5.34}
$$

where

$$
f(x_c) = \begin{bmatrix} 0 \\ 0 \\ 0 \\ 0 \end{bmatrix} \quad \frac{\partial f}{\partial x}(x_c) = \begin{bmatrix} 0 & 1 & 0 & 0 \\ 0 & 0 & 0 & 0 \\ 0 & 0 & 0 & 1 \\ 0 & 0 & 0 & 0 \end{bmatrix} \quad g(x_c) = \begin{bmatrix} 0 \\ 0 \\ 0 \\ 1 \end{bmatrix} \quad \frac{\partial g}{\partial x}(x_c) = [\mathbf{0}]
$$

So the controllability distribution $\Delta_{\mathcal{C}}(x_c) = \text{span}\{\mathcal{C}(x_c)\}$, has dimension $\dim \Delta_{\mathcal{C}}(x_c) = 2 < 4$, and the system is, therefore, not locally reachable from x_c on M.

From a physical perspective, radial motion $(r, \dot{r})$ of the ball cannot be induced by a nonzero angular position of the beam. Without gravity, there is no reachable state in ball position or velocity from x_c resulting from an applied torque to the beam. Values of beam angular position and velocity remain reachable, however, and a result similar to Theorem 5.3 implies the existence of a foliation parameterized by all admissible values of beam angular position, p_3. Therefore, a non-empty $R_T^V(x_c) \subset S_{x_c}$ exists where the submanifold

$$S_{x_c} := \{x \in M \mid x_1 = 0, x_3 = p_3\}$$

constitutes a leaf of the foliation for each fixed constant, p_3.

Introduction of a bias term in the CRL system designed using the guidelines of Section 4.1.3 alters the drift vector field. For simplicity, it is assumed that the constant and first-order coefficient terms of the bias polynomial estimate are $c_0 = c_1 = 1$. The drift vector field at $x_s^T = [0\ 0\ 0]$ now becomes

$$f(x_s) = \begin{bmatrix} 0 \\ -1 \\ 0 \end{bmatrix} \qquad \frac{\partial f}{\partial x}(x_s) = \begin{bmatrix} 0 & 1 & 0 \\ -1 & 0 & 0 \\ 0 & 0 & -1 \end{bmatrix} \tag{5.35}$$

The controllability subalgebra remains unchanged and, therefore, the bias offers no assistance in defining a relative degree. However, the bias does change the equilibrium state of the system. The next section details the CRL system equilibrium analysis and gives a sufficient condition for maneuvering through the uncontrollable singularity.

5.5 Commutational Ramp Load Actuator Dynamic Analysis

Based on the modeling development in Chapter 4, the actuator static and dynamic behavior on the ramp is investigated. This section establishes equilibria existing within the ramp angle and defines conditions at which they occur. A sufficient condition ensuring actuator motion through the equilibria and critical point x_c is given. There exists two *forced* equilibrium points, x_{eq-} and x_{eq+}, depending on the location of the actuator arm relative to the critical angle, x_{1c}. Evaluating the left side of equation (5.23) to zero, the equilibrium points are shown to occur when

$$K_t(x_{1eq})u_{sat} - R\,T_b(x_{1eq}) = 0 \tag{5.36}$$

where u_{sat} is the saturation voltage for the system. Knowing $K_t(x_1)$ and $T_b(x_1)$, the equilibrium points can be determined as a function of u_{sat} and the coil resistance where $x_{1eq-} < x_{1c} < x_{1eq+}$. Consider $U_c \subset M$ containing M_c such that

$$U_c := \{x \in M \mid x_{1eq-} < x_1 < x_{1eq+}\}$$

Four possibilities exist corresponding to the dynamics of equation (5.23) when maneuvering through U_c with and without input commutation. Two input voltage levels, $\pm u_{sat}$ are used along with the design parameters developed in Section 4.4 to demonstrate each case. Using equation (5.36) along with the bias and torque factor polynomial expressions of (4.9) with coefficients from Table 4.7, the two equilibrium points were computed at 0.1360 rad and 0.1534 rad for x_{1eq-} and x_{1eq+}, respectively. The critical angle $x_{1c} = 0.1449$ rad lies between the two equilibrium points. The following four cases reflect the possible scenarios for an attempted ramp load maneuver with the proposed commutational actuator.

Case 1: No commutation ($u = -u_{sat}$) The actuator initially moves away from the OCS through x_{1c}, but is forced back toward the OCS when $x_1 > x_{1c}$. The cycle continues and a stable focus results about x_{1eq-} as shown in Figure 5.2.

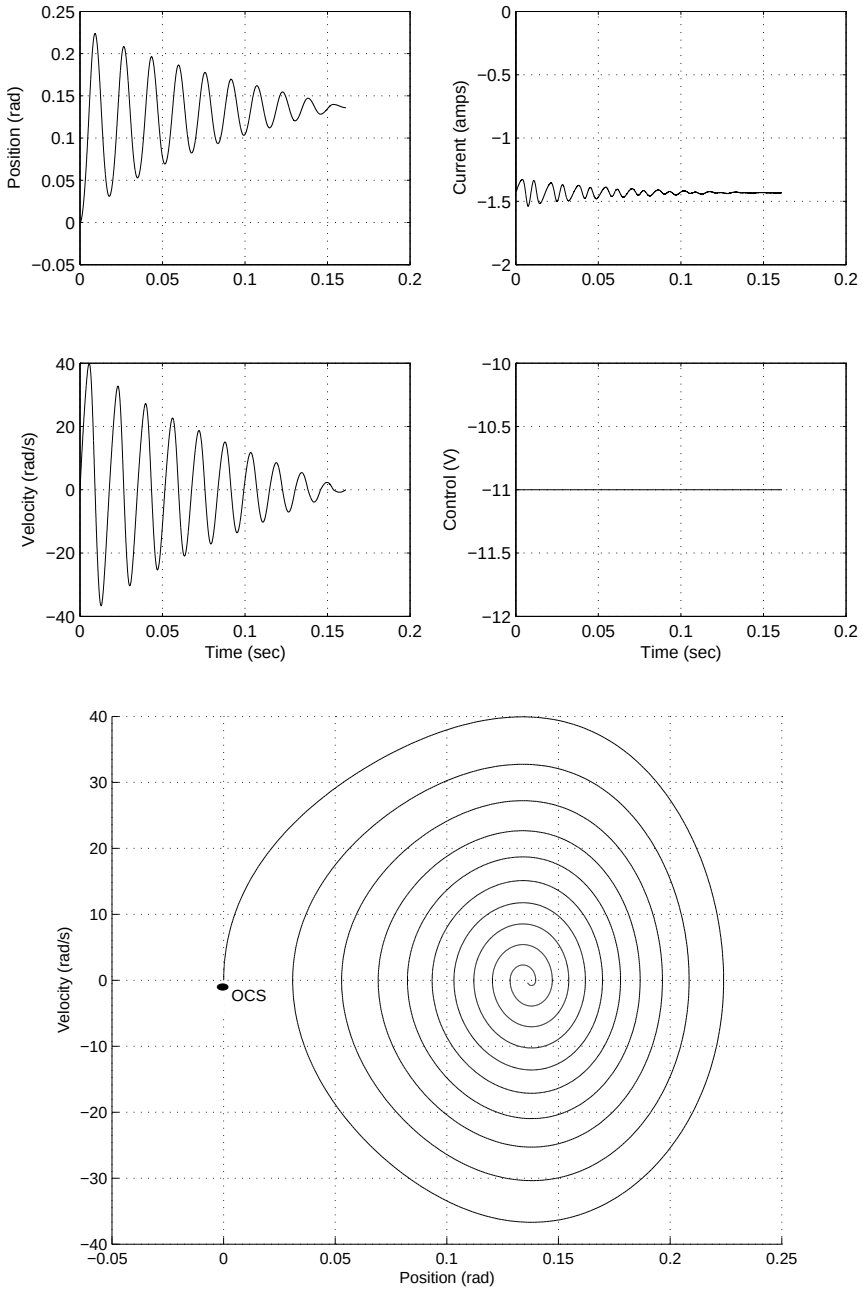

Figure 5.2: Actuator ramp dynamic characteristics without commutation

The remaining three scenarios occur when the input voltage switches polarity $u = -u_{sat},\ 0 \leq t < t_s$ or $u = u_{sat},\ t \geq t_s$ at some switching time, t_s.

Case 2: The actuator initially moves away from the OCS. The input voltage reverses polarity at $t_s = 3.5$ msec at an angle $x_1(t_s) < x_{1eq+}$. There is not enough initial velocity to reach x_{1eq+} and the actuator returns to the OCS (Fig. 5.3).

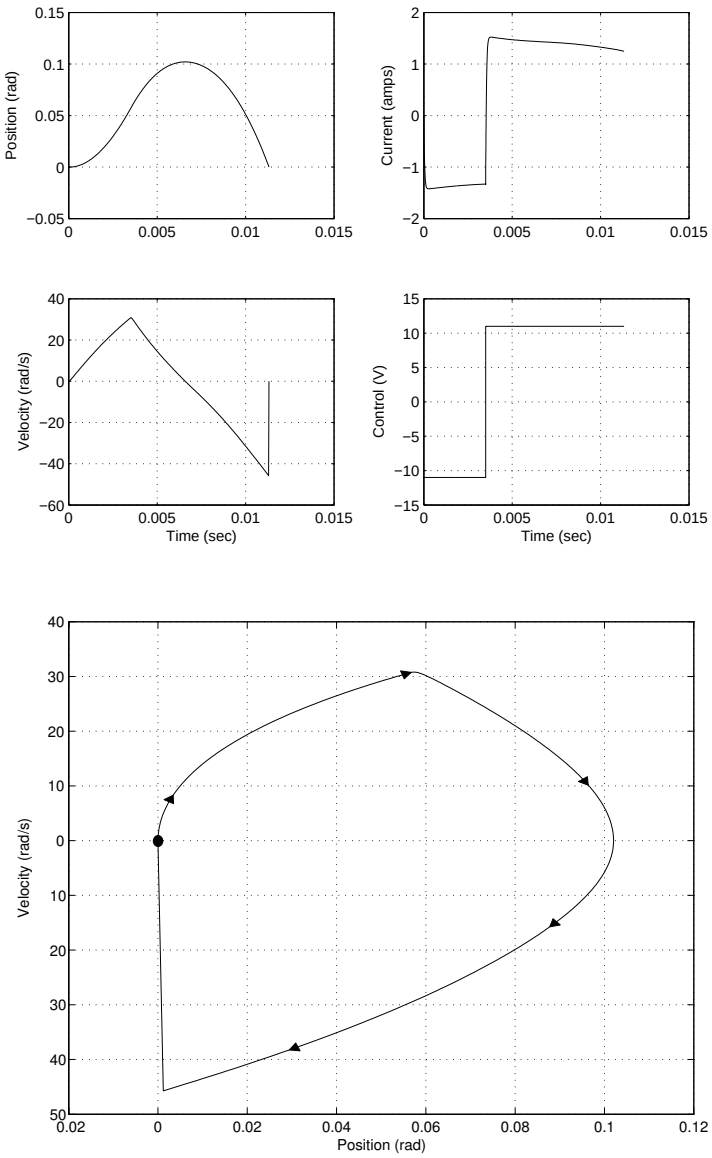

Figure 5.3: Dynamic characteristics with commutation. Actuator forced back to OCS

Case 3: Similar to Case 2, but $t_s = 3.929$ msec occurs later than Case 2 where there is just enough initial velocity such that $x_2 = 0$ at x_{1eq+}. As shown in Figure 5.4, the actuator rests at x_{1eq+}.

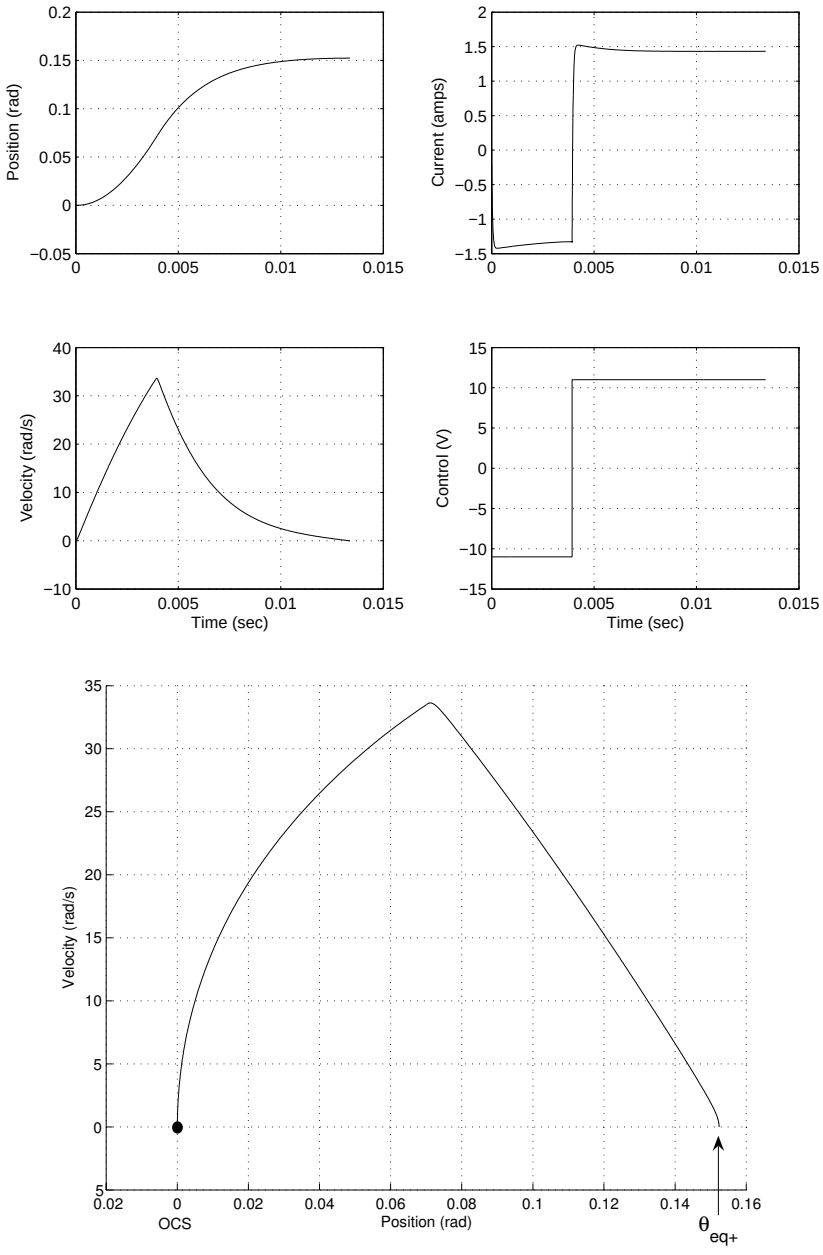

Figure 5.4: Dynamic characteristics with commutation. Actuator rests at x_{1eq+}

Case 4: The input polarity reversal occurs at $t_s = 6.0$ msec such that $x_2 > 0$ at x_{1eq+} and the actuator moves through x_{1eq+} and loads the heads onto the disk

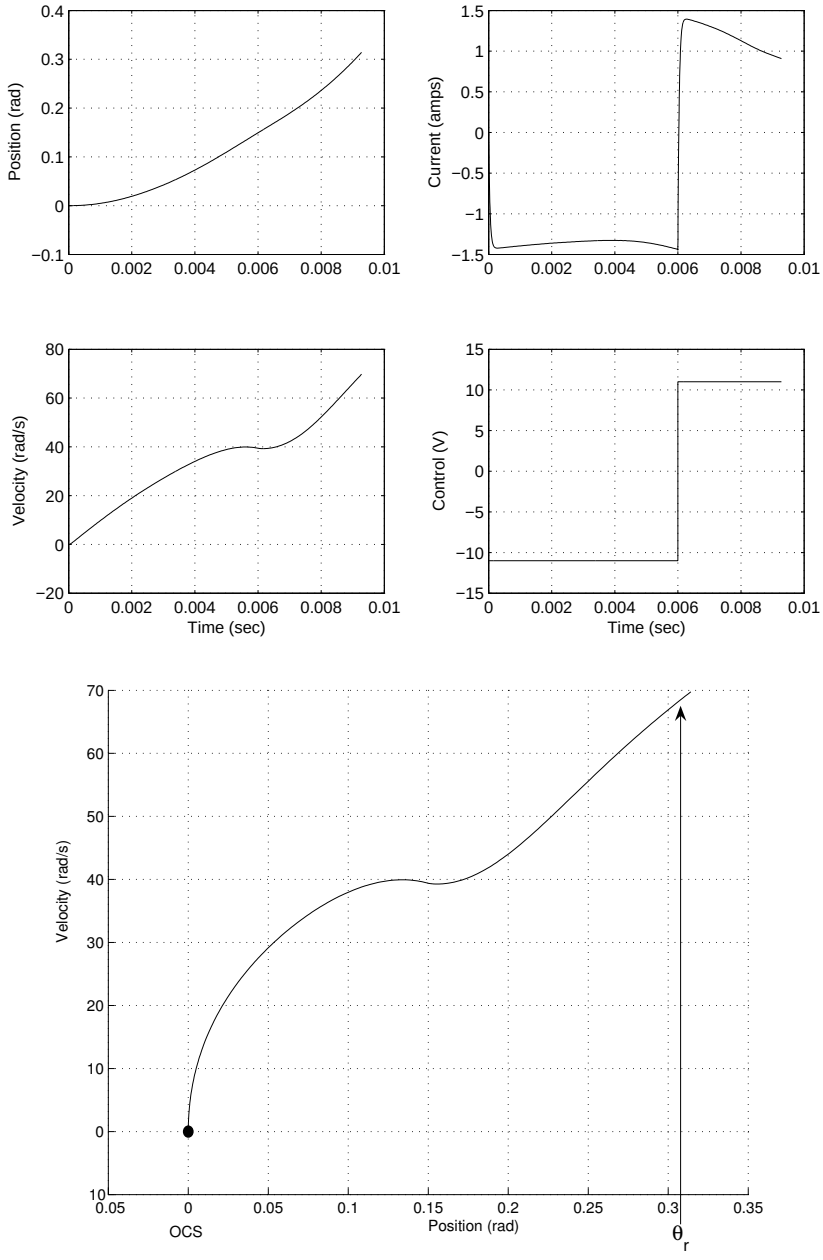

Figure 5.5: Dynamic characteristics with commutation. Actuator loads onto disks

The latter three cases suggest that there exists a minimum, critical angular velocity, x_{2c}, such that if the actuator reaches x_{2c} prior to reaching, U_c, it can successfully pass through U_c to some $\{x \in M \mid x_1 > x_{1eq+}\}$. Transform the CRL system to a new set of local physical coordinates $z = [\theta\ \omega\ \alpha]$ on M through the diffeomorphism $\Pi : x \mapsto z$

$$\begin{aligned} \theta &= x_1 \\ \omega &= x_2 \\ \alpha &= \frac{1}{J}[K_t(x_1)x_3 - T_b(x_1) - T_f] \end{aligned} \tag{5.37}$$

where θ, ω, α are the angular position, velocity, and acceleration, respectively, defined as

$$\omega = \frac{d\theta}{dt}, \quad \alpha = \frac{d\omega}{dt} \tag{5.38}$$

The equations in (5.38) can be rewritten to establish a time independent relationship between angular velocity and acceleration

$$\omega \frac{d\omega}{d\theta} = \alpha(\theta) \quad \text{or} \quad \omega\, d\omega = \alpha(\theta)\, d\theta \tag{5.39}$$

Integrating both sides of (5.39) and noting the expression for angular acceleration from (5.37) gives

$$\begin{aligned} \frac{1}{2}\left[\omega^2(\theta_{eq+}, i) - \omega_c^2(\theta_o, i)\right] &= \int_{\theta_o}^{\theta_{eq+}} \alpha(\zeta)\, d\zeta \\ \omega^2(\theta_{eq+}, i) - \omega_c^2(\theta_o, i) &= \frac{2}{J}\left\{\int_{\theta_o}^{\theta_{eq+}} [K_t(\zeta)i - T_b(\zeta) - T_f]\, d\zeta\right\} \end{aligned}$$

where $\omega_c(\theta_o, i)$ is the actuator initial velocity at some $\theta_o < \theta_{eq+}$. If

$$\omega_c^2(\theta_o, i) = \left|\frac{2}{J}\left\{\int_{\theta_o}^{\theta_{eq+}} [K_t(\zeta)i - T_b(\zeta)]\, d\zeta - T_f(\theta_{eq+} - \theta_o)\right\}\right|, \quad \forall\, z \in U_c$$

then $\omega^2(\theta_{eq+}, i) \geq 0$ and the actuator will either pass through or rest at θ_{eq+}, respectively. If

$$\omega_c^2(\theta_o, i) > \left|\frac{2}{J}\left\{\int_{\theta_o}^{\theta_{eq+}} [K_t(\zeta)i - T_b(\zeta)]\, d\zeta - T_f(\theta_{eq+} - \theta_o)\right\}\right|, \quad \forall\, z \in U_c \tag{5.40}$$

then $\omega^2(\theta_{eq+}, i) > 0$ and the actuator will pass through θ_{eq+} for all $z \in U_c$. Therefore, knowing the design tolerances, an upper bound on the right side of (5.40) can be determined resulting in an input that guarantees (5.40) is satisfied. The above example for the CRL system leads to a general formulation for a class of systems defined on uncontrollable, singular manifolds.

Theorem 5.4 *Consider the nonlinear system* (5.1) *defined on a smooth, connected, n-dimensional manifold M represented in the normal form as*

$$\begin{aligned} \dot{\xi}_1 &= \xi_2 \\ \dot{\xi}_2 &= \xi_3 \\ &\vdots \\ \dot{\xi}_{k-1} &= \xi_k \\ \dot{\xi}_k &= \xi_{k+1} \\ \dot{\xi}_{k+1} &= \rho(\xi) + \beta(\xi)u \\ \dot{\eta} &= q(\xi, \eta) \end{aligned} \tag{5.41}$$

where $2 \leq k \leq (n-1)$. *Let* U_c *be an open neighborhood of a critical point* $\xi_c \in M_c$ *where*

$$M_c := \{\xi \in M \mid \beta(\xi) = 0, \xi_j = 0,\ j = 2, \ldots, k\}$$

and consider the one-dimensional submanifold $\Theta_c \subset U_c$,

$$\Theta_c := \{\xi \in U_c \mid \xi_{k-1} \neq 0,\ \xi_{k-1} \in (a, b)\}$$

where $[a, b]$ *is in the closure of* U_c. *There exists a set*

$$M_\Omega := \left\{ \xi \in M \;\middle|\; \xi_k^2 > \left| 2 \int_a^b \xi_{k+1} d\xi_{k-1} \right|,\ \forall\, \xi \in U_c \right\}$$

such that if the system is driven to M_Ω, *it can successfully pass through* U_c.

Proof. Integration of the time-independent relationship

$$\xi_k d\xi_k = \xi_{k+1} d\xi_{k-1}$$

results in

$$\xi_{kb}^2 - \xi_{ka}^2 = 2\int_{\Theta_c} \xi_{k+1} d\xi_{k-1} = 2\int_a^b \xi_{k+1} d\xi_{k-1}$$

where ξ_{ka} and ξ_{kb} are the values of ξ_k in the submanifold, Θ_c, corresponding to $\xi_{k-1} = a$ and $\xi_{k-1} = b$, respectively. Therefore, if

$$\xi_{ka}^2 > \left| 2\int_a^b \xi_{k+1} d\xi_{k-1} \right|, \quad \forall\, \xi \in U_c$$

then $\xi_{kb}^2 > 0$ and $\dot{\xi}_{k-1} > 0$ for $\xi_{k-1} = b$. Since b is in the boundary set of U_c, the system moves to a point outside of U_c. ■

The sufficient condition of Theorem 5.4 will prove to be a crucial basis for generation of an admissible reference trajectory that can be tracked using closed loop control for a successful ramp load maneuver.

5.6 Summary

This chapter developed the general characteristics of systems possessing controllable and uncontrollable singularities. Terminology and control solutions from current literature are presented for handling singularities along with applications to the classic ball and beam system. A comparison is presented between the ball and beam and commutational ramp load systems. The comparison reveals deficiencies in the existing control solutions when applied to commutational ramp loading with an uncontrollable, singular point. Equilibria existing within the ramp angle are established and conditions at which they occur are defined. A sufficient condition for manuevering through the uncontrollable singularity is given and a general formulation is developed for a class of systems possessing this quality.

CHAPTER 6

DISK DRIVE COMMUTATIONAL RAMP LOAD CONTROL

The contributions of this chapter include the integration and implementation of the commutational ramp load disk drive actuator designed in Chapter 4. Operation of the concept requires an input polarity reversal to maneuver the actuator through an uncontrollable region along the ramp. A trajectory is developed based on the analysis of Chapter 5 to provide a tracking reference and promote motion through the uncontrollable region. A formal procedure is developed to facilitate the trajectory design method. Finally, two controllers are developed to specifically fulfill the tracking requirement. Both controllers compensate for nonlinearities during a ramp load maneuver, but allow for easy transition to a linear controller upon loading and entry into the data zone. Extensive experiments are conducted to verify both design concepts.

A description of the performance requirements and trajectory generation procedure for commutational ramp loading are presented in Section 6.1 and 6.2, respectively. A robust state feedback controller to track the reference trajectory is developed in Section 6.3. To compensate for the absence of position and velocity measurement, an output feedback tracking controller is given in Section 6.4. Simulations and experiments are performed to verify the designs. Section 6.5 summarizes the results.

6.1 Performance Requirements

To protect the disk drive against data loss or catastrophic damage, three primary performance constraints are necessary. As discussed in Chapter 1, the vertical and

Table 6.1: Performance requirements

Parameter	Max Value
Max Loading velocity (ω_l)	5.56 rad/s
Max Head acceleration (α_{max})	20.4 krad/s^2
Max Control output (V)	11 V
Min Sample rate (f_s)	20 kHz

horizontal head loading velocities must be regulated to prevent HDI. Table 4.4 lists these velocities for the ramp load disk drive designed in Chapter 4. Based on the actuator arm pivot to head distance it was determined that a maximum angular loading velocity of $\omega_l \leq 5.56$ rad/s (10 in/s at the head) could be achieved without HDI. Additionally, a linear head acceleration limit exists to prevent damage to the head/suspension interface. The R/W head is attached to a suspension (Fig. 6.1) designed with an inherent acceleration limit to avoid structural damage. The limit for the particular drive under study was 980 m/s^2 (1000 g) corresponding to an angular acceleration $\alpha_{max} = 20.4$ krad/s^2. Finally, it is required that the ramp loading maneuver execute within the 11 V saturation voltage of the amplifier. Table 6.1 summarizes the performance requirements.

6.2 Trajectory Design

Following the analysis of Chapters 4 and 5, the actuator becomes uncontrollable at a critical angle, θ_c. An implementation consideration is that there is actually a neighborhood around θ_c where $K_t(\theta)$ is very small and $V \rightarrow V_{sat}$ during tracking. An angle or zone exists within which the velocity and position states cannot be tracked. Using the results of Chapter 5, a trajectory generation strategy must be developed for successful passage of the actuator through this zone while providing a smooth,

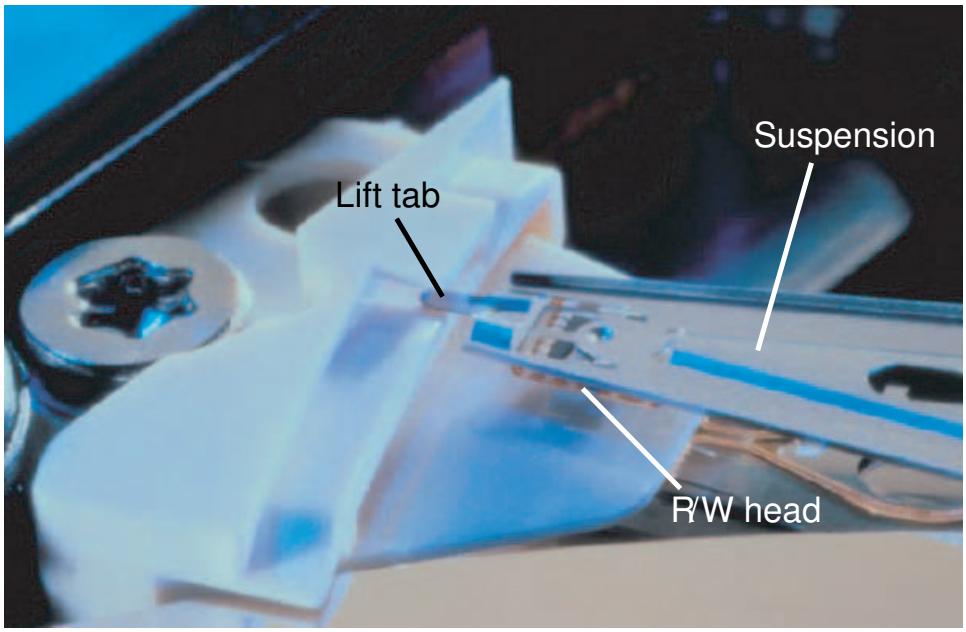

Figure 6.1: Suspension lift tab on ramp

continuous state trajectory. A strategy is proposed that considers the primary constraints of maximum angular loading velocity, ω_l, maximum angular acceleration, α_{max}, and the saturation voltage V_{sat}. It is assumed that $K_t(\theta)$ and $T_b(\theta)$ are known. The loading velocity should be achieved prior to the ramp loading angle, θ_r, but subsequent to θ_c. An angle, $\Delta\theta_c$, is chosen as a design parameter and selected so that θ_c is centered within $\Delta\theta_c$. The strategy requires the trajectory be mapped into three sectors (Fig. 6.2) based on angular position

$$\mathbb{S}_1 := [0, \theta_-]\,;\ \mathbb{S}_2 := [\theta_-, \theta_+]\,;\ \mathbb{S}_3 := [\theta_+, \theta_r] \tag{6.1}$$

where

$$\theta_- = \theta_c - \frac{\Delta\theta_c}{2} \quad \text{and} \quad \theta_+ = \theta_c + \frac{\Delta\theta_c}{2}.$$

Recall from Section 5.5 that the input saturates at the equilibrium points. Therefore, it is desirable that the set $\Theta_c := [\theta_{eq-}, \theta_{eq+}] \subset \mathbb{S}_2$ to guarantee controllability in sectors $\mathbb{S}_1$ and $\mathbb{S}_3$. Ideally, ω_l would be achieved as the actuator exits $\mathbb{S}_2$, minimizing the error in $\mathbb{S}_3$ prior to the actuator departing the ramp and loading onto the disk.

It follows that velocity is constant in $\mathbb{S}_3$ ($\omega_{\mathbb{S}3} = \omega_l$) and position is required to vary linearly according to constant velocity. The current trajectory in $\mathbb{S}_3$ is calculated to sustain $\omega_{\mathbb{S}3}$ based on the acceleration required to overcome the bias and frictional torques

$$i_{\mathbb{S}3} = \frac{T_{fx} + T_b(\theta_{\mathbb{S}3})}{K_t(\theta_{\mathbb{S}3})} \tag{6.2}$$

Since it is known that little or no control effort will be available for controlling the mechanical dynamics within $\Delta\theta_c$ ($\mathbb{S}_2$), Theorem 5.4 can be used to determine the minimum initial angular velocity, $\omega_{\mathbb{S}2o}$, required to overcome magnetic bias and dynamic friction torques for sustained actuator motion. Assuming a linear velocity decay to w_l, this required angular velocity can be estimated from (5.40) as

$$\begin{aligned} \omega_{\mathbb{S}2o} &= \sqrt{\omega_l^2 + \frac{2(T_{bx} + T_{fx} - K_{tx} i)\Delta\theta_c}{J}} \\ &> \sqrt{\left| \frac{2}{J} \left\{ \int_{\theta}^{-\theta_+} \left[K_t(\zeta) i - T_b(\zeta) \right] d\zeta - T_{fx}(\theta_+ - \theta_-) \right\} \right|}, \quad \forall\, \theta \in \mathbb{S}_2 \end{aligned} \tag{6.3}$$

where T_{bx} and K_{tx} are the maximum bias torque and torque factor within $\mathbb{S}_2$, respectively. While inside $\mathbb{S}_2$, linear velocity decay is observed beginning at $\omega_{\mathbb{S}2o}$ and ending at $\omega_{\mathbb{S}2f} = \omega_l$. The initial and final position $\theta_{\mathbb{S}2o} = \theta_-$ and $\theta_{\mathbb{S}2f} = \theta_+$, respectively, correspond to the boundaries of $\mathbb{S}_2$ and the position trajectory within $\mathbb{S}_2$ is parabolic resulting from the linear velocity decay. It follows from Theorem 5.3 that current remains controllable in $\mathbb{S}_2$ at or near the critical angle. Since current has little effect on the actuator dynamics within $\mathbb{S}_2$, it is advantageous to reverse polarity and increase the current to an initial value, $i_{\mathbb{S}3o}$, that will sustain the actuator at the loading velocity, ω_l, upon entering $\mathbb{S}_3$. Therefore, a smooth trajectory is generated from $i_{\mathbb{S}2o} = 0$ to $i_{\mathbb{S}2f} = i_{\mathbb{S}3o}$. Prior to entering $\mathbb{S}_2$, a smooth trajectory can be generated in $\mathbb{S}_1$ with initial and final conditions

$$\theta_{\mathbb{S}1o} = \omega_{\mathbb{S}1o} = \alpha_{\mathbb{S}1o} = 0, \quad \theta_{\mathbb{S}1f} = \theta_-, \quad \omega_{\mathbb{S}1f} = \omega_{\mathbb{S}2o}, \quad \alpha_{\mathbb{S}1f} = -\frac{T_{fx} + T_{bx}}{J} \tag{6.4}$$

The current is computed from the angular acceleration trajectory as

$$i_{\mathbb{S}1} = \frac{J(\alpha_{\mathbb{S}1} - \alpha_{\mathbb{S}1f})}{K_t(\theta_{\mathbb{S}1})} \tag{6.5}$$

Subtraction of $\alpha_{\mathbb{S}1f}$ results in an initial value, $i_{\mathbb{S}1o}$, to immediately compensate for effects of bias and friction. Also, $i_{\mathbb{S}1f} = i_{\mathbb{S}2o} = 0$ to ensure saturation is not reached for small values of $K_t(\theta)$ upon entering $\mathbb{S}_2$. The trajectory generation procedure is summarized in the following five steps:

1. Determine the constraints ω_l, α_{max}, and V_{sat} and select the size of $\Delta\theta_c$.

2. Map the ramp angle into three sectors as indicated in (6.1). The trajectory in $\mathbb{S}_3$ corresponds to sustaining the constant loading velocity $\omega_{\mathbb{S}3} = \omega_l$. Position, $\theta_{\mathbb{S}3}$, increases linearly corresponding to constant velocity and, with measurements of $K_t(\theta)$, $T_b(\theta)$, and T_f, the current trajectory is computed using (6.2).

3. The initial and final conditions, $\theta_{\mathbb{S}2o}$ and $\theta_{\mathbb{S}2f}$, respectively correspond to the boundaries of $\mathbb{S}_2$ in (6.1). The final velocity $\omega_{\mathbb{S}2f} = \omega_{\mathbb{S}3} = \omega_l$ and the initial velocity, $\omega_{\mathbb{S}2o}$, can be determined from (6.3). The velocity profile will decay linearly within $\mathbb{S}_2$ and $\theta_{\mathbb{S}2}$ will be parabolic corresponding to linear velocity. Represent the current trajectory, $i_{\mathbb{S}2}$, as a smooth, continuous function beginning from $i_{\mathbb{S}2o} = 0$ to $i_{\mathbb{S}2f} = i_{\mathbb{S}3o}$.

4. Generate a smooth, continuous trajectory in $\mathbb{S}_1$ corresponding to the initial and final conditions (6.4). The current trajectory, $i_{\mathbb{S}1}$, corresponds to (6.5).

5. Ensure that the constraints are met. If not, adjust $\Delta\theta_c$ and repeat the procedure.

An example trajectory is shown in Figure 6.2.

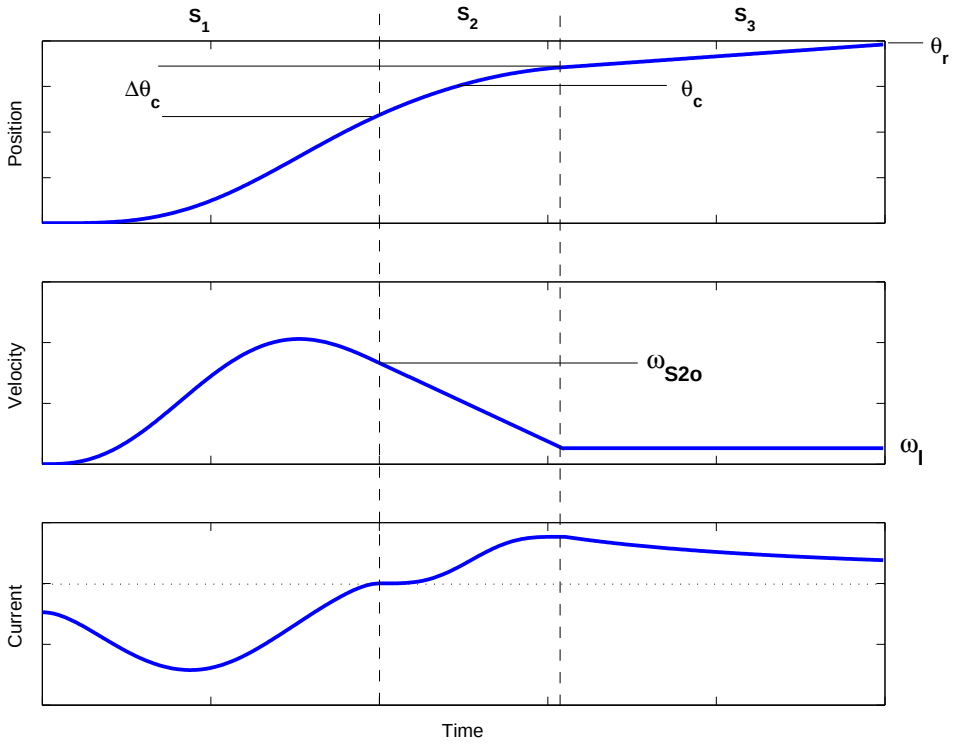

Figure 6.2: Example ramp load trajectory profile

6.3 Robust State-Feedback Control

A method is required to track the trajectory developed in Section 6.2 while adhering to the constraints outlined in Section 6.1. A robust control law is developed that provides stability and compensation for small errors that may exist in association with relative differences in torque factor and bias based on reference and actual position. A variation is also presented that is particularly advantageous for systems that are sample rate limited under low disturbance conditions.

6.3.1 Controller Design

Choosing the states as $x_1 = \theta$, $x_2 = \dot{\theta}$, $x_3 = i$, and the control $u = V_s$ gives the third-order state space representation

$$\begin{aligned} \dot{x}_1 &= x_2 \\ \dot{x}_2 &= \frac{1}{J}[K_t(x_1)x_3 - T_b(x_1) - T_f \,\mathrm{sat}(x_2)] \\ \dot{x}_3 &= \frac{1}{L}[-K_t(x_1)x_2 - Rx_3 + u] \end{aligned} \tag{6.6}$$

The system becomes uncontrollable at θ_c as discussed in Section 6.2. Additionally, the controller must not exceed V_{sat} which can be problematic when $K_t(\theta)$ becomes small. Using the sector mapping introduced in Section 6.2, the controller gains can be chosen constant in each sector with smooth, continuous transitions near the sector boundaries. Each sector has individual tracking priorities and the gains can be weighted based on the tracking priority of each state within a sector. For example, it is important to keep the velocity and position error low in $\mathbb{S}_1$. The current tracking performance, however, can be relaxed while only constraining $u < V_{sat}$. Therefore, more weighting can be applied to position and velocity error in $\mathbb{S}_1$. In $\mathbb{S}_2$, because of the controllability condition, the position and velocity trajectory designed in Section 6.2 assume dynamics from induced current are negligible. Therefore, an appropriate choice for the velocity and position gains would be zero. It is important, however, for current to be driven from $i_{\mathbb{S}2o} = 0$ to $i_{\mathbb{S}2f}$ accurately so that errors are small upon entry into $\mathbb{S}_3$. Therefore, weighting on current tracking could be increased in $\mathbb{S}_2$. The resulting control gains take the form of a vector valued function, $\mathcal{K}_j(x_1),\ (j = 1, 2, 3)$ where each element of $\mathcal{K}_j$ is a sector dependent constant with smooth, continuous transitions between each sector. As discussed in Section 4.2, a sign change in $K_t(x_1)$ requires a sign change in x_3 to maintain directional consistency with the position and velocity trajectory. Compensation for this requirement is inherent in the current trajectory. However, this is not reflected in the position and velocity trajectory.

Therefore, direct multiplication of the position and velocity portion of the control law by $K_t(\theta)$ will satisfy the requirement. The final control law takes the form

$$u_s = -K_t(x_1)[\mathcal{K}_1(x_1)e_1 + \mathcal{K}_2(x_1)e_2] - \mathcal{K}_3(x_1)e_3 + V_r \tag{6.7}$$

where $\mathcal{K}_1(x_1)$, $\mathcal{K}_2(x_1)$, and $\mathcal{K}_3(x_1)$ are continuous gain functions, $e_j = x_j - x_{jr}$ is the state tracking error, and x_{jr} is the desired trajectory of the j-th state. The feed-forward reference voltage is represented by

$$V_r = L\dot{x}_{3r} + Rx_{3r} + K_t(x_{1r})x_{2r} \tag{6.8}$$

Since the torque factor and bias terms in the reference trajectory are based on desired position rather than actual position, additional analysis is required for stability. The following control law

$$u_{sp} = L[\mathcal{K}_{1p}(x_1)e_1 + \mathcal{K}_{2p}(x_1)e_2 - \mathcal{K}_{3p}(x_1)e_3 + \Delta u] + V_r \tag{6.9}$$

where $\mathcal{K}_{jp}(x_1)$ are smooth, continuous gain functions provides stability in $\mathbb{S}_1$ and $\mathbb{S}_3$ when large parameter perturbations are present resulting from position error. An auxiliary control, Δu, is used to compensate for the perturbations. With knowledge of K_t, T_b, and T_f, the reference trajectory dynamics are chosen as

$$\begin{aligned} \dot{x}_{1r} &= x_{2r} \\ \dot{x}_{2r} &= \frac{1}{J}[K_t(x_{1r})x_{3r} - T_b(x_{1r}) - T_f \,\mathrm{sat}(x_{2r})] \\ \dot{x}_{3r} &= \frac{1}{L}[-K_t(x_{1r})x_{2r} - Rx_{3r}] \end{aligned} \tag{6.10}$$

Subtracting (6.10) from (6.6) and substituting u_{sp} for u gives the error dynamics

$$\begin{aligned} \dot{e}_1 &= e_2 \\ \dot{e}_2 &= \frac{1}{J}[K_t(x_1)e_3 + \Delta K_t x_{3r} - \Delta T_b - \Delta T_f] \\ \dot{e}_3 &= \frac{1}{L}[-K_t(x_1)e_2 - Re_3 - \Delta K_t x_{2r}] + u_{sp} - V_r \end{aligned} \tag{6.11}$$

where

$$\begin{aligned}\Delta K_t &= K_t(x_1) - K_t(x_{1r}),\\ \Delta T_b &= T_b(x_1) - T_b(x_{1r}),\\ \Delta T_f &= T_f\,\mathrm{sat}(x_2) - T_f\,\mathrm{sat}(x_{2r}).\end{aligned} \tag{6.12}$$

The equations in (6.12) represent the physical parameter perturbations resulting from differences in the desired and actual position.

Theorem 6.1 *The control law* (6.9) *with*

$$\begin{aligned}K_{1p}(x_1) &= \frac{J}{K_t(x_1)}\left[\gamma_1^2\lambda - \gamma_1^2\gamma_2\lambda\right]\\ K_{2p}(x_1) &= \frac{K_t(x_1)}{L} + \frac{J}{K_t(x_1)}\left[\gamma_1^2 - \gamma_1\gamma_2\lambda - \gamma_1^2\gamma_2\right]\\ K_{3p}(x_1) &= \frac{R}{L} - \frac{\dot{K}_m(x_1)}{K_t(x_1)} - \lambda - \gamma_1\gamma_2\end{aligned} \tag{6.13}$$

$$\begin{aligned}\Delta u = \frac{\Delta K_t}{L}x_{2r} - \frac{1}{K_t(x_1)}\left[(\Delta K_t)'x_{3r} + \Delta K_t\dot{x}_{3r} - (\Delta T_b)' - (\Delta T_f)'\right]\\ - \frac{1}{K_t(x_1)}\left[(\lambda+\gamma_1\gamma_2)(\Delta K_t x_{3r} - \Delta T_b - \Delta T_f)\right]\end{aligned} \tag{6.14}$$

where $\lambda, \gamma_1 > 0$, $\gamma_2 > 1$ *and* $(\cdot)'$ *denotes* $\frac{d(\cdot)}{dt}$ *renders the error dynamics* (6.11) *exponentially stable in the sectors* $\mathbb{S}_1$ *and* $\mathbb{S}_3$.

Proof. Consider the following change of variables:

$$s_1 = e_2 + \lambda e_1 \tag{6.15}$$

with dynamics

$$\dot{s}_1 = \dot{e}_2 + \lambda\dot{e}_1 \tag{6.16}$$

$$= \frac{1}{J}[K_t(x_1)e_3 + \Delta K_t x_{3r} - \Delta T_b - \Delta T_f] + \lambda e_2 \tag{6.17}$$

Defining s_2 as

$$s_2 = \frac{K_t(x_1)}{J}e_3 + \frac{\Delta K_t x_{3r} - \Delta T_b - \Delta T_f}{J} + \lambda e_2 + \gamma_1 s_1 \tag{6.18}$$

results in

$$\dot{s}_1 = -\gamma_1 s_1 + s_2 \tag{6.19}$$

The dynamics of s_2 are

$$\dot{s}_2 = \frac{\dot{K}_t(x_1)}{J} e_3 + \frac{K_t(x_1)}{J}\dot{e}_3 + \frac{(\Delta K_t)' x_{3r} + \Delta K_t \dot{x}_{3r} - (\Delta T_b)' - (\Delta T_f)'}{J} + \lambda \dot{e}_2 + \gamma_1 \dot{s}_1 \tag{6.20}$$

Substituting the error dynamics (6.11) with control law (6.9), into (6.20) and simplifying gives

$$\dot{s}_2 = (1 - \gamma_2)\gamma_1 s_2 \tag{6.21}$$

Combining (6.19) and (6.21) and recalling $\gamma_1 > 0, \gamma_2 > 1$ gives exponentially stable dynamics in s

$$\begin{bmatrix} \dot{s}_1 \\ \dot{s}_2 \end{bmatrix} = \begin{bmatrix} -\gamma_1 & 1 \\ 0 & (1-\gamma_2)\gamma_1 \end{bmatrix} \begin{bmatrix} s_1 \\ s_2 \end{bmatrix} \tag{6.22}$$

Therefore, $s_1 \to 0$ and $s_2 \to 0$ exponentially. Since $s_1 = e_2 + \lambda e_1$ and $\lambda > 0$, $e_1 \to 0$ and $e_2 \to 0$ exponentially. ■

Remark 6.1 *Notice that e_3 does not converge to zero. From* (6.18)

$$e_3 \to -\frac{\Delta K_t x_{3d} - \Delta T_b - \Delta T_f}{K_t(x_1)} \tag{6.23}$$

The variable, s_2, is selected so that the current is used to compensate for any errors that exist in the torque factor and bias relative to the actual and reference position.

Remark 6.2 *Only three gains need to be chosen. Choose γ_1 and γ_2 for the desired convergence to the invariant manifold $\{e \in \mathbb{R}^3 \mid e_2 + \lambda e_1 = 0\}$. Choose λ for the desired convergence once on the manifold.*

Remark 6.3 *The torque factor $K_t \approx 0$ in $\mathbb{S}_2$. Therefore, only current trajectory tracking is achieved. Transitioning to the following state feedback control law*

$$u_{\mathbb{S}_2} = -K_3^{\mathbb{S}2} e_3 + L\dot{x}_{3r} + R x_{3r} \tag{6.24}$$

in $\mathbb{S}_2$ *where* $K_3^{\mathbb{S}2} > -R$ *results in the exponentially stable current dynamics*

$$\dot{e}_3 = -\left(\frac{R + K_3^{\mathbb{S}2}}{L}\right) e_3 \tag{6.25}$$

Similar to (6.7), position and velocity cannot be tracked in $\mathbb{S}_2$ and the gain functions require a transition. Since the addition of Δu adds an extra element of complexity to the controller, the performance benefits may not be justified. For sample rate limited systems not subject to large disturbances, the difference may be small enough to be neglected. Comparison experimental results for both scenarios are presented in the next section.

6.3.2 Experimental Results

The experimental setup described in Section 4.4.3 was used as the test platform. Computation of the control law was fulfilled by the digital signal processor (DSP) board and the control voltage was output from the DSP board through the bipolar amplifier. The voltage drop was fed back into the DSP board to calculate the states necessary to update the control law. The velocity was computed based on a measurement of current

$$x_2 = \frac{u - Rx_3}{K_t(x_1)} \tag{6.26}$$

and integrated to get the position, x_1. The velocity obtained by using (6.26) was shown to be relatively accurate when compared to laser doppler vibrometer (LDV) measurements and provides a simple, implementable solution. It is evident from (6.26), however, that the velocity computation can become distorted near θ_c when K_t is small. Depending on the noise level of the signals, this becomes another consideration for selecting $\Delta\theta_c$. The sample rate was set at 25 kHz and $\Delta\theta_c$ was chosen to be 3° (0.0524 rad). The head loading velocity limit was set at 127 mm/s which results in $\omega_l \leq 2.8$ rad/s. A trajectory was generated based on the procedure discussed in Section 6.2. The selected control gains are given in Table 6.2 and a sample of the

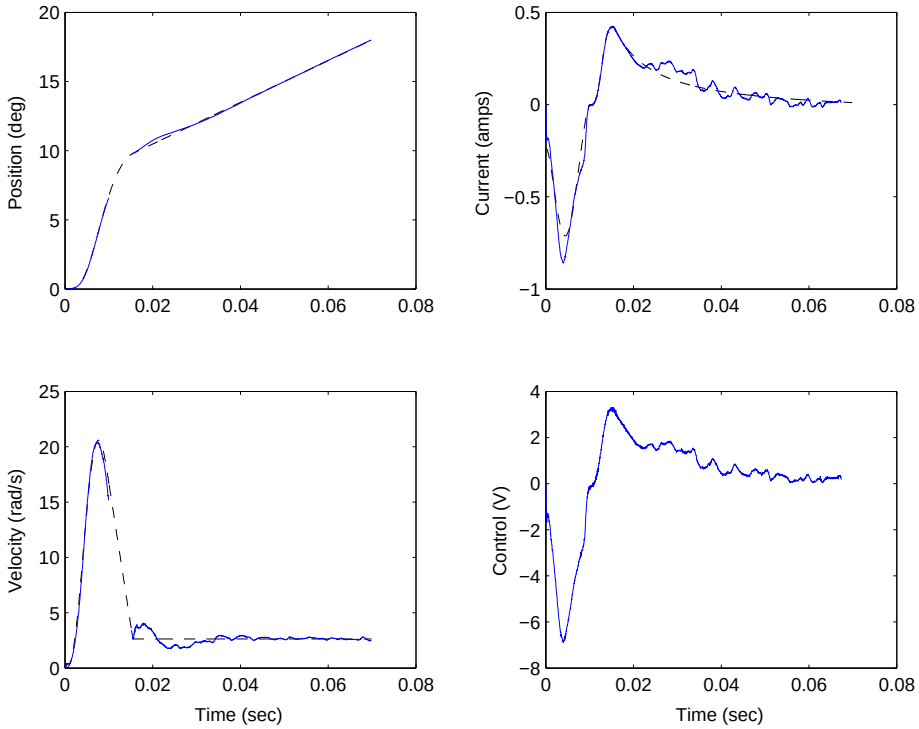

Figure 6.3: Results from ramp load state-feedback control

trajectory tracking performance for a ramp loading maneuver using (6.7) is shown in Figure 6.3. The figure shows the loading velocity and voltage saturation requirements to be satisfied. Additionally, the maximum angular acceleration imparted to the head was calculated to be $\alpha = 4.67$ krad/s^2 which is well below α_{max}. Therefore, all the constraints were satisfied using the state-feedback controller. Because K_t is small in $\mathbb{S}_2$, and K_1 and K_2 are zero, velocity and position were not computed directly in $\mathbb{S}_2$.

Table 6.2: State-feedback control gains

Gain	$\mathbb{S}_1$	$\mathbb{S}_2$	$\mathbb{S}_3$
K_1	25000	0	5000
K_2	40	0	30
K_3	0.01	20	0.01

The region around the ramp cannot be shrouded to direct air flow. Therefore, disk windage can have a significant effect on low velocity tracking in $\mathbb{S}_3$. This is seen as non-periodic "ripple" in the control signal of Figure 6.3. The ramps used were unfinished, injection mold prototypes which can also have an effect on the controller during low velocity tracking. The error norms using controller (6.7) and (6.9) are given in Table 6.3. The norms reflect the weighting strategy discussed in Section 6.3.1 where current tracking performance only becomes significant while maneuvering through the critical angle. Control law (6.9) exhibited slightly improved position and velocity tracking performance. The increase in current error results from the added terms in Δu that compensate for errors in the torque factor and bias relative to the actual and reference trajectory.

Table 6.3: Controller performance

L_2 norm	$\mathbb{S}_1$		$\mathbb{S}_2$		$\mathbb{S}_3$	
	u_s	u_{sp}	u_s	u_{sp}	u_s	u_{sp}
e_1	0.02	0.016	-	-	0.06	0.04
e_2	9.33	8.21	-	-	15.57	13.33
e_3	1.42	1.61	0.01	0.01	1.23	1.55

6.4 Output Feedback Control

The controller in Section 6.3 relies on full state feedback where the velocity and position states were computed using current measurement and neglecting coil inductance effects. This section develops a more comprehensive solution including a state observer that considers the entire nonlinear model. A stable, output feedback design with nonlinear observation is provided for state estimation feedback similar to the

design of Section 3.5. By redefining the nonlinearities as

$$K_\phi(x_1) = \begin{cases} K_t(x_1) - K_t^{OCS}, & \theta < \theta_c \\ K_t(x_1) - K_t^{DZ}, & \theta > \theta_c \end{cases} \tag{6.27}$$

$$T_\phi(x_1) = T_b(x_1) - c_1 x_1 \tag{6.28}$$

equation (6.6) can be rewritten as

$$\begin{aligned} \dot{x} &= Ax + Bu + \Phi(x) \\ y &= Cx \end{aligned} \tag{6.29}$$

where

$$A = \begin{bmatrix} 0 & 1 & 0 \\ -\mu_1 c_1 & 0 & \mu_1 \nu \\ 0 & -\mu_3 \nu & -\mu_3 R \end{bmatrix}, \qquad \nu = \begin{cases} K_t^{OCS}, & x_1 < \theta_c \\ K_t^{DZ}, & x_1 > \theta_c \end{cases} \tag{6.30}$$

$$B = \begin{bmatrix} 0 \\ 0 \\ \mu_3 \end{bmatrix} \quad C^T = \begin{bmatrix} 0 \\ 0 \\ 1 \end{bmatrix} \tag{6.31}$$

and

$$\Phi(x) = \begin{bmatrix} 0 \\ \mu_1\{K_\phi(x_1)x_3 - T_\phi(x_1) - T_f \,\mathrm{sat}(x_2)\} \\ -\mu_3 K_\phi(x_1) x_2 \end{bmatrix} \tag{6.32}$$

where $\mu_1 = \frac{1}{J}$ and $\mu_3 = \frac{1}{L}$. Equation (6.30) defines two separate model representations dependent on the actuator position relative to the critical angle. The controller design presented in the next section requires the vector valued nonlinearity, Φ, be locally Lipschitz within the set of all possible actuator angular positions on the ramp

$$\|\Phi(x_a) - \Phi(x_b)\| \leq \gamma \|x_a - x_b\| \tag{6.33}$$

$$\forall\, x_a, x_b \in X \quad X := \{x \in \mathbb{R}^3 |\, 0 \leq x_1 \leq \theta_r\}$$

Lemma 6.1 *Let $\Phi : U \to \mathbb{R}^n$ be a vector valued funtion continuous on some $U \subset \mathbb{R}^n$. Suppose that $[\partial\Phi/\partial x]$ exists and is continuous on U. If for a convex subset $X \subset U$, there is a constant $\gamma \geq 0$ such that*

$$\left\| \frac{\partial \Phi}{\partial x}(x) \right\|_2 \leq \gamma, \quad \forall\, x \in X$$

then

$$\|\Phi(x_a) - \Phi(x_b)\|_2 \leq \gamma \|x_a - x_b\|_2, \quad \forall\, x \in X$$

Proof. Consider a vector $z \in \mathbb{R}^n$ where $\|z\|_2 = 1$ and let $\rho(s) = (1-s)x_a + sx_b$ for all $s \in \mathbb{R}$ such that $\rho(s) \in U$. Since $X \subset U$ is convex, $\rho(s) \in X,\ \forall\, s \in [0,1]$. Furthermore, $q(s) = z^\top \Phi(\rho(s))$ is a real valued function that is continuously differentiable in an open interval of $[0,1]$. From the mean-value theorem, there exists $s_0 \in (0,1)$ such that

$$q(1) - q(0) = q'(s_0)$$

It follows that

$$\begin{aligned} z^\top [\Phi(x_a) - \Phi(x_b)] &= z^\top \left[\frac{\partial \Phi}{\partial x}(\rho(x)) \right] (x_b - x_a) \\ \|\Phi(x_a) - \Phi(x_b)\|_2 &= \|z\|_2 \left\| \frac{\partial \Phi}{\partial x}(\rho(x)) \right\|_2 \|x_b - x_a\|_2 \\ &\leq \gamma \, \|x_b - x_a\|_2 \end{aligned}$$

■

Since, Φ as defined in (6.32) is a C^1 vector field for all $x \in X$, $[\partial\Phi/\partial x]$ exists and is finite. Therefore, by Lemma 6.1, a Lipschitz constant can be determined satisfying (6.33).

It can be readily determined that (A, B) is controllable for $\theta \neq \theta_c$ and observability of (A, C) requires $c_1 \neq 0$. Consideration of this requirement can be taken during the actuator design phase. The designer has flexibility on positioning and size of the magnetic bias feature which will ultimately effect the profile of the restoration bias

torque over the ramp angle. Therefore, a profile can be developed that delivers a non-zero linear component when approximating magnetic bias torque.

6.4.1 Controller Design

A predetermined reference trajectory, x_r, satisfies a reference model

$$\dot{x}_r = Ax_r + Bu_r + \Phi(x_r) \tag{6.34}$$

In order to fulfill the ramp loading requirements and manage the nonlinearities outlined in Section 4.2, an output feedback controller is developed. The controller consists of a linear state feedback control law coupled with a nonlinear observer. A new metric is derived from Definition 3.1 to analyze the stability properties of the system error dynamics

$$\delta_s(\mathcal{A}) = \delta(\mathcal{A}, \mathbf{0})$$

where δ_s represents the *distance to instability* of a system matrix, $\mathcal{A}$.

Theorem 6.2 *Let* $X := \{x \in \mathbb{R}^3 | \, 0 \leq x_1 \leq \theta_r\}$ *where* θ_r *is the actuator ramp angle and* $\Phi(x)$ *is Lipschitz according to* (6.33)*. The output tracking control law*

$$u = L(\dot{x}_{3r} + \mu_3 x_{3r} + \mu_2 x_{2r}) - \mathcal{K}_c \hat{e} \tag{6.35}$$

with $\hat{e} = \hat{x} - x_r$ *and nonlinear observer*

$$\dot{\hat{x}} = A\hat{x} + Bu + \Phi(\hat{x}) + \mathcal{L}_o(y - C\hat{x}) \tag{6.36}$$

where $\mathcal{K}_c, \mathcal{L}_o \in \mathbb{R}^3$ *are gain vectors chosen such that* $A_c = A - B\mathcal{K}_c$ *and* $A_o = A - \mathcal{L}_o C$ *are Hurwitz, renders the tracking error dynamics*

$$\dot{e} = A_c e + \Phi(x) - \Phi(x_r), \quad e = x - x_r \tag{6.37}$$

and observer error dynamics

$$\dot{\tilde{x}} = A_o \tilde{x} + \Phi(x) - \Phi(\hat{x}), \quad \tilde{x} = x - \hat{x} \tag{6.38}$$

exponentially stable for all $x \in X$ if

$$\gamma < \delta_s(A_c) \quad \textit{and} \quad \gamma < \delta_s(A_o) \tag{6.39}$$

Proof. Substituting (6.35) into (6.6) gives

$$\dot{e} = A_c e + B_c \mathcal{K}_c \tilde{x} + \Phi(x) - \Phi(x_r) \tag{6.40}$$

Consider a Lyapunov function candidate

$$V(e, \tilde{x}) = \xi e^T P_c e + \tilde{x}^T P_o \tilde{x} \tag{6.41}$$

where ξ is a positive constant and $P_c, P_o \in \mathbb{R}^{3\times 3}$ are symmetric, positive definite. Taking the time derivative of (6.41) yields

$$\begin{aligned}
\dot{V}(e, \tilde{x}) &= \xi\{e^T(A_c^T P_c + P_c A_c)e + 2e^T P_c[\Phi(x) - \Phi(x_r)] + 2e^T P_c B_c \mathcal{K}_c \tilde{x}\} \\
&\quad + \tilde{x}^T[A_o^T P_o + P_o A_o]\tilde{x} + 2\tilde{x}^T P_o[\Phi(x) - \Phi(\hat{x})] \\
&\leq \xi\{e^T(A_c^T P_c + P_c A_c)e + 2\gamma\|P_c e\|\,\|e\| + 2P_c B_c \mathcal{K}_c\|e\|\,\|\tilde{x}\|\} \\
&\quad + \tilde{x}^T(A_o^T P_o + P_o A_o)\tilde{x} + 2\gamma\|P_o\tilde{x}\|\,\|\tilde{x}\| \\
&\leq \xi\{e^T(A_c^T P_c + P_c A_c + P_c P_c + \gamma^2 I)e + 2P_c B_c \mathcal{K}_c\|e\|\,\|\tilde{x}\|\} \\
&\quad + \tilde{x}^T(A_o^T P_o + P_o A_o + P_o P_o + \gamma^2 I)\tilde{x}
\end{aligned} \tag{6.42}$$

Now, from Lemma 3.1, for any $\eta_c, \eta_o > 0$, there exist symmetric, positive definite P_c, P_o such that

$$A_c^T P_c + P_c A_c + P_c P_c + \gamma^2 I = -\eta_c I \quad \text{and} \quad A_o^T P_o + P_o A_o + P_o P_o + \gamma^2 I = -\eta_o I \tag{6.43}$$

if the associated Hamiltonian matrices

$$\mathbb{H}_c = \begin{bmatrix} A_c & I \\ -(\gamma^2 + \eta_c)I & -A_c^T \end{bmatrix} \quad \text{and} \quad \mathbb{H}_o = \begin{bmatrix} A_o & I \\ -(\gamma^2 + \eta_o)I & -A_o^T \end{bmatrix} \tag{6.44}$$

are hyperbolic. From (6.39) in the hypothesis, consider the continuous function $f(\gamma) = \gamma^2 - \delta_s^2(A_c) < 0$. Since f is continuous, there exists $\eta_c > 0$ such that

$$f(\gamma) = \gamma^2 + \eta_c - \delta_s^2(A_c) < 0 \quad \text{or} \quad \sqrt{\gamma^2 + \eta_c} < \delta_s(A_c)$$

A similar continuity argument can be made regarding the observer resulting in

$$\sqrt{\gamma^2 + \eta_o} < \delta_s(A_o)$$

Therefore, the Hamiltonian matrices of (6.44) are hyperbolic and it follows from (6.43) that

$$\dot{V}_c(e, \tilde{x}) \leq -\xi\eta_c\|e\|^2 + 2\xi P_c B_c \mathcal{K}_c \|e\| \, \|\tilde{x}\| - \eta_o\|\tilde{x}\|^2 \tag{6.45}$$

Defining $\xi_c = 2\|P_c B_c \mathcal{K}_c\|, \xi = \frac{\eta_c\eta_o}{\xi_c^2}$, and noting

$$\left(\frac{1}{\sqrt{2}}\frac{\eta_c\sqrt{\eta_o}}{\xi_c}\|e\| - \frac{1}{\sqrt{2}}\sqrt{\eta_o}\|\tilde{x}\|\right)^2 \geq 0 \tag{6.46}$$

gives

$$\dot{V}(e, \tilde{x}) \leq -\xi\eta_c\|e\|^2 + \xi\xi_c\|e\| \, \|\tilde{x}\| - \eta_o\|\tilde{x}\|^2 \tag{6.47}$$

$$\leq -\frac{\eta_c^2\eta_o}{\xi_c^2}\|e\|^2 + \frac{\eta_c\eta_o}{\xi_c}\|e\| \, \|\tilde{x}\| - \eta_o\|\tilde{x}\|^2 \tag{6.48}$$

$$\leq -\frac{1}{2}\left(\frac{\eta_c^2\eta_o}{\xi_c^2}\|e\|^2 + \eta_o\|\tilde{x}\|^2\right) \tag{6.49}$$

Therefore, $V(e, \tilde{x})$ is a Lyapunov function and $e, \tilde{x} \to 0$ exponentially as $t \to \infty$. ■

Remark 6.4 *Since A_c and A_o are both Hurwitz, the controller* (6.35) *and observer* (6.36) *provide stable tracking dynamics in the data zone when nonlinear effects dissipate. Therefore, a seamless transition can occur when the actuator moves between the ramp and data zone region without redesigning the controller and observer gains.*

6.4.2 Simulation Results

Simulations were performed to get an initial estimate of the appropriate controller and observer gains required for a successful ramp load maneuver. It was also desired to evaluate the controller performance based on realistic variational limits of the state initial conditions. Geometric tolerance analysis of the actuator R/W heads relative to the ramp position resulted in a potential variation of 0.0037 rad. It was assumed

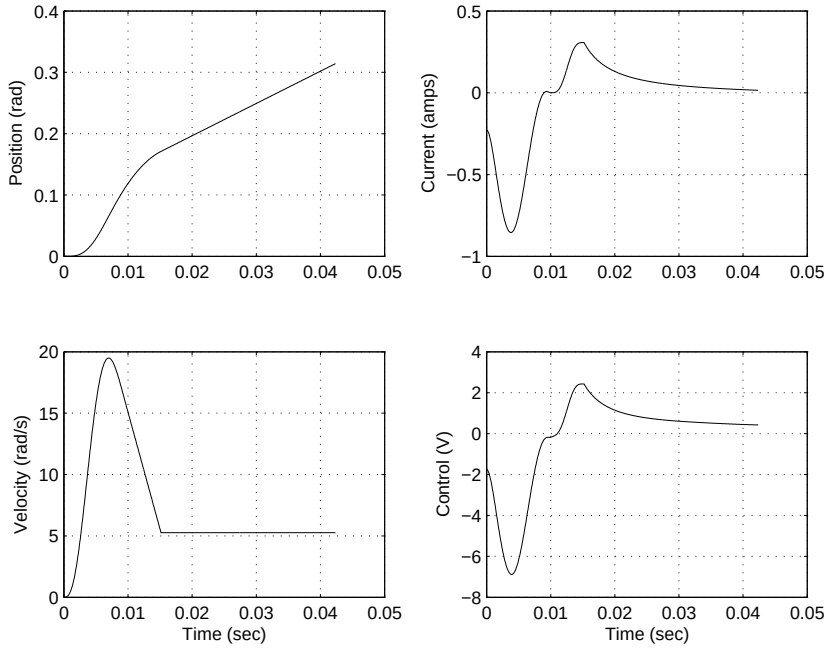

Figure 6.4: Output feedback reference trajectory profile

the actuator would always be motionless prior to a loading maneuver and therefore, have no initial velocity observation error. Amplifier noise levels, however, could vary as much as 10 mA peak-to-peak. Based on the tolerance analysis, the simulation was loaded with the state and observer initial conditions $x_0 = [0.0037 \;\; 0 \;\; 0.01]^T$ and $\hat{x}_0 = [0 \;\; 0 \;\; 0]^T$, respectively. Choosing $\Delta\theta_c = 0.0524$ rad (3°), and loading velocity $\omega_l = 5.56$ rad/s (10 in/s), a trajectory was generated based on the procedure defined in Section 6.2. The sector transitions occur at 10 msec and 15.1 msec, for $\mathbb{S}_1 \rightarrow \mathbb{S}_2$ and $\mathbb{S}_2 \rightarrow \mathbb{S}_3$, respectively. The trajectory is shown in Figure 6.4 and results in a maximum angular acceleration of $\alpha_{max} = 4.867$ krad/s^2; well below the required limit. An iteration procedure was undertaken to determine a set of gains that satisfy the requirements of Section 6.4.1 and provide an initial reference for tuning during the experimental phase. In this case δ_s was evaluated for condition (6.39) subsequent to selecting the gains $\mathcal{K}_c$ and $\mathcal{L}_o$. The following computational results are for the controller design in $\mathbb{S}_1$ and the system representation (6.29). Recall from Remark 3.2,

a coordinate transformation can be used to reduce the value of γ and increase δ_s. From the Lipschitz condition with transformation, T_c,

$$\|T_c^{-1}\phi(T_c x_a) - T_c^{-1}\phi(T_c x_b)\| \leq \gamma' \|x_a - x_b\| \tag{6.50}$$

The Lipschitz constant was determined as $\gamma' = 1.35$ using a transformation

$$T_c = \text{diag}[1 \ 10^6 \ 10^5]$$

The state feedback control gains

$$\mathcal{K}_c^{\mathbb{S}1} = [-2094 \quad -3.74 \quad 0.13] \tag{6.51}$$

result in a distance to instability $\delta_s(A_c) = 2.16$. Choosing $\eta_c = 1$ results in $\sqrt{(\gamma')^2 + \eta_c} = 1.68 < 2.16$ which satisfies (6.39) resulting in the symmetric, positive definite solution

$$P_c = \begin{bmatrix} 0.003 & 0.006 & -0.0002 \\ 0.006 & 1.501 & -0.049 \\ -0.0002 & -0.049 & 0.0016 \end{bmatrix} \tag{6.52}$$

For the observer design, the Lipschitz condition is

$$\|T_o^{-1}\phi(T_o x_a) - T_o^{-1}\phi(T_o x_b)\| \leq \gamma' \|x_a - x_b\| \tag{6.53}$$

The Lipschitz constant was determined as $\gamma' = 1.35$ using the transformation

$$T_o = \text{diag}[1 \ 10^5 \ 10^5]$$

The observer gains

$$\mathcal{L}_o^{\mathbb{S}1} = [-573 \quad 87096 \quad 1950] \tag{6.54}$$

result in a distance to instability $\delta_s(A_o) = 2.73$. Choosing $\eta_o = 1$ results in $\sqrt{(\gamma')^2 + \eta_o} = 1.68 < 2.73$ which satisfies (6.39) resulting in the symmetric, positive definite solution

$$P_o = \begin{bmatrix} 35.44 & -0.702 & 0.0014 \\ -0.702 & 0.024 & 0.00004 \\ 0.0014 & 0.00004 & 0.0001 \end{bmatrix} \tag{6.55}$$

The following computational results are for the controller design in $\mathbb{S}_3$:

Transformation: $T_c = \text{diag}[1\ 10^6\ 10^5] \longrightarrow \gamma' = 1.35$

Control gains: $\mathcal{K}_c^{\mathbb{S}3} = [1594\ 3.74\ 0.13] \longrightarrow \delta_s(A_c) = 3.27$

Condition: $\eta_c = 1 \longrightarrow \sqrt{(\gamma')^2 + \eta_c} = 1.67 < 3.27$

$$P_c = \begin{bmatrix} 0.003 & 0.41 & 0.03 \\ 0.41 & 52.90 & 3.48 \\ 0.027 & 3.48 & 0.23 \end{bmatrix}$$

Transformation: $T_o = \text{diag}[1\ 10^5\ 10^5] \longrightarrow \gamma' = 1.35$

Observer gains: $\mathcal{L}_o^{\mathbb{S}3} = [-103\ \ -38982\ \ 1973] \longrightarrow \delta_s(A_o) = 2.12$

Condition: $\eta_o = 1 \rightarrow \sqrt{(\gamma')^2 + \eta_o} = 1.68 < 2.12$

$$P_o = \begin{bmatrix} 32.61 & -0.004 & -0.001 \\ -0.004 & 0.0306 & -0.00002 \\ -0.001 & -0.00002 & 0.00005 \end{bmatrix}$$

Control in $\mathbb{S}_2$ involved only the current dynamics (5.31) and the gains were selected as noted in Table 6.4.

The ramp load simulation results are shown in Figures 6.5-6.7. Figure 6.6 manifests the gain strategy discussed in Section 6.3.1 where position and velocity tracking is prioritized in $\mathbb{S}_1$ and $\mathbb{S}_3$ while current is prioritized in $\mathbb{S}_2$.

Table 6.4: Simulation controller gains

Gain	$\mathbb{S}_1$	$\mathbb{S}_2$	$\mathbb{S}_3$
$\mathcal{K}_{c1}$	-2094	0	1594
$\mathcal{K}_{c2}$	-3.74	0	3.74
$\mathcal{K}_{c3}$	0.13	13.5	0.13
$\mathcal{L}_{o1}$	-573	0	-103
$\mathcal{L}_{o2}$	87096	0	-38982
$\mathcal{L}_{o3}$	1950	843	1973

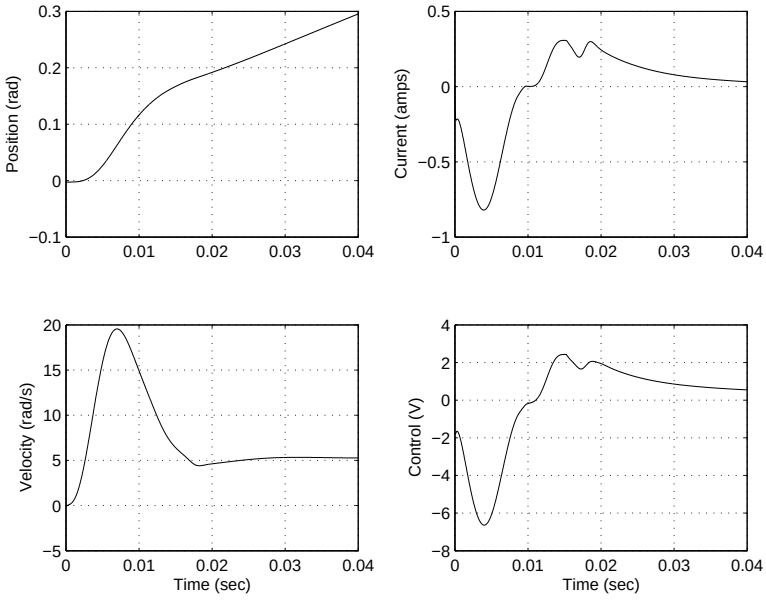

Figure 6.5: Simulated trajectory profiles (observer with toleranced initial conditions)

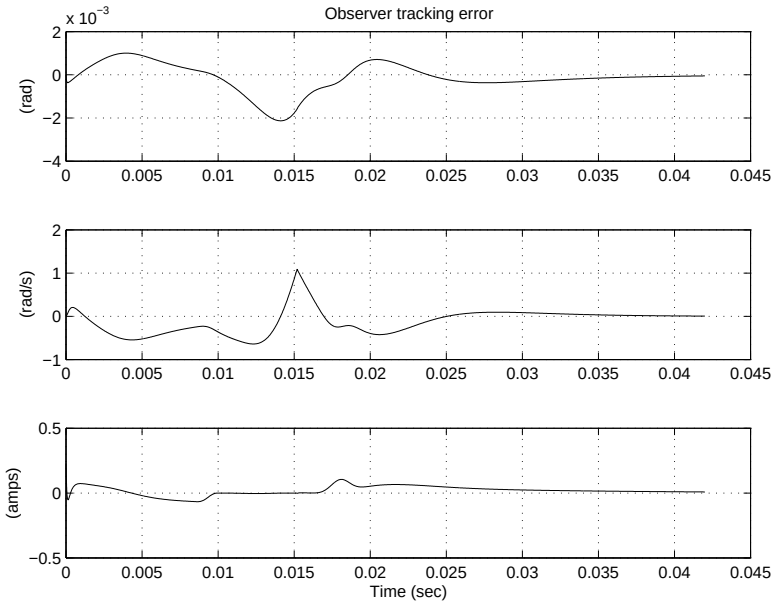

Figure 6.6: Simulated tracking error (observer with toleranced initial conditions)

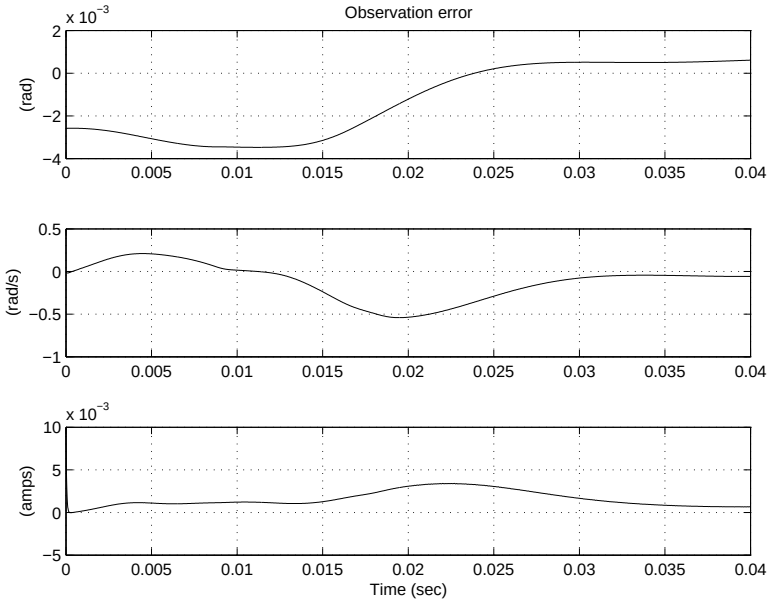

Figure 6.7: Simulated observer error (observer with toleranced initial conditions)

6.4.3 Experimental Results

To ultimately verify the feasibility of the proposed ramp loading design scheme, experiments were necessary to evaluate the performance in a realistic test case. The test setup of Section 4.4.3 was used for experimental analysis. It was desired to track the state reference trajectory developed for simulation in Section 6.4.2 while meeting the performance requirements of Table 6.1. The observer was loaded with the initial conditions $\hat{x}_0 = [0\ 0\ 0]^T$ and the results from Table 6.4 were used as an initial set of gains. Iterative tuning of several L/UL operations produced an admissible set of gains which satisfied the tracking requirements of Section 6.4.1. The following computational results are for the controller design in $\mathbb{S}_1$:

Transformation: $T_c = \text{diag}[1\ 10^5\ 10^6] \longrightarrow \gamma' = 1.35$

Control gains: $\mathcal{K}_c^{\mathbb{S}1} = [-830\ \ -1.63\ \ 0.3] \longrightarrow \delta_s(A_c) = 2.50$

Condition: $\eta_c = 1 \longrightarrow \sqrt{(\gamma')^2 + \eta_c} = 1.68 < 2.50$

$$P_c = \begin{bmatrix} 0.003 & 0.154 & -0.487 \\ 0.154 & 8.64 & -27.86 \\ -0.487 & -27.86 & 89.95 \end{bmatrix}$$

Transformation: $T_o = \text{diag}[1\ 10^5\ 10^5] \longrightarrow \gamma' = 1.35$

Observer gains: $\mathcal{L}_o^{\mathbb{S}1} = [112.5\ 45991\ 808] \longrightarrow \delta_s(A_o) = 2.08$

Condition: $\eta_o = 1 \rightarrow \sqrt{(\gamma')^2 + \eta_o} = 1.68 < 2.08$

$$P_o = \begin{bmatrix} 1.002 & -0.06 & -0.0005 \\ -0.06 & 0.016 & 0.00006 \\ -0.0005 & 0.00006 & 0.00006 \end{bmatrix}$$

The following computational results are for the controller design in $\mathbb{S}_3$

Transformation: $T_c = \text{diag}[1\ 10^5\ 10^5] \longrightarrow \gamma' = 1.35$

Control gains: $\mathcal{K}_c^{\mathbb{S}3} = [100\ 3.5\ 0.3] \longrightarrow \delta_s(A_c) = 1.82$

Condition: $\eta_c = 1 \longrightarrow \sqrt{(\gamma')^2 + \eta_c} = 1.68 < 1.82$

$$P_c = \begin{bmatrix} 0.039 & 0.550 & 0.355 \\ 0.550 & 7.712 & 4.987 \\ 0.355 & 4.987 & 3.227 \end{bmatrix}$$

Transformation: $T_o = \text{diag}[1\ 10^5\ 10^5] \longrightarrow \gamma' = 1.35$

Observer gains: $\mathcal{L}_o^{\mathbb{S}3} = [-112.5\ \ -45991\ \ 808] \longrightarrow \delta_s(A_o) = 1.74$

Condition: $\eta_o = 1 \rightarrow \sqrt{(\gamma')^2 + \eta_o} = 1.68 < 1.74$

$$P_o = \begin{bmatrix} 2.92 & -0.131 & 0.0012 \\ -0.131 & 0.042 & -0.0001 \\ 0.0012 & -0.0001 & 0.0001 \end{bmatrix}$$

Table 6.5: Experimental controller gains

Gain	$\mathbb{S}_1$	$\mathbb{S}_2$	$\mathbb{S}_3$
$\mathcal{K}_{c1}$	-830	0	100
$\mathcal{K}_{c2}$	-1.63	0	3.5
$\mathcal{K}_{c3}$	0.3	5	0.3
$\mathcal{L}_{o1}$	112.5	0	-112.5
$\mathcal{L}_{o2}$	45991	0	-45991
$\mathcal{L}_{o3}$	808	808	808

Control in $\mathbb{S}_2$ involved only the current dynamics and the gains were selected as noted in Table 6.5. Figure 6.8 shows a sample trajectory of a typical ramp load maneuver

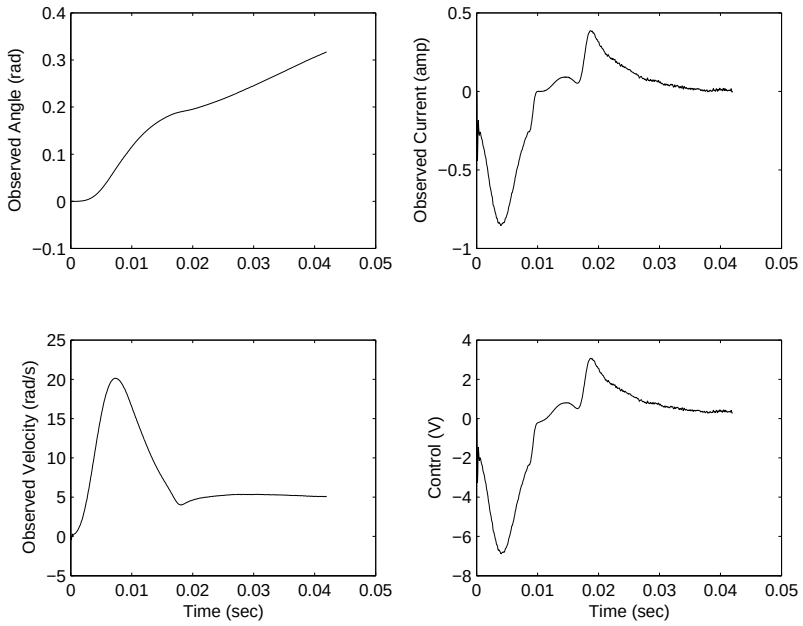

Figure 6.8: Experimental trajectory profiles

using the gains of Table 6.5. The inherent filtering characteristics of the observer is noticed when compared to the state feedback results of Figure 6.3. Therefore, the controller is less sensitive to high frequency windage disturbances prior to head loading. The tracking performance exhibited in Figure 6.9 reflects the weighting strategy discussed in Section 6.3.1 where current tracking performance only becomes significant while maneuvering through the critical angle. The position and velocity error increase as expected in $\mathbb{S}_2$ while the current error decreases. The converse is true in $\mathbb{S}_1$ and $\mathbb{S}_3$. It can be verified that the loading velocity and control input requirements are met. It is desirable that any velocity error present at the end of the maneuver satisfy $\hat{e}_2 < 0$ indicating $\hat{x}_2 < \omega_l$. Additionally, the maximum angular acceleration imparted to the head was calculated to be $\alpha < 5.5$ krad/s^2 which is well below α_{max} and the position error stays within 0.0075 rad (0.43°). The large transient at the beginning of the current profile is a result of immediate bias compensation reflected in the reference trajectory. Figure 6.10 shows acceptable performance of the

current observer below 40 mA after the initial transient and below 10 mA in $\mathbb{S}_3$ prior to loading. The two anomalies at 8 msec and 16 msec result from travel through the sector boundaries where the observer transitions between open and closed loop in the position and velocity states. Repeatability was verified by completing 50 consecutive L/UL cycles without failure.

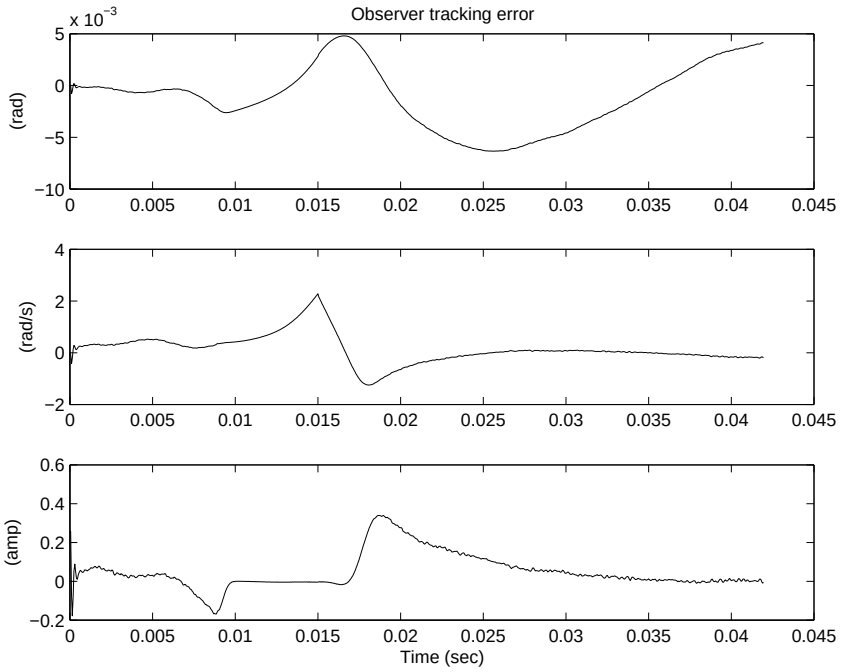

Figure 6.9: Experimental tracking error performance

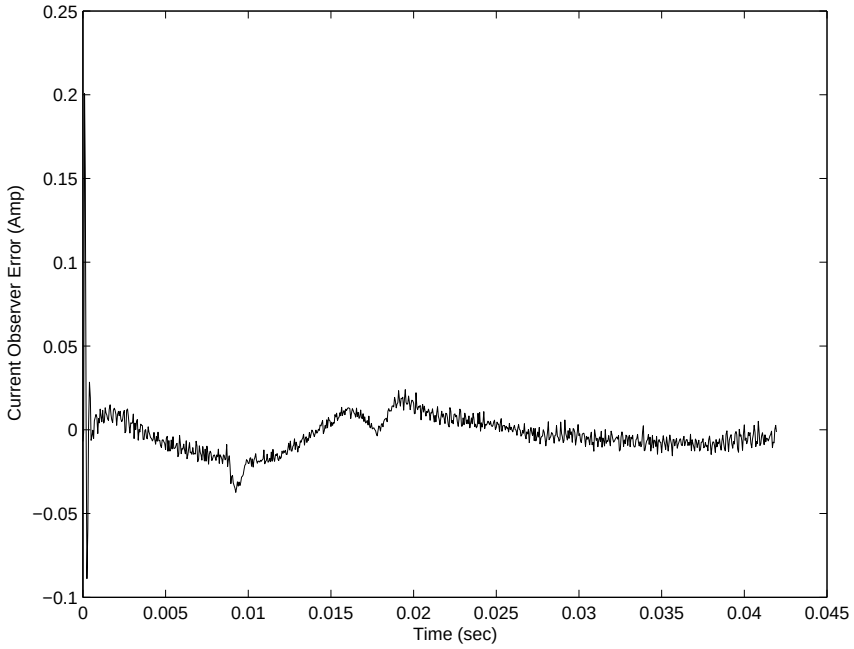

Figure 6.10: Current observer error

6.5 Summary

The research studied feasibility of ramp L/UL functionality and performance using a unique ramp load disk drive actuator. A model reference trajectory generation scheme is developed that, when tracked using closed loop control, moves the actuator through the uncontrollable region for a successful load onto the disk. The motor torque factor, bias, and friction nonlinearities can be represented by functions that are Lipschitz within the actuator state-space. A robust, state-feedback control law was designed that compensates for errors in the actual and calculated states as functions of the nonlinearities. To compensate for lack of direct position and velocity measurement, a stable, output feedback tracking controller was developed to track the trajectory while handling the nonlinear effects. Experiments were performed on a unique ramp load disk drive to verify the proposed ramp loading scheme. The output feedback controller

provided high frequency disturbance attenuation during tracking while meeting all necessary performance requirements. Repeatability was demonstrated by sequentially completing a series of L/UL operations.

CHAPTER 7

SUMMARY AND FUTURE WORK

As disk drive manufacturers search for cost reduction opportunities, customers continue to demand steady quality and performance improvements. Shock damage of the head/disk interface is one area that causes many quality issues and cost constraints. Some of the most damaging shocks occur when the drive is in a non-operational state. These shocks can be both linear and rotational in nature. Many of the methods currently used to suppress shock dynamics preserve servo control performance at the expense of cost increases and quality issues. This research focused on enhanced disk drive actuator design and control strategies that improve performance while reducing part cost and quality concerns associated with suppressing the effects of non-operational shocks.

A voice-coil motor actuator for a disk drive was designed in Chapter 2 to meet specific move-time performance requirements. Using an energy equivalence method, a quantitative determination was derived of the bias torque necessary to reject a rotational shock and return the actuator arm back to the nominal shipping position. A stainless steel member was designed and attached to the actuator arm producing a non-contact, magnetic bias to fulfill the non-operational, rotary shock requirements. The magnetic bias provided a low cost, reliable alternative to latches currently used in industry today. However, it was determined that the overall magnetic and flex circuit bias torque profile was nonlinear throughout the actuator sweep angle which can have detrimental effects on seek performance. The actuator was manufactured according to the desired design requirements and measurements were taken of the

motor physical parameters. A dynamic model was developed for the actuator, which included the bias force nonlinearity.

Seek control methodologies to combat the nonlinearity induced by the bias design are presented. It was assumed that the exact bias characteristic was unknown for a given drive population, but a nominal estimate was measured for a specific drive. An adaptive controller was designed to track a predetermined reference trajectory and compensate for bias uncertainty. A state-feedback controller was developed for comparison. Experiments were conducted to verify the design and performance requirements. The experiments confirmed that the adaptive control outperforms the state-feedback with slightly more power consumption. A geometric tolerance analysis resulted in bounds that constrain the bias torque for a given drive population. With knowledge of the bounds, a projection algorithm was implemented to constrain the bias estimate below a cumulative upper bound. A performance reduction was noted with the addition of projection along with an increase in implementation complexity. Overall, the adaptive controller adds a degree of complexity that promotes sample rate limitations resulting from processor computation delay. Additional memory or processor resources might be required which may not be feasible for disk drives targeting low cost markets. Performance effects from a reduction in bias estimate accuracy were also investigated. It was determined that controller performance lost by a reduction in bias modeling accuracy could be recovered by an increase in sample rate. Therefore, if sampling resources are available, the complexity of the controller can be reduced without significant sacrifices in performance. The experimental environment produced a velocity measurement which allowed full state feedback for the control law computation. However, production disk drives are not capable of direct velocity measurement. An output feedback tracking controller, using only current measurement, was developed for the actuator performing a seek maneuver. In this case, the bias was assumed to be known exactly and shown to be locally Lipschitz within the

actuator sweep angle. In addition to satisfying the separation principle, the output feedback controller induced exponentially stable tracking error dynamics. Experimentally, the controller exhibited successful tracking performance of a predetermined reference trajectory with a bias 5% of the maximum available torque. The position and velocity tracking error increased with seek length while current error decreased. Experiments also revealed observer convergence with initial condition variation.

Non-operational shocks can also inflict undesirable linear dynamics. Chapter 4 discusses a reliable, low cost solution for suppressing the effects of non-operational linear shocks. The solution uses a well-known linear shock protection scheme by parking the R/W heads on a ramp when the drive is not in operation. The heads are loaded on and off of the disks when the drive power is turned on and off, respectively. Loading and unloading was performed with a unique, low cost actuator that provided a lower cost, higher torque solution while realizing the shock resistance benefits of ramp loading. However, when used in a ramp loading scheme, the actuator exhibits a region that is not controllable by induced coil current. A voice-coil motor actuator was designed and optimized for cost and performance without consideration for ramp loading. The methods of Chapter 2 were used to develop a magnetic bias solution for rotary shock and prevent the actuator from resting at the uncontrollable condition. Both the motor torque factor and magnetic bias were shown to be nonlinear along the ramp angle. A ramp design was also discussed that defines the velocity with which the heads are required to load onto the disks. A disk drive was fabricated to provide ramp loading capability with the unique actuator. All actuator physical parameters were measured to verify the design and simulations coupled with experiments revealed the expected shock and move time performance requirements were satisfied. Results were compared to a nominal L/UL actuator to demonstrating superiority of the commutational ramp load (CRL) design. A final open-loop experiment was performed to characterize and identify the uncontrollable region.

In addition to the uncontrollable condition the CRL actuator exhibits an input singularity that makes exact input/output tracking impossible. The input singularity coincides with the uncontrollable condition at a specific *critical point* further complicating the control design. The CRL actuator is compared to the well-known ball and beam system where a deficiency is revealed in the ability of existing control methods to track in a neighborhood of the critical point. An extensive dynamic analysis of the CRL actuator resulted in a sufficient condition guaranteeing motion through the critical point which sets the basis of trajectory generation for closed loop control.

It was necessary to design a reference trajectory such that, when tracked, moves the actuator through the uncontrollable region for a successful load onto the disk. A step-by-step trajectory generation procedure was proposed based on the sufficient condition and two controllers were developed to track the trajectory throughout the loading process. One controller used full-state feedback and provides robustness to errors in the actual and calculated states as functions of the nonlinearities. To compensate for lack of direct position and velocity measurement, an exponentially stable, output feedback controller was developed to track the trajectory while handling the nonlinear effects. Experimental results revealed that both controllers tracked the trajectory and successfully loaded the R/W heads on the disk while maintaining the required ramp loading specifications. The inherent filtering characteristics of the output feedback controller provided robustness to high frequency disk windage disturbances as the actuator rotated close to the disk outer radius. Repeatability was demonstrated by sequentially completing a series of L/UL operations.

This work investigated a nonlinear bias solution for actuator protection against non-operational rotary shock. Armed with full-state feedback, an adaptive controller is developed to compensate for the nonlinearity and any associated uncertainties during a seek maneuver. Knowing that direct velocity measurement is unavailable in production disk drives, an output feedback controller, using only current measurement,

is designed to handle nonlinear effects when an *exact* description of the nonlinearity is known. Future work should combine the scenarios and investigate output feedback control with uncertain nonlinear effects. Similarly for the CRL actuator, compensation for uncertain effects in friction, disk windage, and actuator physical parameters should be implemented with output feedback control. Additionally, the theoretical development of provided for non-regular systems should be expanded to further characterize and compensate for the effects of uncontrollable, input singularities.

BIBLIOGRAPHY

[1] S. G. Campbell, "Magnetically biased aerodynamically released integral safety latch for rigid disk drive." U.S. Patent 4692829, September 1987.

[2] J. H. Morehouse, J. A. Dunckley, and D. M. Furay, "Rotary inertial latch for disk drive actuator." U.S. Patent 5189576, February 1993.

[3] G. Kelsic and J. Martinez, "Magnetic latch for disk drive actuator." U.S. Patent 5023736, June 1991.

[4] R. C. Reinhart, "Disk drive magnetic actuator latch mechanism having a latch lever with magnetic members on each end thereof for latching and unlatching the actuator using voice coil motor magnet." U.S. Patent 5734527, March 1998.

[5] Y. Kinoshita, "Actuator arm with magnetic flux response to bias arm to a stop position." U.S. Patent 5541792, July 1996.

[6] H. K. Khalil, *Nonlinear Systems*. New Jersey: Prentice Hall, 3rd ed., 2002.

[7] M. Krstić, I. Kanellakopoulos, and P. Kokotović, *Nonlinear and Adaptive Control Design*. New York: John Wiley and Sons, 1995.

[8] K. Astrom and B. Wittenmark, *Adaptive Control*. Mass.: Addison Wesley, 2nd ed., 1994.

[9] I. Pejcha, "Head loading and unloading assembly for a magnetic disc drive having a rotary actuator." U.S. Patent 3984873, October 1976.

[10] T. G. Jeong and D. B. Bogy, "An experimental study of the parameters that determine slider-disk contacts during dynamic load-unload," *ASME Journal of Tribology*, vol. 114, pp. 507–514, 1992.

[11] Q. H. Zeng and D. B. Bogy, "Effects of certain design parameters on load/unload performance," *IEEE Transactions on Magnetics*, vol. 36, pp. 140–147, 2000.

[12] P. G. Levi and F. E. Talke, "Load/unload investigations on a rotary actuator disk drive," *IEEE Transactions on Magnetics*, vol. 28, pp. 2877–2879, 1992.

[13] R. T. Ratliff, "Extending actuator range through magnetic flux reversal detection." U.S. Patent 6157509, December 2000.

[14] R. T. Ratliff and C. A. Trammell, "Passive actuator for assisting commutational ramp loading." U.S. Patent 6621651 B1, September 2003.

[15] J. Hauser, S. Sastry, and P. Kokotovic, "Nonlinear control via approximate input-output linearization: The ball and beam example," *IEEE Transactions on Automatic Control*, vol. 37, no. 3, pp. 392–398, 1992.

[16] R. Ghanadan and G. L. Blankenship, "Adaptive control of nonlinear systems via approximate linearization," *IEEE Transactions on Automatic Control*, vol. 41, no. 4, pp. 618–625, 1996.

[17] R. Ghanadan and G. L. Blankenship, "On output tracking for nonlinear systems with singular points," Proceedings IEEE American Control Conference, 1994.

[18] C. J. Tomlin and S. S. Sastry, "Switching through singularities," *Systems & Control Letters*, vol. 35, pp. 145–154, 1998.

[19] W. H. Chen and D. J. Ballance, "On a switching control scheme for nonlinear systems with ill-defined relative degree," *Systems & Control Letters*, vol. 47, pp. 159–166, 2002.

[20] R. L. Boylestad, *Introductory Circuit Analysis*. New York: Macmillan, 6th ed., 1990.

[21] P. Campbell, *Permanent Magnet Materials and Their Application*. Cambridge University Press, 1994.

[22] W. H. Hayt and J. A. Buck, *Engineering Electromagnetics*. New York: McGraw-Hill, 6th ed., 2001.

[23] Hitachi Global Storage, *Ultrastar 36LZX Product Specification*, May 2000.

[24] Western Digital Corporation, *WDE18310 Product Specification*, May 2005.

[25] J. A. Wickert, "Vibration of flex circuits in hard disk drives," *ASME Journal of Vibration and Acoustics*, vol. 125, no. 3, pp. 335–342, 2003.

[26] M. W. Spong and M. Vidyasagar, *Robot Dynamics and Control*. New York: John Wiley and Sons, 1989.

[27] P. A. Ioannou and J. Sun, *Robust Adaptive Control*. NJ: Prentice-Hall, 1996.

[28] K. S. Narendra and A. M. Annaswamy, *Stable Adaptive Systems*. New Jersey: Prentice-Hall, 1989.

[29] C. Aboky, G. Sallet, and J. Vivalda, "Observers for Lipschitz non-linear systems," *International Journal of Control*, vol. 75, no. 3, pp. 204–212, 2002.

[30] R. Rajamani and Y. M. Cho, "Existence and design of observers for nonlinear systems: Relation to distance to unobservability," *International Journal of Control*, vol. 69, no. 5, pp. 717–731, 1998.

[31] L. S. Pontriagin, "Optimal control processes," *English trans.: Automation Express*, vol. 1, pp. 15–18,26–30, 1960.

[32] R. Bellman, I. Glicksberg, and O. Gross, "On the 'bang-bang' control problem'," *Quarterly of Applied Mathematics*, vol. 14, pp. 11–18, 1956.

[33] K. S. Ananthanarayanan, "Third-order theory and bang-bang control of voice coil actuators," *IEEE Transactions on Magnetics*, vol. MAG-18, no. 3, pp. 888–892, 1982.

[34] A. Isidori, *Nonlinear Control Systems*. London: Springer-Verlag, 3 ed., 1990.

[35] R. Hermann and A. J. Krener, "Nonlinear controllability and observability," *IEEE Transactions on Automatic Control*, vol. 22, no. 4, pp. 728–740, 1977.

[36] H. Nijmeijer and A. van der Schaft, *Nonlinear Dynamical Control Systems*. Berlin: Springer-Verlag, 1990.

[37] M. Spivak, *A Comprehensive Introduction to Differential Geometry*. Houston: Publish or Perish, 2005.

[38] R. T. Ratliff and P. R. Pagilla, "Design and seek control of a disc drive actuator with nonlinear magnetic bias," pp. 3640–3646, Proceedings of IEEE International Conference on Robotics and Automation, April 2004.

[39] R. T. Ratliff and P. R. Pagilla, "Commutational ramp load control using a conventional disc drive actuator," Proceedings of International Federation on Automatic Control World Congress, July 2005.

[40] R. T. Ratliff and P. R. Pagilla, "Experimental investigation of disc drive seek control when subject to a nonlinear magnetic bias," Proceedings of IEEE American Control Conference, June 2005.

[41] R. T. Ratliff and P. R. Pagilla, "Output feedback seek control for disc drives with Lipschitz nonlinearities," Proceedings of IEEE Conference on Control Applications, August 2005.

[42] P. R. Pagilla and Y. Zhu, "Controller and observer design for Lipschitz nonlinear systems," Proceedings IEEE American Control Conference, July 2004.

[43] M. Arcak and P. Kokotovic, "Observer-based control of systems with slope-restricted nonlinearities," *IEEE Transactions on Automatic Control*, vol. 46, no. 7, pp. 1146–1150, 2002.

[44] T. Kouhei, T. Yamada, Y. Keroba, and K. Aruga, "A study of head-disk interface shock resistance," *IEEE Transactions on Magnetics*, vol. 31, no. 6, pp. 3006–3008, 1995.

[45] C. C. Lin, "Finite element analysis of a computer hard disk drive under shock," *ASME Journal of Mechanical Design*, vol. 124, pp. 121–125, 2002.

[46] G. Leitmann, "On the efficacy of nonlinear control in uncertain linear systems," *ASME Journal of Dynamic Systems, Measurement, and Control*, vol. 102, no. 1, pp. 95–102, 1981.

[47] R. Byers, "A bisection method for measuring the distance of a stable matrix to the unstable matrices," *SIAM Journal of Scientific and Statistical Computing*, vol. 9, pp. 875–881, 1988.

[48] Y. Yamashita and A. Isidori, "Global output regulation through singularities," Proceedings Conference on Decision and Control, 2000.

VITA

Ryan Ratliff

Candidate for the Degree of

Doctor of Philosophy

Thesis: DISK DRIVE ACTUATOR DESIGN AND CONTROL FOR ROBUST NON-OPERATIONAL SHOCK PERFORMANCE

Major Field: Mechanical Engineering

Biographical:

Personal Data: Born in Toledo, Ohio, USA on February 9, 1970.

Education:

Received the B.S. degree from University of Oklahoma, Norman, Oklahoma, USA, 1992, in Mechanical Engineering

Received the M.S. degree from University of Oklahoma, Norman, Oklahoma, USA, 1997, in Mechanical Engineering

Completed the requirements for the degree of Doctor of Philosophy with a major in Mechanical Engineering and a minor in Control Systems at Oklahoma State University in December, 2005.

Experience:

Engineer/Scientist, The Boeing Company, St. Louis, MO, USA, 2004 to present

Staff Engineer, Seagate Technology, Oklahoma City, OK, June 1994 to January 2004;

Name: Ryan Ratliff Date of Degree: December, 2005

Institution: Oklahoma State University Location: Stillwater, Oklahoma

Title of Study: DISK DRIVE ACTUATOR DESIGN AND CONTROL FOR ROBUST NON-OPERATIONAL SHOCK PERFORMANCE

Pages in Study: 157 Candidate for the Degree of Doctor of Philosophy

Major Field: Mechanical Engineering

As disk drives become more of a commodity based product, quality and cost control have become top industry priorities. Disk drive manufacturers are now heavily focused on efforts to reduce costs while maintaining quality and improving performance. Shock damage of the head/disk interface is one area that causes many quality issues and cost constraints. The most damaging shocks, which can be both linear and rotational in nature, occur during the non-operational state. Several methods are used to combat shocks, many of which preserve servo control performance at the expense of cost increases and reliability issues. The research investigates the combination of improved mechanical designs and advanced control methods to improve servo controller performance while maintaining shock resistance, improving product quality, and providing cost reduction.

A voice coil motor actuator is designed to meet specific seek performance requirements. A low cost, magnetic bias feature on the actuator arm is independently designed to compensate for non-operational rotary shock. Because the resulting bias is nonlinear and uncertain, a model-based adaptive controller was developed to meet the seek performance requirements and simultaneously handle effects of the nonlinear bias. Extensive experiments were conducted to characterize the actuator physical parameters and verify the controller performance. A representative sample of the results is presented and discussed.

To address linear shock resistance, the research investigates the feasibility of a ramp load/unload (L/UL) controller using a conventional, non-L/UL disk drive actuator. Therefore, disk drives with lower cost, higher torque actuators can realize the linear shock resistance benefits of ramp loading. A unique disk drive actuator is designed and optimized for L/UL operation. While on the ramp, there exists a set in the state space where the actuator dynamics are uncontrollable. A sufficient condition is determined that guarantees actuator passage through the uncontrollable region. A state trajectory is generated that, when tracked, moves the actuator through the uncontrollable set for a successful load onto the disk at the desired load velocity. Exponentially stable state-feedback and output feedback controllers are designed for tracking. Experiments are performed to validate and verify the new design.

ADVISOR'S APPROVAL: _____